

Spring 2007

# A comparative study of the extended Kalman filter and sliding mode observer for orbital determination for formation flying about the L(2) Lagrange point

Oliver Olson

*University of New Hampshire, Durham*

Follow this and additional works at: <https://scholars.unh.edu/thesis>

---

## Recommended Citation

Olson, Oliver, "A comparative study of the extended Kalman filter and sliding mode observer for orbital determination for formation flying about the L(2) Lagrange point" (2007). *Master's Theses and Capstones*. 275.  
<https://scholars.unh.edu/thesis/275>

This Thesis is brought to you for free and open access by the Student Scholarship at University of New Hampshire Scholars' Repository. It has been accepted for inclusion in Master's Theses and Capstones by an authorized administrator of University of New Hampshire Scholars' Repository. For more information, please contact [nicole.hentz@unh.edu](mailto:nicole.hentz@unh.edu).

A COMPARATIVE STUDY OF THE EXTENDED KALMAN  
FILTER AND SLIDING MODE OBSERVER FOR ORBITAL  
DETERMINATION FOR FORMATION FLYING ABOUT THE  $L_2$   
LAGRANGE POINT

BY

OLIVER OLSON

B.S., University of New Hampshire, 2004

THESIS

Submitted to the University of New Hampshire  
in partial fulfillment of  
the requirements for the degree of

Master of Science  
in  
Mechanical Engineering

May 2007

UMI Number: 1443625

### INFORMATION TO USERS

The quality of this reproduction is dependent upon the quality of the copy submitted. Broken or indistinct print, colored or poor quality illustrations and photographs, print bleed-through, substandard margins, and improper alignment can adversely affect reproduction.

In the unlikely event that the author did not send a complete manuscript and there are missing pages, these will be noted. Also, if unauthorized copyright material had to be removed, a note will indicate the deletion.

**UMI**<sup>®</sup>

---

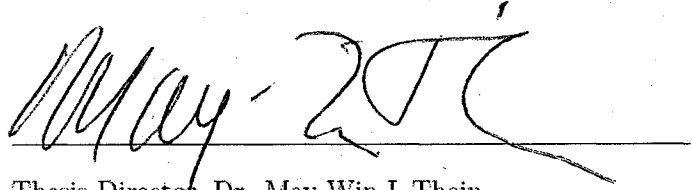
UMI Microform 1443625

Copyright 2007 by ProQuest Information and Learning Company.

All rights reserved. This microform edition is protected against unauthorized copying under Title 17, United States Code.

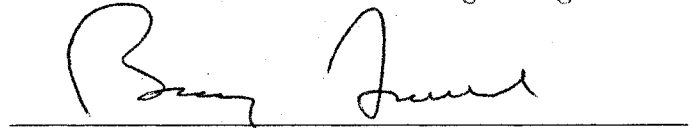
ProQuest Information and Learning Company  
300 North Zeeb Road  
P.O. Box 1346  
Ann Arbor, MI 48106-1346

This thesis has been examined and approved.



Thesis Director, Dr. May-Win L. Thein

Associate Professor of Mechanical Engineering



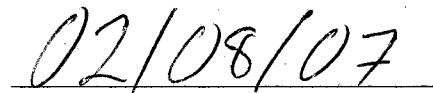
Dr. Barry Fussell

Professor of Mechanical Engineering



Dr. L. Gordon Kraft, III

Professor of Electrical and Computer Engineering



Date

## ACKNOWLEDGEMENTS

I would like to thank everyone who has helped me throughout this work. I am thankful to my thesis supervisor, Professor May-Win Thein, for her guidance, help and encouragement. To Professors Barry Fussell and Gordon Kraft, for teaching me about controls and spending their time evaluating my thesis. To the New Hampshire Space Grant Consortium for funding this research. To Tracey Harvey, for her dedicated service to the students, faculty, and staff. To my family for their constant love and support since the day I was born. To all my friends for their encouragement along the way. To Rob Schuman. Thanks for all the help. To Jennie Mac. Thanks for all the love.

And to my mother, Anne Olson. She did a great job.

## TABLE OF CONTENTS

ACKNOWLEDGEMENTS . . . . .	iii
LIST OF FIGURES . . . . .	ix
ABSTRACT . . . . .	x
<b>1 INTRODUCTION</b>	<b>1</b>
1.1 Distributed Spacecraft Systems and Formation Flying . . . . .	1
1.2 Orbit Determination . . . . .	3
1.2.1 General Orbit Determination . . . . .	3
1.2.2 Orbit Determination About $L_2$ . . . . .	4
1.2.3 Orbit Determination for Formation Flying About $L_2$ . . . . .	5
1.2.4 The Extended Kalman Filter . . . . .	6
1.2.5 The Sliding Mode Observer . . . . .	7
1.3 Thesis Outline . . . . .	8
<b>2 FORMATION FLYING ABOUT <math>L_2</math> LIBRATION POINTS</b>	<b>11</b>
2.1 The Restricted Three Body Problem . . . . .	11
2.2 Libration Points . . . . .	15
2.3 Formation Flying in Orbit About an $L_2$ Point . . . . .	18
2.4 Space Environment at the $L_2$ Point . . . . .	19
<b>3 THE EXTENDED KALMAN FILTER</b>	<b>23</b>
3.1 The Continuous-Time Extended Kalman Filter . . . . .	23
<b>4 SLIDING MODE OBSERVERS</b>	<b>30</b>
4.1 Sliding Mode Observers . . . . .	30

<b>5</b>	<b>SIMULATION CHARACTERISTICS</b>	<b>36</b>
5.1	Formation Flying Scenario . . . . .	36
5.2	VISNAV Measurement System . . . . .	38
5.2.1	Measurement Model . . . . .	40
5.2.2	Simulation Conditions . . . . .	41
5.3	Control Law . . . . .	43
<b>6</b>	<b>EXTENDED KALMAN FILTER FOR FORMATION FLYING</b>	<b>45</b>
6.1	Extended Kalman Filter Simulations . . . . .	45
6.2	Extended Kalman Filter Covariance Matrix Selection . . . . .	49
6.3	Extended Kalman Filter Covariance Matrix Tuning . . . . .	50
6.4	Extended Kalman Filter Results . . . . .	51
6.4.1	Case One: Inaccurate Initial Conditions . . . . .	52
6.4.2	Case Two: Input Disturbances . . . . .	54
6.4.3	Case Three: Parameter Uncertainty . . . . .	55
6.4.4	Case Four: Measurement Noise . . . . .	57
6.4.5	Case Five: Cumulative Inaccuracies and Disturbances . . . . .	58
<b>7</b>	<b>SLIDING MODE OBSERVER FOR FORMATION FLYING</b>	<b>65</b>
7.1	Sliding Mode Observer Simulations . . . . .	65
7.2	Sliding Mode Observer Gain Selection . . . . .	65
7.3	Sliding Mode Observer Gain Tuning . . . . .	67
7.4	Sliding Mode Observer Results . . . . .	71
7.4.1	Case One: Inaccurate Initial Conditions . . . . .	72
7.4.2	Case Two: Input Disturbances . . . . .	72
7.4.3	Case Three: Parameter Uncertainty . . . . .	73
7.4.4	Case Four: Measurement Noise . . . . .	75

7.4.5	Case Five: Cumulative Inaccuracies and Disturbances . . . . .	76
<b>8</b>	<b>COMPARISON OF EKF AND SMO</b>	<b>83</b>
8.1	Case Results . . . . .	83
8.2	Sensitivity Comparisons . . . . .	92
8.3	Considerations . . . . .	96
<b>9</b>	<b>RESEARCH SUMMARY AND FUTURE WORK</b>	<b>99</b>
9.1	Conclusions . . . . .	99
9.2	Future Work . . . . .	101
	<b>BIBLIOGRAPHY</b>	<b>103</b>
	<b>APPENDICES</b>	<b>107</b>
	<b>APPENDIX A CONSTITUTION X MODELS</b>	<b>108</b>
A.1	Simulation Models . . . . .	108
	<b>APPENDIX B EKF - DIAGRAMS &amp; MATLAB FILES</b>	<b>111</b>
B.1	Extended Kalman Filter . . . . .	111
	<b>APPENDIX C SMO - DIAGRAMS &amp; MATLAB FILES</b>	<b>118</b>
C.1	Sliding Mode Observer . . . . .	118



## LIST OF FIGURES

2-1	Restricted Three Body Problem Geometry [1] . . . . .	13
2-2	Libration Point Locations [1] . . . . .	17
2-3	Two Spacecraft Orbiting in the Earth/Moon - Sun Rotating Frame [2]	20
4-1	Reaching And Sliding Phenomena of Sample State Trajectories on the Phase Plane [3] . . . . .	31
5-1	VISNAV Measurement System . . . . .	40
6-1	Case One - EKF Relative Position Error Magnitude . . . . .	53
6-2	Case Two - EKF Relative Position Error Magnitude . . . . .	55
6-3	Case Three - EKF Relative Position Error Magnitude . . . . .	56
6-4	Case Four - EKF Relative Position Error Magnitude . . . . .	57
6-5	Case Five - EKF Relative Position Estimates . . . . .	58
6-6	Case Five - EKF Relative Position Estimates (Magnified) . . . . .	59
6-7	Case Five - EKF Relative Position Estimate Error Magnitude . . . . .	60
6-8	Case Five - EKF Relative Position Estimate Error Magnitude (Magnified)	60
6-9	Case Five - EKF Relative Velocity Estimates . . . . .	61
6-10	Case Five - EKF Relative Velocity Estimates (Magnified) . . . . .	62
6-11	Case Five - EKF Relative Velocity Estimate Error Magnitude . . . . .	63
6-12	Case Five - EKF Velocity Estimate Error Magnitude (Magnified) . . . . .	63
6-13	Case Five - EKF Relative Position Error Magnitude . . . . .	64
6-14	Case Five - EKF Relative Position Error Magnitude (Magnified) . . . . .	64
7-1	Case One - SMO Relative Position Error Magnitude . . . . .	72

7-2	Case Two - SMO Relative Position Error Magnitude . . . . .	73
7-3	Case Three - SMO Relative Position Error Magnitude . . . . .	74
7-4	Case Four - SMO Relative Position Error Magnitude . . . . .	75
7-5	Case Five - SMO Relative Position Estimates . . . . .	76
7-6	Case Five - SMO Relative Position Estimates (Magnified) . . . . .	77
7-7	Case Five - SMO Relative Position Estimate Error Magnitude . . . . .	78
7-8	Case Five - SMO Relative Position Estimate Error Magnitude (Magnified) . . . . .	78
7-9	Case Five - SMO Relative Velocity Estimates . . . . .	79
7-10	Case Five - SMO Relative Velocity Estimates (Magnified) . . . . .	80
7-11	Case Five - SMO Relative Velocity Estimate Error Magnitude . . . . .	80
7-12	Case Five - SMO Relative Velocity Estimate Error Magnitude (Magnified) . . . . .	81
7-13	Case Five - SMO Relative Position Error Magnitude . . . . .	82
7-14	Case Five - SMO Relative Position Error Magnitude (Magnified) . . . . .	82
8-1	Case One - Steady-State Statistics of $ \mathbf{x}_e $ . . . . .	84
8-2	Case One - Time Values of $ \mathbf{x}_e $ . . . . .	85
8-3	Case Two - Time Values of $ \mathbf{x}_e $ . . . . .	85
8-4	Case Three - Steady-State Statistics of $ \mathbf{x}_e $ . . . . .	86
8-5	Case Three - Time Values of $ \mathbf{x}_e $ . . . . .	86
8-6	Case Four - Steady-State Statistics of $ \mathbf{x}_e $ . . . . .	87
8-7	Case Four - Time Values of $ \mathbf{x}_e $ . . . . .	87
8-8	Case Five - Steady-State Statistics of $ \tilde{\mathbf{x}} $ . . . . .	89
8-9	Case Five - Steady-State Statistics of $ \dot{\tilde{\mathbf{x}}} $ . . . . .	89
8-10	Case Five - Steady-State Statistics of $ \mathbf{x}_e $ . . . . .	90
8-11	Case Five - Time Values of $ \mathbf{x}_e $ . . . . .	90

8-12	Overshoot Values of $ \mathbf{x}_e $ . . . . .	91
8-13	Observer Sensitivity to Parameter Uncertainty - $\tau_{SE}$ . . . . .	92
8-14	Observer Sensitivity to Parameter Uncertainty - $\tau_{EL}$ . . . . .	93
8-15	Observer Sensitivity to Measurement Noise . . . . .	94
8-16	Observer Sensitivity to Disturbance Accelerations . . . . .	95
A-1	Main Block Diagram - Constellation X Model . . . . .	109
A-2	Measurement Model Sub-block . . . . .	110
B-1	Main Block Diagram - Extended Kalman Filter . . . . .	112
B-2	Estimated Beacon Unit Vector Sub-block . . . . .	113
B-3	Sub-block A . . . . .	113
B-4	$f(\mathbf{x},t)$ Sub-block . . . . .	114
B-5	Kalman Gain Sub-block . . . . .	115
B-6	Measurement Jacobian Sub-block . . . . .	116
B-7	System Jacobian Sub-block . . . . .	117
C-1	Main Block Diagram - Sliding Mode Observer . . . . .	119

## ABSTRACT

### A COMPARATIVE STUDY OF THE EXTENDED KALMAN FILTER AND SLIDING MODE OBSERVER FOR ORBITAL DETERMINATION FOR FORMATION FLYING ABOUT THE $L_2$ LAGRANGE POINT

by

Oliver Olson

University of New Hampshire, May, 2007

Two nonlinear state estimation techniques, the Sliding Mode Observer and the Extended Kalman Filter, are compared in terms of their ability to provide accurate relative position and velocity estimates for a formation flying mission about the Earth/Moon - Sun  $L_2$  libration point. The observers are individually tested on the NASA Constellation X simulation model. Constellation X is a proposed x-ray telescope mission, where formation flying spacecraft was considered as a possible mission scenario. A follower spacecraft is controlled to maintain a fixed distance (50 meters) from a leader spacecraft to within 1 millimeter accuracy.

The state estimates propagated by each observer were of sufficient accuracy to maintain the required separation distance to within mission design requirements. For these particular formations of the Extended Kalman Filter and the Sliding Mode Observer, the Extended Kalman Filter is shown to be less sensitive to measurement noise levels, and the Sliding Mode Observer is shown to be less sensitive to input disturbances. There is no overall significant difference in sensitivity to parametric uncertainties between observers.

# CHAPTER 1

## INTRODUCTION

### 1.1 Distributed Spacecraft Systems and Formation Flying

A Distributed Spacecraft System (DSS) consists of two or more spacecraft operating together to accomplish a shared objective. Formation flying is a subset of the DSS architecture. Formation flying missions impose the requirement that the spacecraft maintain a designated attitude and/or relative position with respect to one another, or a common point of interest [2]. Meeting such requirements demands precise measurement and control capabilities. Although such capabilities are costly, the use of individual satellites in a formation is an attractive alternative to rigidly connecting spacecraft for several reasons. Many satellite formations which would be small enough to be rigidly connected would still be too large to be connected during launch. This would require assembly in space, increasing complexities for a successful mission. In the event of vibration between formation members, the absence of atmospheric damping beyond low earth orbit would impose the requirement for damping control, or the necessity to wait for damping to die out due to internal heat losses in the connecting members. Finally, DSS missions may require separation distances of a kilometer or more, making rigidly connecting the formation members a practical impossibility.

Deep space imaging is one particular venue that is driving the need for formation flying systems. For stand-alone telescopes, an increase in resolution demands an increase in size. Obeying this constraint quickly leads to the requirement for

telescopes which are simply too large to build practically. To overcome this hurdle, astronomers make use of a technique called interferometry, the process of coupling two or more telescopes together to synthetically build an aperture equal to the separation of the telescopes. The potential usefulness of formation flying systems for deep space imaging is made evident in the context of interferometry. Multiple spacecraft can each serve as constituent elements for the formation of a large telescope, allowing for greater resolution than can be achieved by stand-alone telescopes.

As an example of formation flying applications, several NASA formation flying missions are currently under development:

- The Stellar Imager (SI) [4] is a mission to investigate solar and stellar magnetic activity and its impact on the origin and continued existence of life in the universe. To accomplish this goal it will require a resolution of 100 microarcseconds, 100 times greater than that of the Hubble telescope. To that end it will require a multi-spacecraft interferometer composed of more than 20 members in a stable environment, such as in a Lissajous<sup>1</sup> orbit about the Earth/Moon-Sun L2 libration point.
- The Terrestrial Planet Finder (TPF) [5] is a formerly proposed NASA mission. It was to be NASA's first space-based mission to directly observe planets in other solar systems. The TPF was to make use of five member spacecraft flying in formation about one kilometer apart. Four of the satellites were to have telescopes, while the fifth was to act as a combiner.
- The Microarcsecond X-ray Imaging Mission (MAXIM) [6] has the potential for achieving 100 nanoarcsecond resolution, which would allow it to provide the first ever x-ray images of Sagittarius A, the suspected supermassive black hole

---

<sup>1</sup>Lissajous orbits are the natural periodic motion of a satellite about any two-body system's collinear libration points:  $L_1$ ,  $L_2$ , and  $L_3$ . They are composed of a combination of planar and vertical components.

at the center of the Milky Way galaxy. For an X-ray interferometer large enough to achieve such resolution, MAXIM would require 33 spacecraft equipped with telescopes, and a combiner spacecraft located 500 kilometers behind the mirrors. The proposed MAXIM mission could launch in the latter part of the next decade.

## 1.2 Orbit Determination

This research investigates the performance of two state estimation techniques, implemented in a formation flying mission about the Earth/Moon-Sun  $L_2$  libration point. As will be discussed, the  $L_2$  point is too far from Earth ( $\simeq 1,500,000$  km) for spacecraft to obtain GPS relative position updates of adequate accuracy. On-board hardware is required to obtain adequate relative position estimates. As a basis for comparison, relative position and velocity estimation errors are discussed.

Relative position measurements are obtained with the aid of the Visual Navigation (VISNAV) system developed by Kim et al [7]. VISNAV is an on-board measurement system comprised of an electro-optical sensor placed on one spacecraft to detect the light emitted by beacons on another spacecraft in the formation. The unit vectors between the beacons and the sensor are measured, then processed to produce relative position and attitude estimates. For this research, satellite attitude (orientation in space) measurements are not considered. The VISNAV measurement system shows promise in applications such as spacecraft rendezvous and docking, autonomous aerial refuelling of UAVs, and lost-in-space attitude and position determination [8, 9, 10].

### 1.2.1 General Orbit Determination

The act of determining the relative position and velocity between spacecraft in a formation flying pattern is the act of specifying each spacecraft's orbit. An orbit is

the curved path (some conic section) traversed by a satellite about a celestial body. Assume there exists a celestial body and its satellite, both of known mass. A satellite's orbit is defined when its relative position and velocity are known with respect to its celestial body at some point in time [1]. Although this is a straightforward mathematical concept, it does not provide an intuitive visualization of a satellite's orbit. For this reason, other quantities are used to specify a satellite's orbit. Although there are different techniques using differing parameters to describe an orbit, these parameters must be used to reveal the shape of the orbit, the satellite's position in the orbit at a given time, and the orientation of the orbit in space (i.e. the orientation of the orbital plane with respect to the equatorial plane of the celestial body).

Information regarding the satellite's position in the orbit was originally updated to the satellite from ground stations on Earth. With the advent of GPS, however, improved methods of updating a satellite's position have evolved [11]. Satellites with GPS receivers are able to receive accurate position estimates from GPS satellites. This is advantageous over ground station updates because it eliminates the periodic unavailability of position updates when the satellite is not within view of the ground station. With missions requiring accurate attitude knowledge, the method of using onboard GPS updates can be improved with systems such as the GPS-MAGNAV system developed at NASA's Goddard Space Flight Center [12]. In addition to onboard GPS updates, the GPS-MAGNAV system uses low-cost, low weight magnetometers to determine attitude for satellites in Low-Earth Orbiting (LEO) satellites.

### 1.2.2 Orbit Determination About $L_2$

More specific than orbit determination in general, is orbit determination for satellites about the Earth/Moon-Sun  $L_2$  Libration point (libration points and associated dynamics are discussed later in this work). This point is approximately 1,500,000 kilo-



meters from Earth, on the side not facing the Sun. At this point a satellite's inertial acceleration is balanced by the gravitational acceleration from the Earth (and Moon) and the Sun. The Genesis spacecraft mission, charged with collecting solar wind samples, entailed the first ever unmanned sample return from a libration point orbit to an Earth touchdown [13]. The Genesis spacecraft orbited the Earth/Moon-Sun  $L_1$  point for 2 years while collecting samples, and flew by the  $L_2$  point on its return to Earth. Another example of a satellite mission involving orbit around the Earth/Moon - Sun  $L_2$  point is Gaia [14]. Beginning in 2011, this mission involves the Gaia spacecraft orbiting  $L_2$  for ten years. Gaia's mission is to collect compositional information, as well as positional and radial velocity measurements of approximately one billion stars in the Milky Way Galaxy and throughout the Local Group (the group of 30 closely packed galaxies including the Milky Way). The data collected by Gaia will provide information for a complex three-dimensional map of our Galaxy (although one billion stars is less than one percent of the total number of stars in our galaxy). Yet another satellite mission involving orbit about the Earth/Moon Sun  $L_2$  point is the James Webb Space Telescope [15, 16]. This mission, scheduled for launch in 2013, involves a large, infrared telescope whose mission is fourfold: to search for light from the first stars and galaxies, study galactic evolution, study the formation of stars and planetary systems, and to investigate planetary systems and the origins of life.

### 1.2.3 Orbit Determination for Formation Flying About $L_2$

Other specific examples requiring orbit determination, are formation flying missions, whether they be formation flying missions about the Earth/Moon-Sun  $L_2$  point, or some other location. An example of the latter is the Gravity Recovery and Climate Experiment (GRACE) project [17]. Launched in March of 2002, this formation flying mission involves flying two satellites 100-500 km apart, in orbit about the Earth, to

produce a new model of the Earth's gravitational field every 30 days. The differing gravitational forces experienced by each satellite in the formation reveal the differences in Earth's gravitational field on a position basis. Because a new gravitational model is produced every 30 days by the GRACE satellites, the time-varying nature of Earth's gravitational field will also be investigated.

Most specifically, examples of formation flying missions about the Earth/Moon-Sun  $L_2$  libration point follow. The previously mentioned Stellar Imager (SI), Terrestrial Planet Finder (TPF) and Microarcsecond X-ray Imaging Mission (MAXIM), were all proposed to orbit about  $L_2$  [18, 19, 20]. The European Space Agency's Darwin Mission [21] consists of four spacecraft, each containing an infrared telescope. Scheduled for launch sometime after 2014, the mission is charged with detecting Earth-like planets, and searching for the possibility of life on these planets by searching for atmospheric gases that may indicate life.

The preceding missions represent a sampling of future applications of formation flying. There are multiple architectures for formation flying missions, with the appropriate architecture decided upon for each mission on an individual basis. Scharf et al. summarize these architectures in [22].

#### 1.2.4 The Extended Kalman Filter

The Extended Kalman Filter (EKF) is the natural extension to the Kalman Filter for nonlinear estimation problems. It is often used as a nonlinear state estimator because of its ability to minimize the mean square estimation error. The EKF has a lack of guaranteed stability, so filter design is often verified through Monte-Carlo simulations. Despite its lack of guaranteed stability, the EKF has been successfully implemented in a wide variety of applications, and is considered standard for formation flying applications. Kim et al. developed an approach for relative navigation

and attitude estimation using the VISNAV system [7]. Accurate relative position and attitude estimates are obtained by processing line-of-site measurements coupled with gyroscopic measurements and dynamic models in an EKF. Busse, How, and Simpson used the EKF along with a carrier-phase differential GPS (CDGPS) measurement model for Low-Earth Orbit (LEO) formation estimation [23]. The EKF's dependence on a near-perfect system model is reduced by augmenting the filter with adaptive filtering techniques based on the method of maximum likelihood estimation (MMLE). Hardware-in-the-loop simulations at NASA Goddard Space Flight Center demonstrate less than 2 cm relative position error and less than 0.3 mm/s relative velocity error for formation separations of 1-2 km. Philip also shows the EKF to provide adequate results when used to filter noisy relative position and velocity measurements for spacecraft rendezvous [24].

### 1.2.5 The Sliding Mode Observer

Sliding Mode Observers (SMO) are nonlinear state estimators whose development stems from the theory of variable structure systems [25]. They were developed to address the dependence of the classical observers, such as the Kalman Filter and Luenberger Observer, on precise mathematical representations of the plant. As a result, some advantages of the SMO include robustness to bounded system parameter uncertainties and input disturbances. Examples of SMO for state estimation in formation flying are rare, though Thein et al. have investigated their use in a formation flying mission about the Earth/Moon-Sun  $L_2$  point [26]. Limited examples of comparisons between the EKF and SMO have been found for applications not pertaining to formation flying. For example, Park et al. [27] compared these two state estimators in a cold flow circulating fluidized bed, a system applied to a wide variety of chemical industry processes. This system's purpose is to reduce pollution and raise efficiency. The de-

cision to investigate the performance of an SMO is prompted by the EKF's inability to provide adequate state and standpipe height estimates for certain oscillating input cases. In this case, the Sliding Mode Observer is found to compare favorably to the Extended Kalman Filter. Chen and Dunnigan compare the performance of the EKF and SMO for full state estimation (stator currents and rotor fluxes) in an induction machine [28]. For this application, the SMO and EKF perform comparably, but the Sliding Mode Observer is favored due to its ease of implementation, lower computational burden, and lack of demand for accurate noise statistics. It should be noted that the SMO used by Chen and Dunnigan is formulated differently than the SMO used in this work, as proposed by Misawa [29, 30]. As will be explained subsequently, this work utilizes a constant gain matrix  $K$  multiplied by a suitable switching function (e.g. the signum or saturation function) to ensure that error trajectories remain on the sliding surface. As a means of dealing with the chattering associated with the sliding mode method, this work employs a boundary layer to minimize chatter. The SMO implemented in [28] accomplishes these tasks by using a variable observer gain  $K$ , modified as a function of the sliding surface.

The goal of this thesis is to provide a more extensive effort into comparing the Extended Kalman Filter and Sliding Mode Observer proposed by Misawa for state estimation in the context of formation flying about the  $L_2$  Lagrange point. The contributions of this research include developing a simulation model for each observer and individually implementing each observer into the pre-existing NASA Constellation X simulation model in MATLAB/Simulink. Simulations are run assuming various conditions, and the observers are compared in terms of their ability to provide accurate relative position and velocity estimates.

### 1.3 Thesis Outline

This thesis is organized as follows:

- Chapter 2, Formation Flying About  $L_2$  Libration Points - An explanation of the Restricted Three Body Problem and Libration Points are given. Based on this explanation, Formation Flying in orbit about an  $L_2$  point is discussed.
- Chapter 3, The Extended Kalman Filter - The continuous-time Extended Kalman Filter is derived by extending the Kalman Filter to nonlinear systems.
- Chapter 4, Sliding Mode Observers - The Sliding Mode Observer is described by first describing Sliding Mode Control and extending these concept to estimation.
- Chapter 5, Constellation X - The NASA Constellation X simulation model is introduced as the platform on which the observers will be compared. The measurement model and control laws are subsequently explained.
- Chapter 6, The Extended Kalman Filter For Formation Flying - The Extended Kalman Filter is implemented on an example  $L_2$  formation flying mission. It is defined by describing the state and measurement Jacobi and the selection and tuning of the covariance matrices. Relative position and velocity estimates and errors are discussed.
- Chapter 7, The Sliding Mode Observer For Formation Flying - The Sliding Mode Observer is implemented on the same  $L_2$  formation flying mission as the EKF. It is defined by describing the selection of the sliding surface, boundary layer thickness, and Luenberger and Switching Gain selection and tuning. As with the Extended Kalman Filter, relative position and velocity estimates and errors are discussed.

- Chapter 8, Comparison Of Extended Kalman Filter And Sliding Mode Observer  
- The results of the simulations from Chapters 6 and 7 are discussed.
- Chapter 9, Research Summary and Future Work - Contributions of this research are summarized and conclusions are drawn. Possible topics of future research are suggested.

## CHAPTER 2

# FORMATION FLYING ABOUT $L_2$ LIBRATION POINTS

### 2.1 The Restricted Three Body Problem

The Restricted Three Body Problem (RTBP) investigates the motion of an infinitesimal mass influenced by the gravitational fields of two finite masses in circular orbit about their common center of mass. This problem was originally formulated by Euler in 1772 to study the motion of the Moon about the Earth, perturbed by the Sun [1]. In our own solar system there are many opportunities to use the RTBP. One may formulate the RTBP using the Sun and Jupiter as the primary bodies to study the motion of asteroids and comets, or one may use the Earth and Moon as primary bodies to study the motion of spacecraft within the Earth/Moon system. The RTBP may also be used to find likely planetary orbits about double-star systems, once the motion of the two stars is known.

The Restricted Three Body Problem may be solved using numerical techniques, as there is no solution in the form of an analytic, differentiable function of both the initial conditions and time. Henri Poincaré first proved that an analytical solution to the closed form solution does not exist. As the RTBP has been studied over the last 200 years, certain conventions have been established pertaining to units for mass, length and time, as well as coordinate frames.

The simplest unit convention is to use the distance between the two primary bodies as the unit of length:

$$a_{12} = 1 \quad (2.1)$$

As a unit of mass, the masses of all bodies in the problem sum to unity. Since the mass of the third body is infinitesimal, only the two primary bodies are of importance.

$$\begin{aligned} m_1 + m_2 &= 1 \\ m_1 &= 1 - \mu \\ m_2 &= \mu \end{aligned} \quad (2.2)$$

The smaller mass is traditionally referred to as  $m_2$ . Note that the quantity  $\mu$  referred to here is different than the gravitational parameter  $\mu_{(\cdot)}$  referred to elsewhere. The quantity  $\mu$  is the mass ratio of the restricted problem, or the ratio of the smaller mass to that of the larger mass. The quantity  $\mu_{(\cdot)}$  is referred to as the standard gravitational parameter, the product of a celestial body's mass  $M$  and the universal gravitational constant  $G$ .

Kepler's Third Law is used to define the time unit. Kepler's Third law states that the square of the period of time it takes a planet to complete an orbit of the Sun is proportional to the cube of its mean distance from the Sun. This law was originally formulated in 1619 as

$$p^2 = ka^3 \quad (2.3)$$

where  $p$  represents the orbit period and  $a$  represents the semi-major axis length. The constant  $k$  was found by Kepler to be unique for every body under consideration, although he did not have an understanding of its physical meaning. Newton later stated that  $k$  was a description of gravitational force and rewrote Kepler's Third Law as

$$T^2 = \left[ \frac{4\pi^2}{G(m_1 + m_2)} \right] a^3 \quad (2.4)$$



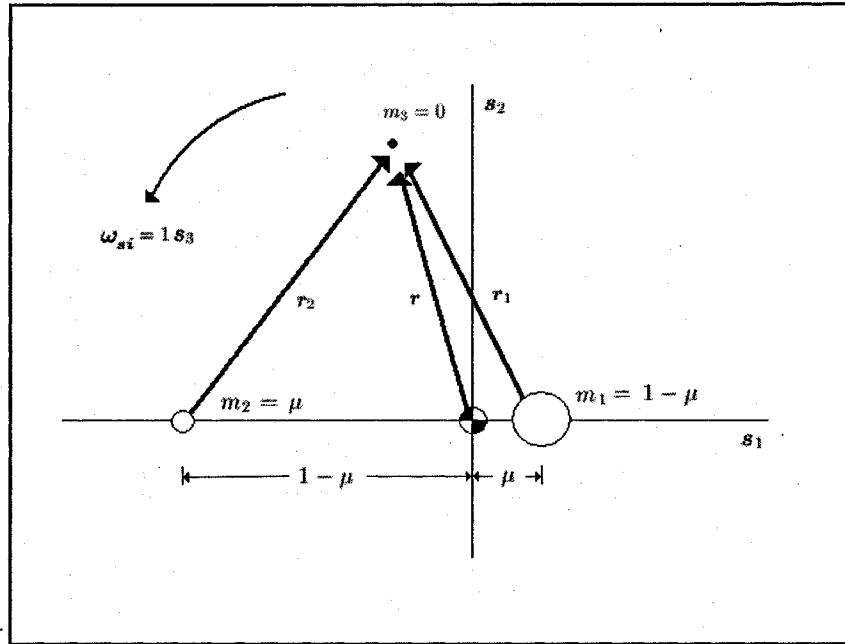


Figure 2-1: Restricted Three Body Problem Geometry [1]

where  $T$  takes on the same meaning as  $P$ ,  $G$  represents the universal gravitational constant,  $m_1$  represents the mass of the primary body, and  $m_2$  represents the mass of the body orbiting the primary body. For the purposes of ascribing the time unit to the Restricted Three Body Problem,  $G$  is assumed to be 1, making the period of the two primary bodies in their orbit about one another

$$T_{12} = 2\pi \left[ \frac{a_{12}^3}{G(m_1 + m_2)} \right]^{1/2} = 2\pi \quad (2.5)$$

Here the time unit is set as a result of the choice for  $G$ .

Traditionally, the RTBP is set in a reference frame that rotates with the orbital motion of the primary objects. The primary objects lie on the  $s_1$  axis, and the origin of the reference frame is located at the center of mass of the two primary objects as depicted in figure 2-1. The second axis,  $s_2$ , is orthogonal to  $s_1$  and lies in the orbital plane of the primary masses. The final axis,  $s_3$ , is the axis of rotation, and completes the dextral (right-handed) orthogonal triad. Note from Figure 2-1 that

since the problem is considered using nondimensional units, all physical variables may be measured in terms of  $\mu$ . For instance, the quantity  $\mu$  refers to both the mass of the secondary body  $m_2$ , as well as the distance of the primary body  $m_1$  from the center of the reference frame. Conversely, the quantity  $1 - \mu$  refers to both the mass of the primary body  $m_1$ , and the distance of the secondary body  $m_2$  from the center of the reference frame.

Because the rotational period of this frame is  $2\pi$ , the rotating reference frame has a inertial angular velocity  $\omega_{si} = 1\mathbf{s}_3$ . The inertial acceleration of the third body must be calculated in order to obtain the equations of motion. For convenience, this acceleration may be expressed in terms of the unit vectors of the rotating frame  $\mathbf{s}$

$$\left(\frac{d^2}{dt^2}\mathbf{r}_i\right) = \frac{d^2}{dt^2}\mathbf{r}_s + 2\omega_{si} \times \frac{d}{dt}\mathbf{r}_s + \omega_{si} \times (\omega_{si} \times \mathbf{r}_s) \quad (2.6)$$

where the subscripts  $i$  and  $s$  denote the inertial and rotating frames, respectively.

The position vector of the third body given as

$$\mathbf{r}_s = x\mathbf{s}_1 + y\mathbf{s}_2 + z\mathbf{s}_3 \quad (2.7)$$

and the time derivatives on the right of Eq. (2.6) are given as

$$\begin{aligned} \frac{d}{dt}\mathbf{r}_s &= \dot{x}\mathbf{s}_1 + \dot{y}\mathbf{s}_2 + \dot{z}\mathbf{s}_3 \\ \frac{d^2}{dt^2}\mathbf{r}_s &= \ddot{x}\mathbf{s}_1 + \ddot{y}\mathbf{s}_2 + \ddot{z}\mathbf{s}_3 \end{aligned} \quad (2.8)$$

After carrying out the cross products, Eq. (2.6) is expressed in the inertial frame as

$$\left(\frac{d^2}{dt^2}\mathbf{r}_i\right) = (\ddot{x} - 2\dot{y} - x)\mathbf{s}_1 + (\ddot{y} + 2\dot{x} - y)\mathbf{s}_2 + \ddot{z}\mathbf{s}_3 \quad (2.9)$$

It is now necessary to calculate the gravitational acceleration of the third body. This acceleration is dependent upon the distances of this body from the primary bodies. The distance between the third body and the larger and smaller primary

bodies are given as  $r_1$  and  $r_2$ , respectively.

$$\begin{aligned} r_1 &= [(x - \mu)^2 + y^2 + z^2]^{1/2} \\ r_2 &= [(x + 1 - \mu)^2 + y^2 + z^2]^{1/2} \end{aligned} \quad (2.10)$$

The distances are calculated using the  $x$ ,  $y$ , and  $z$ -components of the position vectors  $\mathbf{r}_1$  and  $\mathbf{r}_2$  based on the fact that the third body is located at  $(x, y, z)$  and the larger and smaller primary bodies are situated at  $(\mu, 0, 0)$  and  $(\mu - 1, 0, 0)$ , respectively. Using the equation for the force of gravity between two objects separated by a distance  $r$

$$\mathbf{F}_g = -\frac{Gm_a m_b}{r^2} \frac{\mathbf{r}}{r} \quad (2.11)$$

the gravitational acceleration of the third mass can now be calculated

$$\mathbf{a}_g = -\frac{(1 - \mu)\mathbf{r}_1}{r_1^3} - \frac{\mu\mathbf{r}_2}{r_2^3} \quad (2.12)$$

where the first and second term represent gravitational accelerations experienced by  $m_3$  from  $m_1$  and  $m_2$ , respectively. The equations of motion can now be formulated by equating the inertial acceleration of the third object with its gravitational acceleration term. The final result becomes

$$\ddot{x} - 2\dot{y} - x = -\frac{(1 - \mu)(x - \mu)}{r_1^3} - \frac{\mu(x + 1 - \mu)}{r_2^3} \quad (2.13)$$

$$\ddot{y} + 2\dot{x} - y = -\frac{(1 - \mu)y}{r_1^3} - \frac{\mu y}{r_2^3} \quad (2.14)$$

$$\ddot{z} = -\frac{(1 - \mu)z}{r_1^3} - \frac{\mu z}{r_2^3} \quad (2.15)$$

## 2.2 Libration Points

As stated previously, there is no closed form solution to this set of nonlinear ordinary differential equations. However, useful information has been extracted from these equations, most notably the location of the libration points, or LaGrangian

points. Libration points are the stationary solutions to the Restricted Three Body Problem (RTBP). When viewed in a rotating reference frame which rotates with the primary bodies (centered about their common center of mass), the infinitesimal mass is stationary with respect to the two primary bodies at each of the libration points. This is because at these points, inertial acceleration of the infinitesimal mass is equal to the net gravitational acceleration it experiences from the primary bodies. There are five stationary solutions to the RTBP, indicating that these three-body systems have five libration points. Further information about libration points can be found in[1].

Libration points are the equilibrium points of the RTBP. They are found when the RTBP is investigated in the rotating frame. To do this, Eqs. (2.13),(2.14), and (2.15) must be investigated with all velocity and acceleration terms set to zero. The reformulation of the equations of motion becomes

$$-x = -\frac{(1-\mu)(x-\mu)}{r_1^3} - \frac{\mu(x+1-\mu)}{r_2^3} \quad (2.16)$$

$$-y = -\frac{(1-\mu)y}{r_1^3} - \frac{\mu y}{r_2^3} \quad (2.17)$$

$$0 = -\frac{(1-\mu)z}{r_1^3} - \frac{\mu z}{r_2^3} \quad (2.18)$$

Eq. (2.18) immediately indicates that  $z = 0$ , meaning all equilibrium points are contained within the orbital plane of the primary masses. This solution agrees with intuition. Since  $z$  is universally zero for all equilibrium points, only Eqs. (2.16) and (2.17) remain; a system of two equations and two unknowns. Two equilibrium points are found using the assumption that  $r_1 = r_2 = 1$ . A review of figure 2-1 under these assumptions reveals that this situation presents two solutions, both having each of the three bodies centered at the vertex of an equilateral triangle. These two solutions are called the triangular points of the RTBP, and were found by the Italian-French

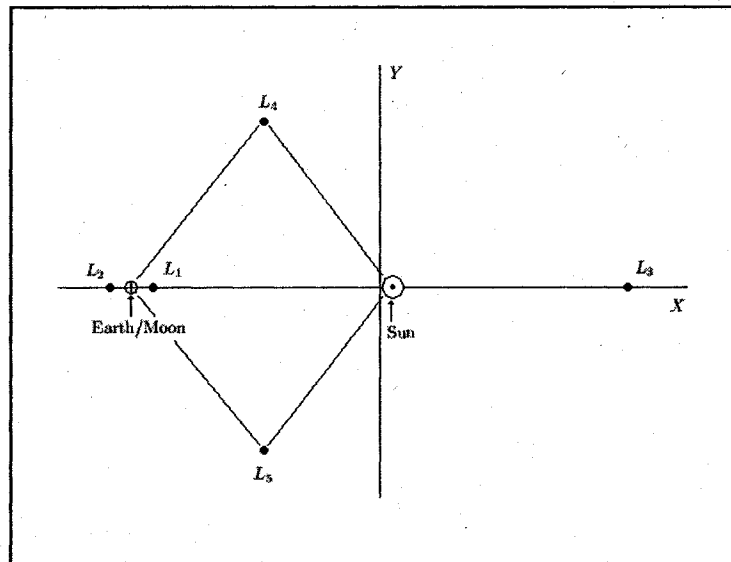


Figure 2-2: Libration Point Locations [1]

Mathematician Joseph Louis LaGrange in 1772, the same year Euler formulated the RTBP. In honor of their discoverer, these points are named  $L_4$  and  $L_5$ . A simple geometric analysis reveals the coordinates of  $L_4$  and  $L_5$  to be  $(-0.5, 0.75, 0)$  and  $(-0.5, -0.75, 0)$ , respectively. The reason  $L_4$  and  $L_5$  are equilibrium points is that at these points, the third body is equidistant from each of the two primary bodies. As a result, the gravitational forces felt by the third body from each of the two primary bodies are in the same ratio as that of the masses of the primary bodies. The resultant force acts through the barycenter (the center of mass and rotation, located at the origin of the inertial frame) of the system. This force is balanced by the inertia of the body in rotation about the barycenter.

There are three other equilibrium points lying on the  $s_1$  axis of the inertial frame. As such they are in line with the primary bodies and are called the collinear points of the RTBP. Euler discovered these points in 1765. Knowing that  $z = 0$  for all equilibrium points, one can see with a brief analysis of Eq. (2.17) that this equation is satisfied for  $y = 0$ . Finding the three collinear libration points is now a matter of

finding the roots of Eq. (2.16) for  $y = z = 0$ . This yields the equation

$$x - \frac{(1-\mu)(x-\mu)}{|x-\mu|^3} - \frac{\mu(x+1-\mu)}{|x+1-\mu|^3} = 0 \quad (2.19)$$

Clearing the denominators results in a quintic equation in  $x$ . For  $0 \leq \mu \leq 1$ , however, this equation never has more than three real roots. This equation may only be solved via numerical techniques, which will reveal the location of the equilibrium points (referred to as the  $L_1$ ,  $L_2$ , and  $L_3$  libration points).  $L_3$  is located on the far end of the larger primary body at a distance from the center of the inertial frame of slightly greater than one unit distance.  $L_1$  is located in between the two primary bodies at slightly less than one unit distance. Finally  $L_2$  is located on the far end of the smaller primary body at slightly more than one unit distance. Figure 2-2 shows the location of the libration points for the restricted three body problem.

### 2.3 Formation Flying in Orbit About an $L_2$ Point

One particular class of formation flying missions involves a satellite formation about an  $L_2$  libration point. Segerman and Zedd investigated the dynamics of relative motion for certain formation flying missions about the Earth/Moon-Sun  $L_2$  point [31]. This type of mission involves a telescope composed of distributed coplanar spacecraft about a hub spacecraft. The dynamics are analyzed based on the Circular Restricted Three Body Problem (CRTBP), the special case of the (RTBP) where the orbits of the primary bodies are assumed to be circular. This is a good approximation for the Earth/Moon-Sun system. Here, the Earth and Moon are combined to form the Earth/Moon system, which is treated as a primary body. The equations of motion for the telescope are written relative to the hub, in terms of the hub's distance from  $L_2$ . Luquette and Sanner analyzed the dynamics of relative motion about  $L_2$  for a different class of formation flying missions, subject to the constraints of the general restricted

three body problem based on the Earth/Moon-Sun system [2]. These missions are in the Leader/Follower configuration, in which a Follower spacecraft is controlled to track a Leader spacecraft. The dynamics of relative motion are defined in terms of the motion of the Follower with respect to the Leader. There is no need for direct linkage to any specific point in the RTBP reference frame. This expression for the dynamics of relative motion will be used in this research.

## 2.4 Space Environment at the $L_2$ Point

The forces that govern orbital dynamics about any of the Earth-Moon/Sun libration points include gravity, solar pressure, and thruster action.

In this formulation of the RTBP, the principal gravitational sources are the Sun and the Earth/Moon system. Here the Earth/Moon system is treated as a single body located at the system center of mass. It should be noted that although this analysis is based on the Earth/Moon-Sun system, there are no special assumptions associated with this selection. The results may be applied to any RTPB scenario with the appropriate definition of the gravitational parameters.

Consider a two-spacecraft formation about the Earth/Moon-Sun  $L_2$  point with one spacecraft designated Leader and the other Follower, as depicted in figure 2-3. Attitude Control is applied to the Leader according to mission objectives, as well as infrequent control for orbit maintenance. Control is also frequently applied to the Follower to maintain desired relative position and attitude requirements. In the scenario of this research, the desired relative position coordinates from the Leader to the Follower is  $(0 \ 0 \ -50m)$ , expressed as the difference in position of a coordinate system centered on the Leader to one centered on the Follower.

In the scenario considered in this research, the Leader and Follower spacecraft are constituent parts of an x-ray telescope with a focal length of 50 meters. The Leader

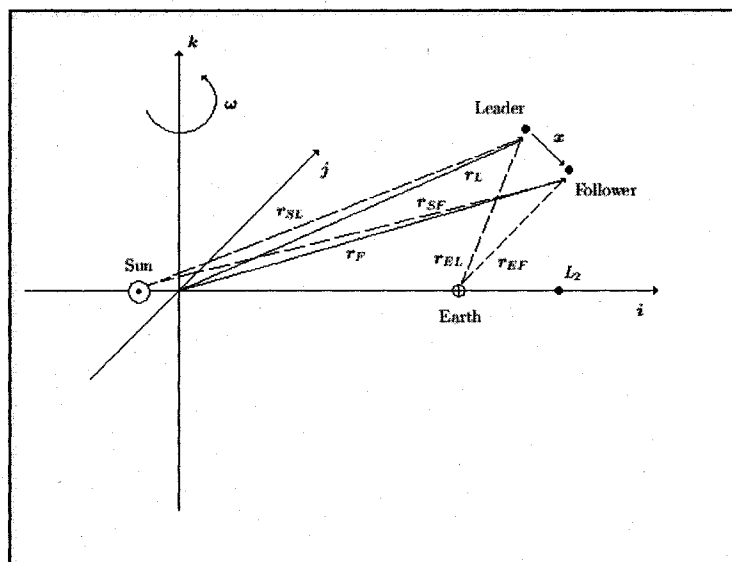


Figure 2-3: Two Spacecraft Orbiting in the Earth/Moon - Sun Rotating Frame [2]

contains x-ray optics and the Follower contains various x-ray science detectors on an optical bench. Upon receiving a signal to capture a target within its field of view, the Leader reorients itself based on the location of the target. As the repositioning of the Leader is occurring, the Follower slews and rotates as necessary to place the center of the detector optical bench at the focal point of the x-ray mirror, contained in the Leader. After the target has been acquired, the only control required on the Leader spacecraft is infrequent orbit maintenance control. As long as it is necessary to observe the target, however, frequent control must be applied to the Follower spacecraft in order to maintain the 50 meter relative position necessary for proper focus, to within sub-millimeter accuracy.

The principle environmental forces applied to a body in orbit about any Earth/Moon-Sun libration point are solar pressure and gravity. Here gravity terms take into account the two massive bodies of the RTBP as well as mutual gravitational interaction between spacecraft, also called self gravity. Luquette and Sanner assume that the spacecraft are comparably small such that their mutual gravitational interaction is



insignificant, so the self gravity term is ignored. For this example, however, the precision required in the relative position is stringent enough to warrant the inclusion of self gravity. Gravitational effects from other planets are negligible. Thruster action works in conjunction with environmental forces to drive the spacecraft dynamics. Figure 2-3 illustrates the basis for the Leader dynamics per unit mass, given by

$$\ddot{\mathbf{r}}_L = -\mu_{em} \frac{\mathbf{r}_{EL}}{\|\mathbf{r}_{EL}\|^3} - \mu_s \frac{\mathbf{r}_{SL}}{\|\mathbf{r}_{SL}\|^3} + \mathbf{f}_{solar,L} + \mathbf{f}_{sg,L} + \mathbf{f}_{pert,L} + \mathbf{u}_{thrust,L} \quad (2.20)$$

where  $\mathbf{r}_L$  is the position of the leader with respect to the inertial frame. The relative position of the Leader and Follower Spacecraft is represented by  $\mathbf{x} = \mathbf{r}_L - \mathbf{r}_F$ . The subscripts  $S$ ,  $E$  and  $L$  represent the Sun, Earth, and Leader, respectively. As such,  $\mathbf{r}_{EL}$  represents the distance between the Leader and the Earth, and  $\mathbf{r}_{SL}$  represents the distance between the Leader and the Sun. By convention, two-letter vector subscripts, as in  $\mathbf{r}_{EL}$ , for example, are interpreted by subtracting the quantity alluded to by the first letter in the subscript from that alluded to by the second letter. By this convention,  $\mathbf{r}_{EL} = \mathbf{r}_L - \mathbf{r}_E$ . The coefficients  $\mu_s$  and  $\mu_{em}$  represent the Sun and Earth/Moon system gravitational parameters, respectively. The forces of solar pressure and self gravity acting on the leader spacecraft are represented by  $\mathbf{f}_{solar,L}$  and  $\mathbf{f}_{sg,L}$ , respectively. Finally,  $\mathbf{f}_{pert,L}$  and  $\mathbf{u}_{thrust,L}$  represent disturbance forces and control forces on the Leader, respectively.

The follower dynamics per unit mass are defined similarly by

$$\ddot{\mathbf{r}}_F = -\mu_{em} \frac{\mathbf{r}_{EF}}{\|\mathbf{r}_{EF}\|^3} - \mu_s \frac{\mathbf{r}_{SF}}{\|\mathbf{r}_{SF}\|^3} + \mathbf{f}_{solar,F} + \mathbf{f}_{sg,F} + \mathbf{f}_{pert,F} + \mathbf{u}_{thrust,F} \quad (2.21)$$

where the terms are defined similarly, with the subscript  $F$  designating the Follower spacecraft.

We can find the relative acceleration vector between the Leader and Follower by taking the difference between Eqs. (2.20) and (2.21)

$$\begin{aligned}
\ddot{\mathbf{x}} &= \ddot{\mathbf{r}}_F - \ddot{\mathbf{r}}_L \\
&= -\mu_{em} \frac{\mathbf{r}_{EF}}{\|\mathbf{r}_{EF}\|^3} - \mu_s \frac{\mathbf{r}_{SF}}{\|\mathbf{r}_{SF}\|^3} + \mathbf{f}_{solar,F} + \mathbf{f}_{sg,F} + \mathbf{f}_{pert,F} + \mathbf{u}_{thrust,F} \\
&\quad - \left( -\mu_{em} \frac{\mathbf{r}_{EL}}{\|\mathbf{r}_{EL}\|^3} - \mu_s \frac{\mathbf{r}_{SL}}{\|\mathbf{r}_{SL}\|^3} + \mathbf{f}_{solar,L} + \mathbf{f}_{sg,L} + \mathbf{f}_{pert,L} + \mathbf{u}_{thrust,L} \right) \\
&= -\mu_{em} \left( \frac{\mathbf{r}_{EF}}{\|\mathbf{r}_{EF}\|^3} - \frac{\mathbf{r}_{EL}}{\|\mathbf{r}_{EL}\|^3} \right) - \mu_s \left( \frac{\mathbf{r}_{SF}}{\|\mathbf{r}_{SF}\|^3} - \frac{\mathbf{r}_{SL}}{\|\mathbf{r}_{SL}\|^3} \right) \\
&\quad + \mathbf{f}_{solar,F} - \mathbf{f}_{solar,L} + \mathbf{f}_{sg,F} - \mathbf{f}_{sg,L} + \mathbf{f}_{pert,F} - \mathbf{f}_{pert,L} \\
&\quad + \mathbf{u}_{thrust,F} - \mathbf{u}_{thrust,L} \\
&= - \left( \frac{\mu_{em}}{\|\mathbf{r}_{EF}\|^3} + \frac{\mu_s}{\|\mathbf{r}_{SF}\|^3} \right) \mathbf{x} - \mu_{em} \left( \frac{1}{\|\mathbf{r}_{EF}\|^3} - \frac{1}{\|\mathbf{r}_{EL}\|^3} \right) \mathbf{r}_{EL} \\
&\quad - \mu_s \left( \frac{1}{\|\mathbf{r}_{SF}\|^3} - \frac{1}{\|\mathbf{r}_{SL}\|^3} \right) \mathbf{r}_{SL} + \Delta \mathbf{f}_{solar} + \Delta \mathbf{f}_{sg} + \Delta \mathbf{f}_{pert} \\
&\quad + \mathbf{u}_{thrust,F} - \mathbf{u}_{thrust,L} \tag{2.22}
\end{aligned}$$

Eq. (2.22) provides the nonlinear dynamics of relative motion between the Leader and Follower spacecraft. The first term in this equation represents a parameter-based function that can be linearly combined with  $\mathbf{x}$  to form a portion of the dynamics, the second term and third terms represent gravitational effects from Earth/Moon-Sun system.

## CHAPTER 3

### THE EXTENDED KALMAN FILTER

#### 3.1 The Continuous-Time Extended Kalman Filter

The following is a description of the Extended Kalman Filter, taken directly from Gelb [32]. As described by Gelb, the Extended Kalman Filter is the natural extension of the Kalman Filter for nonlinear systems. Consider the nonlinear stochastic differential equation and a nonlinear measurement of the system of the following form

$$\dot{x}(t) = f(x(t), t) + w(t) \quad (3.1)$$

$$z_k = h_k(x_k(t_k)) + v_k, \quad K = 1, 2, \dots \quad (3.2)$$

Here  $f(x(t), t) \in \mathbb{R}^{n \times 1}$  is a nonlinear function of the state,  $w(t)$  is a zero mean gaussian noise having spectral density matrix  $Q(t)$ ,  $\{v_k\}$  is a white random sequence of zero mean gaussian random variables with associated covariance matrices  $\{R_k\}$ . An algorithm is sought for calculating the minimum variance estimate (conditional mean) of  $x(t) \in \mathbb{R}^{n \times 1}$  as a function of time and the accumulated measurement data.

Assume the measurement at time  $t_{k-1}$  has just been taken, and used to calculate the corresponding value of the conditional mean  $\bar{x}(t_{k-1})$ . No measurements are taken between  $t_{k-1}$  and  $t_k$ , and the state propagates according to Eq. (3.1), which yields the following when integrated

$$x(t) = x(t_{k-1}) + \int_{t_{k-1}}^{t_k} f(x(\tau), \tau) d\tau + \int_{t_{k-1}}^{t_k} w(\tau) d\tau \quad (3.3)$$

The expectation of both sides of this equation, is taken conditioned on all the measurements taken up to  $t_{k-1}$ . Interchanging the order of expectation and integration,

then differentiating, yields

$$\frac{d}{dt}E[\mathbf{x}(t)] = E[\mathbf{f}(\mathbf{x}(t), t)], \quad t_{k-1} \leq t < t \quad (3.4)$$

with the initial condition

$$E[\mathbf{x}(t_{k-1})] = \bar{\mathbf{x}}(t_{k-1}) \quad (3.5)$$

The conditional mean of  $\mathbf{x}(t)$  is the solution to Eq. (3.4) on the interval  $t_{k-1} \leq t < t$ , which can also be expressed more compactly as

$$\dot{\bar{\mathbf{x}}}(t) = \bar{\mathbf{f}}(\mathbf{x}(t), t), \quad t_{k-1} \leq t < t \quad (3.6)$$

where the bar denotes the expectation operation. A differential equation for the error covariance matrix

$$P(t) = E\left[[\bar{\mathbf{x}}(t) - \mathbf{x}(t)][\bar{\mathbf{x}}(t) - \mathbf{x}(t)]^T\right] \quad (3.7)$$

is derived in a similar manner by substituting for  $\mathbf{x}(t)$  in Eq. (3.7) from Eq. (3.3), interchanging the order of expectation and integration, and differentiating to yield

$$\dot{P}(t) = \overline{\mathbf{x}\mathbf{f}^T} - \bar{\mathbf{x}}\bar{\mathbf{f}}^T + \overline{\mathbf{f}\mathbf{x}^T} - \bar{\mathbf{f}}\bar{\mathbf{x}}^T + Q(t), \quad t_{k-1} \leq t < t \quad (3.8)$$

where the dependence of  $\mathbf{x}$  upon  $t$  and  $\mathbf{f}$  upon  $\mathbf{x}$  and  $t$  have been suppressed for notational convenience.

For general nonlinear systems

$$\bar{\mathbf{f}}(\mathbf{x}, t) = \int_{-\infty}^{\infty} \dots \int_{-\infty}^{\infty} \mathbf{f}(\mathbf{x}, t)p(\mathbf{x}, t)dx_1 \dots dx_n \neq \mathbf{f}(\bar{\mathbf{x}}, t) \quad (3.9)$$

where  $p(\mathbf{x}, t)$  denotes the probability density function of  $\mathbf{x}$ . Note that for general nonlinear systems  $\bar{\mathbf{f}}(\mathbf{x}, t) \neq \mathbf{f}(\bar{\mathbf{x}}, t)$ , unlike in linear systems where

$$\begin{aligned} \dot{\bar{\mathbf{x}}}(t) = \bar{\mathbf{f}}(\mathbf{x}(t), t) &= \overline{F(t)\mathbf{x}(t)} \\ &= F(t)\bar{\mathbf{x}}(t) \\ &= \mathbf{f}(\bar{\mathbf{x}}(t), t) \end{aligned} \quad (3.10)$$

Methods of computing the mean (and covariance matrix) without the knowledge of  $p(\mathbf{x}, t)$  are sought. To that end,  $\mathbf{f}$  is expanded in a Taylor series about a known vector  $\boldsymbol{\chi}(t) \approx \mathbf{x}(t)$ . The current estimate (approximation to the conditional mean)  $\hat{\mathbf{x}}$  of the state vector is chosen as  $\boldsymbol{\chi}$  so that

$$\mathbf{f}(\mathbf{x}, t) = \mathbf{f}(\bar{\mathbf{x}}, t) + \left. \frac{\partial \mathbf{f}}{\partial \mathbf{x}} \right|_{\mathbf{x}=\bar{\mathbf{x}}} (\mathbf{x} - \bar{\mathbf{x}}) + \dots \quad (3.11)$$

assuming the partial derivatives exist. Taking the expectation on both sides yields

$$\bar{\mathbf{f}}(\mathbf{x}, t) = \mathbf{f}(\bar{\mathbf{x}}, t) + \mathbf{0} + \text{H.O.T.} \quad (3.12)$$

The first-order approximation to  $\bar{\mathbf{f}}(\mathbf{x}(t), t)$  is obtained by dropping all but the first term of the power series for  $\bar{\mathbf{f}}$  and substituting the result into Eq. (3.6) to yield

$$\hat{\mathbf{x}}(t) = \mathbf{f}(\hat{\mathbf{x}}(t)), \quad t_{k-1} \leq t < t_k \quad (3.13)$$

Here  $\hat{\mathbf{x}}$  differs from  $\bar{\mathbf{x}}$  in that  $\bar{\mathbf{x}}$  denotes the exact conditional mean;  $\hat{\mathbf{x}}$  denotes an estimate of the state that is an approximation to the conditional mean. The differential equation for the error covariance is determined similarly by substituting the first two terms of the power series for  $\mathbf{f}(\mathbf{x}, t)$  into Eq. (3.8). The result after carrying out the expectation operation and combining terms is

$$\dot{P}(t) = F(\hat{\mathbf{x}}(t), t)P(t) + P(t)F^T(\hat{\mathbf{x}}(t), t) + Q(t), \quad t_{k-1} \leq t < t_k \quad (3.14)$$

Where  $F(\hat{\mathbf{x}}(t), t)$  represents the Jacobian matrix for the state, defined as

$$f_{ij}(\hat{\mathbf{x}}(t), t) = \left. \frac{\partial f_i(\mathbf{x}(t), t)}{\partial x_j(t)} \right|_{\mathbf{x}(t)=\hat{\mathbf{x}}(t)} \quad (3.15)$$

Eqs. (3.13) and (3.14) are referred to as the Extended Kalman Filter propagation equations as they are similar in structure to the Kalman Filter propagation equations for linear systems. It should be noted that the EKF propagation equations are not exact expressions for the conditional mean of the state and its associated covariance

matrix. This is because they were developed by approximating  $\bar{f}(\mathbf{x}(t), t)$  using a Taylor series expansion.

It is also necessary to develop update equations to account for the measurement data in the nonlinear case. Assuming Eqs. (3.13) and (3.14) have been used to obtain an estimate of the state  $\mathbf{x}(t)$  at time  $t_k$ , denote the solutions to these equations by  $\hat{\mathbf{x}}_k(-)$  and  $P_k(-)$ , respectively. An improved estimate of the state is sought upon the completion of the measurement  $z_k$ . Following the development of the Kalman Filter, the updated estimate is required to be a linear function of the measurement

$$\hat{\mathbf{x}}_k(+) = \mathbf{a}_k + K_k z_k \quad (3.16)$$

where the vector  $\mathbf{a}_k$  and gain matrix  $K_k$  are not yet specified. Similar to the development of the Kalman Filter, the estimation errors immediately preceding and following the update are given by

$$\begin{aligned} \tilde{\mathbf{x}}(+)&= \hat{\mathbf{x}}_k(+)-\mathbf{x}_k \\ \tilde{\mathbf{x}}(-)&= \hat{\mathbf{x}}_k(-)-\mathbf{x}_k \end{aligned} \quad (3.17)$$

The measurement error is formulated by combining Eqs. (3.16) and (3.17) with Eq. (3.2) to yield

$$\tilde{\mathbf{x}}_k(+)=\mathbf{a}_k+K_k \mathbf{h}_k\left(\mathbf{x}_k\right)+K_k \mathbf{v}_k+\tilde{\mathbf{x}}_k(-)-\hat{\mathbf{x}}_k(-) \quad (3.18)$$

As in the development of the Kalman Filter the requirement that the estimate be unbiased is imposed. As a result the expected value of the updated estimation error  $\tilde{\mathbf{x}}(+)$  is equal to  $\mathbf{0}$ . Recognizing that  $E[\tilde{\mathbf{x}}_k(-)]=E[\mathbf{v}_k]=\mathbf{0}$  and applying the latter requirement to Eq. (3.18) the result

$$\mathbf{a}_k+K_k \hat{\mathbf{h}}_k\left(\mathbf{x}_k\right)-\hat{\mathbf{x}}_k(-)=\mathbf{0} \quad (3.19)$$

is obtained. This result is then solved for  $\mathbf{a}_k$  and substituted into Eq. (3.16) to obtain

$$\hat{\mathbf{x}}_k(+)=\hat{\mathbf{x}}_k(-)+K_k\left[z_k-\hat{\mathbf{h}}_k\left(\mathbf{x}_k\right)\right] \quad (3.20)$$

Combining Eqs. (3.18) and (3.20) provides an alternative expression for the estimation error

$$\tilde{\mathbf{x}}_k(+) = \tilde{\mathbf{x}}_k(-) + K_k[\mathbf{h}_k(\mathbf{x}_k) - \hat{\mathbf{h}}_k(\mathbf{x}_k)] + K_k\mathbf{v}_k \quad (3.21)$$

Determining the optimal gain matrix  $K_k$  is accomplished in the same way as that of the Kalman Filter. First, the estimation error covariance matrix  $P_k(+)$  is expressed in terms of  $K_k$ . Then  $K_k$  is chosen to minimize a function of  $P_k(+)$ . The definition

$$P_k(+) = E[\tilde{\mathbf{x}}_k(+)\tilde{\mathbf{x}}_k(+)^T] \quad (3.22)$$

is applied to Eq. (3.21). Assuming that  $P_k(+)$  is independent of  $\mathbf{z}_k$ , recognizing that  $\mathbf{v}_k$  is uncorrelated with  $\tilde{\mathbf{x}}_k(-)$  and  $\mathbf{x}_k$ , and using the relations

$$P_k(-) = E[\tilde{\mathbf{x}}_k(-)\tilde{\mathbf{x}}_k(-)^T] \quad (3.23)$$

$$R_k = E[\mathbf{v}_k\mathbf{v}_k^T] \quad (3.24)$$

a new expression is obtained for the updated estimation error covariance matrix

$$\begin{aligned} P_k(+) &= P_k(-) + K_k E \left[ [\mathbf{h}_k(\mathbf{x}_k) - \hat{\mathbf{h}}_k(\mathbf{x}_k)][\mathbf{h}_k(\mathbf{x}_k) - \hat{\mathbf{h}}_k(\mathbf{x}_k)]^T \right] K_k^T \\ &\quad + E \left[ \tilde{\mathbf{x}}_k(-)[\mathbf{h}_k(\mathbf{x}_k) - \hat{\mathbf{h}}_k(\mathbf{x}_k)]^T \right] K_k^T \\ &\quad + K_k E \left[ [\mathbf{h}_k(\mathbf{x}_k) - \hat{\mathbf{h}}_k(\mathbf{x}_k)]\tilde{\mathbf{x}}_k(-)^T \right] + K_k R_k K_k^T \end{aligned} \quad (3.25)$$

Again, as with the case for the Kalman Filter, the estimate being sought is a minimum variance estimate, one that will minimize the class of functions

$$J_k = E \left[ \tilde{\mathbf{x}}_k(+)^T S \tilde{\mathbf{x}}_k(+)^T \right] \quad (3.26)$$

for any positive semidefinite matrix  $S$ , again chosen to be the identity matrix as it has no bearing on the optimal estimate, leading again to

$$J_k = E \left[ \tilde{\mathbf{x}}_k(+)^T \tilde{\mathbf{x}}_k(+)^T \right] = \text{trace}[P_k(+)] \quad (3.27)$$

The trace of both sides of Eq. (3.25) is taken, and the result is substituted into Eq. (3.27). The equation

$$\frac{\partial J_k}{\partial K_k} = 0 \quad (3.28)$$

is solved for  $K_k$  to yield the optimal gain matrix

$$K_k = -E \left[ \tilde{\mathbf{x}}_k(-) [\mathbf{h}_k(\mathbf{x}_k) - \hat{\mathbf{h}}_k(\mathbf{x}_k)]^T \right] \times \left\{ E \left[ [\mathbf{h}_k(\mathbf{x}_k) - \hat{\mathbf{h}}_k(\mathbf{x}_k)] [\mathbf{h}_k(\mathbf{x}_k) - \hat{\mathbf{h}}_k(\mathbf{x}_k)]^T \right] + R_k \right\}^{-1} \quad (3.29)$$

Eq. (3.29) can be substituted into Eq. (3.25), and the resulting equation can be manipulated to obtain

$$P_k(+) = P_k(-) + K_k E \left[ [\mathbf{h}_k(\mathbf{x}_k) - \hat{\mathbf{h}}_k(\mathbf{x}_k)] \tilde{\mathbf{x}}_k(-)^T \right] \quad (3.30)$$

Although Eqs. (3.20), (3.29), and (3.30) provide updating algorithms for obtaining a new estimate given a new measurement, they are impractical to implement due to their dependence on the probability density function for  $\mathbf{x}(t)$  to calculate  $\hat{\mathbf{h}}_k$ . This obstacle is overcome by expanding  $\mathbf{h}_k(\mathbf{x}_k)$  in a power series about  $\hat{\mathbf{x}}_k(-)$  as follows

$$\mathbf{h}_k(\mathbf{x}_k) = \mathbf{h}_k(\hat{\mathbf{x}}_k(-)) + H_k(\hat{\mathbf{x}}_k(-))(\mathbf{x}_k - \hat{\mathbf{x}}_k(-)) + \dots \quad (3.31)$$

where

$$H_k(\hat{\mathbf{x}}_k(-)) = \left. \frac{\partial \mathbf{h}_k(\mathbf{x})}{\partial \mathbf{x}} \right|_{\mathbf{x}=\hat{\mathbf{x}}_k(-)} \quad (3.32)$$

Truncating the above series after the first two terms, substituting the resulting approximation for  $\mathbf{h}_k(\mathbf{x}_k)$  into Eqs. (3.20), (3.29), and (3.30) and carrying out the indicated expectation operations results in the Extended Kalman Filter measurement update equations

$$\hat{\mathbf{x}}_k(+) = \hat{\mathbf{x}}_k(-) + K_k [z_k - \mathbf{h}_k(\hat{\mathbf{x}}_k(-))] \quad (3.33)$$

$$K_k = P_k(-) H_k^T(\hat{\mathbf{x}}_k(-)) \left[ H_k(\hat{\mathbf{x}}_k(-)) P_k(-) H_k^T(\hat{\mathbf{x}}_k(-)) + R_k \right]^{-1} \quad (3.34)$$

$$P_k(+) = [I - K_k H_k(\hat{\mathbf{x}}_k(-))] P_k(-) \quad (3.35)$$



Eqs. (3.13), (3.14), (3.33), (3.34), and (3.35) constitute the Extended Kalman Filter algorithm for nonlinear systems with discrete measurements. It should be noted that the gains  $K_k$  appearing in Eqs. (3.33), (3.34), and (3.35) are random variables depending on the estimate  $\hat{\mathbf{x}}(t)$  through the matrices  $F(\hat{\mathbf{x}}(t), t)$  and  $H_k(\hat{\mathbf{x}}_k(-))$ , resulting from the choice to linearize  $\mathbf{f}$  and  $\mathbf{h}_k$  about the current estimate of  $\mathbf{x}(t)$ . As a consequence, the sequence  $\{K_k\}$  cannot be pre-computed and must be determined on-line. The sequence of approximate estimation error covariance matrices  $\{P_k\}$  is also random and depends on the time history of  $\hat{\mathbf{x}}(t)$ , indicating that the estimation accuracy achieved is trajectory dependent. Using a similar limiting technique as was applied to the Kalman Filter, the Extended Kalman Filter measurement update equations can be formulated for continuous time, resulting in the following continuous time EKF measurement update equations

$$\dot{\hat{\mathbf{x}}}(t) = \mathbf{f}(\hat{\mathbf{x}}(t), t) + K(t)[z(t) - \mathbf{h}(\hat{\mathbf{x}}(t), t)] \quad (3.36)$$

$$\dot{P}(t) = F(\hat{\mathbf{x}}(t), t)P(t) + P(t)F^T(\hat{\mathbf{x}}(t), t) + Q(t) \quad (3.37)$$

$$-P(t)H^T(\hat{\mathbf{x}}(t), t)R^{-1}(t)H(\hat{\mathbf{x}}(t), t)P(t) \quad (3.38)$$

$$K(t) = P(t)H^T(\hat{\mathbf{x}}(t), t)R^{-1}(t) \quad (3.39)$$

where

$$F(\hat{\mathbf{x}}(t), t) = \left. \frac{\partial \mathbf{f}(\hat{\mathbf{x}}(t), t)}{\partial \mathbf{x}(t)} \right|_{\mathbf{x}(t)=\hat{\mathbf{x}}(t)} \quad (3.40)$$

$$H(\hat{\mathbf{x}}(t), t) = \left. \frac{\partial \mathbf{h}(\hat{\mathbf{x}}(t), t)}{\partial \mathbf{x}(t)} \right|_{\mathbf{x}(t)=\hat{\mathbf{x}}(t)} \quad (3.41)$$

## CHAPTER 4

### SLIDING MODE OBSERVERS

#### 4.1 Sliding Mode Observers

Sliding Mode Observers (SMO) are nonlinear state estimators whose development stems from the theory of variable structure systems. Some advantages of the SMO include robustness to bounded system parameter uncertainties and input disturbances.

As a foundation for understanding the SMO, sliding mode behavior is described in the venue of sliding mode control. These concepts are then extended to estimation. This discussion is similar in content to the work done by Misawa [29] and Koprubasi [3].

Begin with a general nonlinear system model

$$x^{(n)}(t) = f(x(t)) + b(x(t))u(t) + d(t) \quad (4.1)$$

where  $x$  is the scalar output of interest,  $\mathbf{x} = [x, \dot{x}, \dots, x^{(n-1)}]^T$  represents the state,  $b(x; t)$  and  $u(t)$  represent the control gain and scalar control input, respectively, and the superscript  $n$  represents the  $n^{\text{th}}$  time derivative. The function  $f(x; t)$  is unknown, but is assumed to have known bounds. The same is true for the input disturbance  $d(t)$ .

The task in controlling this system is to force the system state to track a desired state  $\mathbf{x}_d = [x_d, \dot{x}_d, \dots, x_d^{(n-1)}]^T$  despite the previously mentioned model uncertainties and unknown input disturbances. To that end, one must introduce a time-varying sliding surface  $s(\tilde{\mathbf{x}}, t) = 0$  based on the tracking error vector  $\tilde{\mathbf{x}} = \mathbf{x} - \mathbf{x}_d = [\tilde{x}, \dot{\tilde{x}}, \dots, \tilde{x}^{(n-1)}]^T$ . This surface is often chosen to be

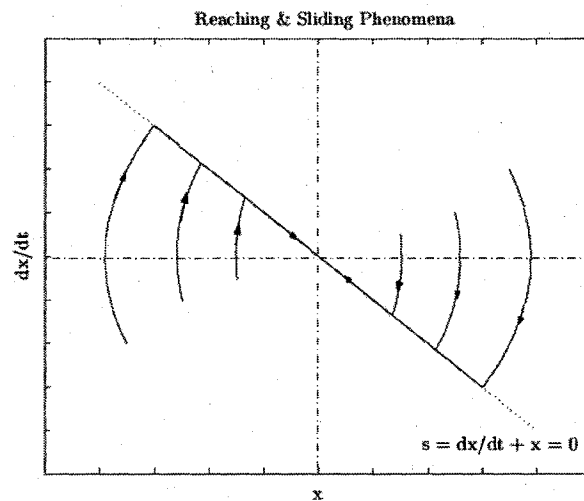


Figure 4-1: Reaching And Sliding Phenomena of Sample State Trajectories on the Phase Plane [3]

$$s(\tilde{x}, t) = \left( \frac{d}{dt} + \lambda \right)^{n-1} \tilde{x}, \quad \lambda > 0 \quad (4.2)$$

where  $\lambda$  represents some positive constant.

The following is an example of sliding mode control applied to a system in the absence of input disturbances. This example demonstrates exponential error convergence and necessity for a discontinuous control law, with Figure 4-1 showing the sliding condition.

Applying Eq.(4.2) to the system

$$\ddot{x} = f(x, \dot{x}) \quad (4.3)$$

yields a possible (out of many) sliding surface

$$s = \dot{\tilde{x}} + \lambda \tilde{x} \quad (4.4)$$

To accurately track a desired state  $x_d$ , the error trajectories must be made to

remain on the sliding surface, therefore  $s(\tilde{\mathbf{x}}, t) = 0$ . Those error trajectories which fall outside of the sliding surface must be redirected toward  $s(t)$  by an appropriate control law. Since the sliding surface  $s(\tilde{\mathbf{x}}, t)$  is required to be zero, the solution  $\tilde{\mathbf{x}} = \tilde{\mathbf{x}}_0 e^{-\lambda t}$  is obtained. This guarantees exponential convergence as  $\lambda$  is a positive constant.

The control law is required to satisfy Eq.(4.5), referred to as the *sliding condition*.

$$\frac{1}{2} \frac{d}{dt} s^2(\tilde{\mathbf{x}}, t) \leq -\eta |s| \quad \eta > 0 \quad (4.5)$$

By Lyapunov stability ( $V = s^2$ ), the sliding condition guarantees that the sliding surface is attractive. Solving Eq.(4.5) for the equality yields

$$s \dot{s} = -\eta |s| \Rightarrow \dot{s} = -\eta \operatorname{sgn}(s) \quad (4.6)$$

where

$$\operatorname{sgn}(s) = \begin{cases} +1 & \text{if } s > 0 \\ -1 & \text{if } s < 0 \end{cases} \quad (4.7)$$

represents the signum function. This demonstrates the discontinuous nature of sliding mode behavior. Finally the sliding surface becomes

$$s(t) = s(0) \pm \eta t \quad (4.8)$$

If met, the sliding condition guarantees via Lyapunov stability analysis that the error trajectories will reach the sliding surface in finite time  $t_{reach}$  where

$$t_{reach} < |s(0)|/\eta \quad (4.9)$$

Having chosen the sliding surface using Eq. (4.2), it is necessary to select a control law  $u$  that satisfies Eq. (4.5), i.e. such that there exists a valid Lyapunov function ( $V = s^2$ ).

The principles of sliding mode control can be applied to the design of observers. However, in estimation, a sliding surface definition analog to Eq. (4.2) is not adequate,

as the full state is not available for measurement. Slotine et al. formulated an observer for second order systems with a single measurement [30], and further extended this observer for  $n$ th-order and multi-output systems. This work goes on to prove stability for these systems, which are of the form

$$\begin{aligned}\dot{\mathbf{x}} &= \mathbf{A}\mathbf{x} + \mathbf{D} \\ \mathbf{z} &= \mathbf{C}\mathbf{x}\end{aligned}\quad (4.10)$$

Here the system and measurement matrices are represented by  $\mathbf{A} \in \mathbb{R}^{n \times n}$  and  $\mathbf{C} \in \mathbb{R}^{m \times n}$ , respectively, with  $\mathbf{D} \in \mathbb{R}^n$  representing lumped nonlinearities and uncertainties, such that  $|\mathbf{D}| \leq D_o$ .

The observer design proposed in [29] assumes a nonlinear, observable system with a linear measurement model

$$\begin{aligned}\dot{\mathbf{x}} &= \mathbf{f}(\mathbf{x}, t), & \mathbf{x} \in \mathbb{R}^n \\ \mathbf{z} &= \mathbf{C}\mathbf{x} + \nu, & \mathbf{z} \in \mathbb{R}^m\end{aligned}\quad (4.11)$$

The proposed observer design is of the form

$$\dot{\hat{\mathbf{x}}} = \hat{\mathbf{f}}(\hat{\mathbf{x}}, t) + \mathbf{H}\tilde{\mathbf{z}} + \mathbf{K}\mathbf{1}_s \quad (4.12)$$

Where the vector of state estimates is  $\hat{\mathbf{x}} \in \mathbb{R}^n$ ,  $\hat{\mathbf{f}}(\hat{\mathbf{x}}(t))$  represents the model of  $\mathbf{f}(\mathbf{x}(t))$ ,  $\mathbf{H} \in \mathbb{R}^{n \times m}$  and  $\mathbf{K} \in \mathbb{R}^{n \times r}$  are constant gain matrices, as yet unspecified, and  $r$  represents the number of sliding surfaces. The  $m \times 1$  vector  $\mathbf{1}_s$  represents any suitable switching function, e.g. the signum function

$$\mathbf{1}_s = [\text{sgn}(\tilde{z}_1) \quad \text{sgn}(\tilde{z}_2) \quad \dots \quad \text{sgn}(\tilde{z}_m)]^T \quad (4.13)$$

where

$$\tilde{\mathbf{z}} = \mathbf{z} - \hat{\mathbf{z}} = \mathbf{z} - \mathbf{C}\hat{\mathbf{x}} \quad (4.14)$$

One may choose to use a saturation function instead of the signum function. To do so, it is necessary to design a diagonal matrix  $\Phi$ , containing a boundary layer

$\phi_i$  for each sliding surface (there may be multiple sliding surfaces employed in a given Sliding Mode Observer). These boundary layers are scalar constants that relax the requirement that  $\mathbf{s} = 0$ . Rather, estimation error trajectories are considered satisfactory if they satisfy  $s_i \leq \phi_i$ . The saturation function is often favored over the signum function because, when used with  $\Phi$ , it eliminates most high amplitude chatter associated with switching in each of the sliding surface functions. Such chatter occurs when the switching action of the signum function causes the estimates to oscillate about the actual values at high frequencies. Another advantage of the boundary layer is that the steady-state error may be adjusted by changing the value of the boundary layer.

The sliding surface  $\mathbf{s}$  in Eq. (4.2) can be extended for multivariable systems as the  $m$  dimensional vector

$$\mathbf{s} = \mathbf{C}\tilde{\mathbf{x}} = \mathbf{C}(\mathbf{x} - \hat{\mathbf{x}}) \quad (4.15)$$

The error dynamics are determined by Eqs. (4.11) and (4.12) as

$$\dot{\tilde{\mathbf{x}}} = \Delta\mathbf{f} - \mathbf{H}\tilde{\mathbf{z}} - \mathbf{K}\mathbf{1}_s \quad (4.16)$$

where

$$\Delta\mathbf{f} = \mathbf{f}(\mathbf{x}, t) - \hat{\mathbf{f}}(\hat{\mathbf{x}}, t), \quad |\Delta\mathbf{f}| < \xi, \quad \xi > 0 \quad (4.17)$$

The extent of the imprecision  $|\Delta\mathbf{f}|$  on  $\mathbf{f}(\mathbf{x}, t)$  is bounded and known to not exceed  $\xi$ . For notational convenience, Eq. (4.16) is rewritten as

$$\dot{\tilde{\mathbf{x}}} = \tilde{\mathbf{f}}, \quad \tilde{\mathbf{f}} = \Delta\mathbf{f} - \mathbf{H}\tilde{\mathbf{z}} - \mathbf{K}\mathbf{1}_s \quad (4.18)$$

The  $m$  dimensional surface,  $\mathbf{s} = 0$  will be attractive if

$$s_i \dot{s}_i < 0, \quad i = 1, 2, \dots, m \quad (4.19)$$

and sliding is achieved if the extended sliding condition is met

$$s_i \dot{s}_i \leq -\eta |s_i|, \quad i = 1, 2, \dots, m \quad (4.20)$$

Eqs. (4.20) defines the sliding surface, chosen considering Lyapunov stability criteria. The sliding surface is chosen such that the energy function  $V(t)$  is positive and its derivative is negative definite. During sliding, the system dynamics are reduced from an  $n^{\text{th}}$  order system to an  $(n - m)$  equivalent or reduced order system. The approximate sliding dynamics of the reduced order manifold can be modelled using the *equivalent control* method [25]. During sliding, the switching term  $\mathbf{1}_s$  acts to assure  $\mathbf{s} = \dot{\mathbf{s}} = \mathbf{0}$ . The latter condition

$$\frac{\partial \mathbf{s}}{\partial \tilde{\mathbf{x}}} \cdot \tilde{\mathbf{f}} = \mathbf{0} \quad (4.21)$$

can be used in conjunction with Eqs. (4.16) and (4.18) to obtain an expression for the equivalent switching vector.

$$\mathbf{C}(\Delta \mathbf{f} - \mathbf{H}\tilde{\mathbf{z}} - \mathbf{K}\mathbf{1}_s) = \mathbf{0} \quad (4.22)$$

so that

$$\mathbf{1}_s = (\mathbf{C}\mathbf{K})^{-1}\mathbf{C}\Delta \mathbf{f} \quad (4.23)$$

Therefore, the equivalent dynamics on the reduced order manifold are given as

$$\begin{aligned} \dot{\tilde{\mathbf{x}}} &= (\mathbf{I} - \mathbf{K}(\mathbf{C}\mathbf{K})^{-1}\mathbf{C})\Delta \mathbf{f} \\ \mathbf{C}\tilde{\mathbf{x}} &= \mathbf{0} \end{aligned} \quad (4.24)$$

The absence of the Luenberger gain matrix,  $\mathbf{H}$ , in Eq. (4.24) marks the independence of the reduced order manifold dynamics on these linear gains. The Luenberger gains serve to force the initial error trajectory toward the sliding surface. The switching gain matrix,  $\mathbf{K}$ , is chosen to ensure stable error dynamics on the reduced order manifold. To that end,  $\mathbf{K}$  is chosen, in order to satisfy Lyapunov stability, to be larger than known modelling uncertainties and disturbances, that is

$$K_i > \xi + D_o. \quad (4.25)$$

## CHAPTER 5

### SIMULATION CHARACTERISTICS

#### 5.1 Formation Flying Scenario

The performance of the Sliding Mode Observer and the Extended Kalman Filter are compared against one another through implementation into a simulated formation flying mission about the Earth/Moon-Sun  $L_2$  libration point. The name of this mission is Constellation X (Con-X), a previously proposed NASA mission involving two satellites in the Leader/Follower formation discussed in Chapter 1, utilizing the VISNAV measurement system, discussed later in this chapter. The Leader and Follower satellites of the Con-X mission form an x-ray telescope with a focal length of 50 meters. This formation is maintained while in halo orbit about the Earth/Moon-Sun  $L_2$  point, with a nominal distance of 300,000 km and orbital period of 6 months. The Leader telescope is also called the mirror spacecraft (MSC), while the Follower is called the detector spacecraft (DSC). The MSC and DSC are controlled to maintain a separation distance of 50 meters to an accuracy of within 1 millimeter. This design requirement follows from the fact that the focal length of the x-ray telescope formed by the MSC and DSC is 50 meters. Therefore, the relative positioning of these two satellite must be maintained for proper focus.

The Leader contains x-ray optics and the Follower contains various x-ray science detectors on an optical bench. Upon receiving a signal to capture a target within its field of view, the Leader reorients itself based on the location of the target. As the repositioning of the Leader is occurring, the Follower slews and rotates as necessary



to place the center of the detector optical bench at the focal point of the x-ray mirror, contained in the Leader. After the target has been acquired, the only control required on the Leader spacecraft is infrequent orbit maintenance control. As long as it is necessary to observe the target, however, frequent control must be applied to the Follower spacecraft in order to maintain the 50 meter relative position necessary for proper focus, to within sub-millimeter accuracy.

The system model for the Constellation X mission is

$$\ddot{\mathbf{x}} = [\mathbf{A} + \Delta\mathbf{A}(t)]\mathbf{x} + \mathbf{f}(\mathbf{x}, t) + \mathbf{u}_{thrust}(t) + [\boldsymbol{\Gamma}(t) + \Delta\boldsymbol{\Gamma}(t)] + \mathbf{D}(t) \quad (5.1)$$

where  $\mathbf{x} \in \mathbb{R}^{3 \times 1} = \mathbf{r}_F - \mathbf{r}_L$ , the distance between the Leader and Follower spacecraft, and  $\mathbf{u}_{thrust}(t)$  represents control effort. Note that, unlike in Eq. (2.22), the state-dependent self-gravity term is included

$$\mathbf{f}(\mathbf{x}, t) = \frac{G\mathbf{x}}{\|\mathbf{x}\|^3} (M_{MSC} - M_{DSC}) \quad (5.2)$$

where  $G = 6.6726 \times 10^{-20} \frac{km^3}{kg \cdot s^2}$  represents Newton's universal gravitational constant, and  $M_{MSC} = 6000$  and  $M_{DSC} = 3000$  represent the mass of the Leader and Follower spacecraft, respectively.

The terms  $[\mathbf{A} + \Delta\mathbf{A}(t)]$  and  $[\boldsymbol{\Gamma}(t) + \Delta\boldsymbol{\Gamma}(t)]$  represent the linear system matrix and gravitational effects from the Sun and Earth/Moon system and solar pressure, respectively. The distance of the satellites from the Earth and the Sun ( $\mathbf{r}_{EF}(t)$ ,  $\mathbf{r}_{EL}(t)$ ,  $\mathbf{r}_{SF}(t)$ , and  $\mathbf{r}_{SL}(t)$ ) are not assumed to be continuously available. This orbital information is updated every seven days with information provided by a ground station. A review of Figure 2-3 shows that only the quantities  $\mathbf{r}_{SE}$  (the Earth's distance from the Sun - not shown), and  $\mathbf{r}_{EL}$  (the distance between the Leader and the Sun) are required in the update procedure. The required orbital parameters  $\mathbf{r}_{EF}(t)$ ,  $\mathbf{r}_{EL}(t)$ ,  $\mathbf{r}_{SF}(t)$ , and  $\mathbf{r}_{SL}(t)$  are calculated through the following relationships, with inaccuracies carrying

through from the inaccuracies in  $\mathbf{r}_{SE}$  and  $\mathbf{r}_{EL}$

$$\begin{aligned}\mathbf{r}_{EF} &= \mathbf{r}_{EL} + \mathbf{x} \\ \mathbf{r}_{SF} &= \mathbf{r}_{SE} + \mathbf{r}_{EL} + \mathbf{x} \\ \mathbf{r}_{SL} &= \mathbf{r}_{SE} + \mathbf{r}_{EL}\end{aligned}\tag{5.3}$$

Because of time between updates, time-dependent, parametric uncertainties exist in  $\mathbf{A}$  and  $\mathbf{\Gamma}(t)$ . This problem is addressed by defining orbital parameters  $\mathbf{r}_{EF}, \mathbf{r}_{SF}, \mathbf{r}_{EL}$ , and  $\mathbf{r}_{SL}$  such that

$$\mathbf{r}(t) = \bar{\mathbf{r}}(t) + \delta\mathbf{r}(t)\tag{5.4}$$

where  $\bar{\mathbf{r}}$  and  $\delta\mathbf{r}$  represent the nominal value and time-varying uncertainties in  $\mathbf{r}$ , respectively. Eq. (5.1) is defined with the following

$$[\mathbf{A} + \Delta\mathbf{A}(t)] = \left[ - \left( \frac{\mu_{EM}}{\|\mathbf{r}_{EF}(t)\|^3} + \frac{\mu_S}{\|\mathbf{r}_{SF}(t)\|^3} \right) \right] \mathbf{I}^3\tag{5.5}$$

where  $\mathbf{I}^3$  represents an identity matrix of size three, and

$$\begin{aligned}[\mathbf{\Gamma}(t) + \Delta\mathbf{\Gamma}(t)] &= -\mu_{EM} \left( \frac{1}{\|\mathbf{r}_{EF}(t)\|^3} + \frac{1}{\|\mathbf{r}_{EL}(t)\|^3} \right) \mathbf{r}_{EL}(t) \\ &\quad -\mu_S \left( \frac{1}{\|\mathbf{r}_{SF}(t)\|^3} + \frac{1}{\|\mathbf{r}_{SL}(t)\|^3} \right) \mathbf{r}_{SL}(t) + \Delta\mathbf{f}_{solar}\end{aligned}\tag{5.6}$$

where  $\Delta\mathbf{f}_{solar}$  represents input disturbances from solar pressure. All other uncertainties are lumped into the uncertainty term

$$\mathbf{D}(t) = \Delta\mathbf{f}_{pert} + \Delta\mathbf{u}_{thrust,F} - \Delta\mathbf{u}_{thrust,L}\tag{5.7}$$

Here  $\Delta\mathbf{f}_{pert}$  represents any other perturbation forces, and  $\Delta\mathbf{u}_{thrust,L}$  and  $\Delta\mathbf{u}_{thrust,F}$  take into account thrust uncertainties in the MSC and DSC, respectively.

## 5.2 VISNAV Measurement System

Formation flying requires precise measurement of the relative positions and attitudes of all spacecraft in the formation. For a formation flying mission involving satellites orbiting the Earth/Moon-Sun  $L_2$  libration point, this point's 1,500,000 kilometer

distance from Earth precludes the possibility of using GPS or any other Earth-based orbit determination system to provide this information. Such techniques would not yield suitable accuracy in relative position and attitude estimation. In order to obtain measurements of adequate accuracy, on-board measurement systems must be used. For formation flying missions beyond the GPS constellation, the Visual Navigation (VISNAV) system developed by Crassidis et al. is a suitable method for obtaining on-board relative position and attitude measurements [7].

The VISNAV system utilizes an electro-optical sensor placed on one spacecraft to detect the light emitted by a beacon on another spacecraft, yielding relative position and attitude estimates. The sensor contains a Position Sensing Diode (PSD) placed in the focal plane of a wide angle lens. Incoming light from the beacons is focused by the lens, illuminating some part of the rectangular silicon area of the PSD. The PSD is wired to generate electrical currents in four directions which provide the information necessary to calculate the energy centroid on the PSD. The imbalances in these currents are almost linearly proportional to the location of this centroid. After calculation, the  $x$  and  $y$  coordinates of the centroid can be calculated. It is then possible to determine the incident direction of this light on the wide angle lens. In this way the sensors are able to supply directional vector readings pointing to the beacons. Three beacon-sensor pairs between spacecraft provide enough information to designate a unique relative position and attitude. In this study, four beacon-sensor pairs are used. The VISNAV concept is demonstrated in Figure 5-1.

The reason the sensors are only able to detect light from the beacons, as opposed to other ambient light sources, is that the beacon light is modulated at a known frequency, while the currents generated on the PSD are driven through an active filter set on the same frequency. This makes for excellent rejection of ambient light under many operating conditions. Other advantages include the compactness of the sensor

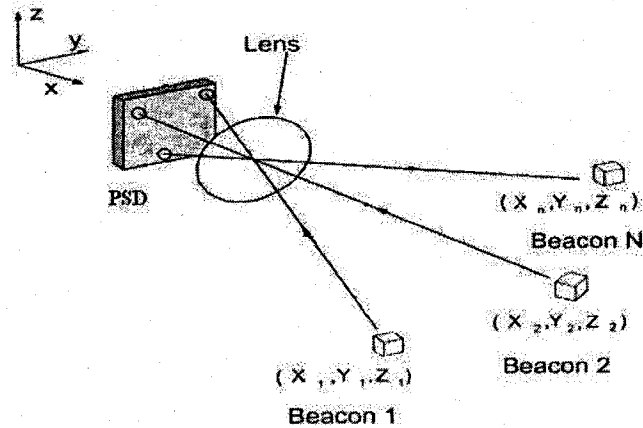


Figure 5-1: VISNAV Measurement System

size and wide field of view due to the use of a wide angle lens in the electro-optical sensors. The VISNAV system also benefits from having relatively simple electronic circuitry and low signal processing requirements, which ease the computational burden on the microprocessors. These advantages make the VISNAV system a reliable tool to aid in relative position and attitude estimation for formation flying missions.

### 5.2.1 Measurement Model

The VISNAV system is to be implemented to provide relative position estimation for a two-satellite formation flying scenario in a halo orbit about the Earth/Moon-Sun system's  $L_2$  point. For this research, the attitudes of the satellites in the formation are assumed to be perfectly known and, without loss of generality, are considered to be identity.

The basic nonlinear measurement model is

$$\mathbf{b}_i = R_{rel}\mathbf{r}_i + \boldsymbol{\nu}_i = \mathbf{r}_i + \boldsymbol{\nu}_i \quad (5.8)$$

Here,  $\mathbf{b}_i$  represents the measured unit vector for the  $i^{th}$  beacon,  $\boldsymbol{\nu}_i$  represents zero-

mean random measurement noise, and  $R_{rel}$  represents the relative attitude matrix, here assumed to be the identity matrix. The true unit vector  $\mathbf{r}_i$  is defined as

$$\mathbf{r}_i = \frac{1}{\sqrt{(X_i - x)^2 + (Y_i - y)^2 + (Z_i - z)^2}} \begin{bmatrix} X_i - x \\ Y_i - y \\ Z_i - z \end{bmatrix} \quad (5.9)$$

Here,  $(X_i, Y_i, Z_i)$  represent the coordinates of the  $i^{th}$  beacon with respect to the body-fixed coordinates of the Leader spacecraft (the spacecraft carrying the beacon), while  $(x, y, z)$  represents the relative position coordinates between the frames of the two spacecraft carrying the beacon-sensor pair.

### 5.2.2 Simulation Conditions

The following conditions apply to both the Extended Kalman Filter and Sliding Mode Observer implementation. The relative attitudes of the MSC and DSC from Eq. (5.8) are assumed to be perfectly known and held constant at identity. As such, the subject of interest is relative position and velocity estimation. To test the reliability of initial startup, the desired separation distance,  $\mathbf{x}_d(0)$ , the actual values of the MSC and DSC relative position,  $\mathbf{x}(0)$ , and the initial values of the estimator state estimates,  $\hat{\mathbf{x}}(0)$ , are initialized at different values

$$\begin{aligned} \mathbf{x}_d(0) &= [0, 0, -50m]^T \\ \mathbf{x}(0) &= [10.4815m, -20.7256m, -44.2785m]^T \\ \hat{\mathbf{x}}(0) &= [11.5927m, -22.7981m, -48.7064m]^T \end{aligned}$$

All estimate and actual relative velocities are initialized at rest

$$\begin{aligned} \dot{\mathbf{x}}_d(0) &= \mathbf{0} \\ \dot{\mathbf{x}}(0) &= \mathbf{0} \\ \dot{\hat{\mathbf{x}}}(0) &= \mathbf{0} \end{aligned}$$

In the Con-X mission, the MSC and DSC are subject to disturbance accelerations from solar pressure, self gravity, and thruster action, averaging  $10^{-6} N/kg$ . Input uncertainties (due to thruster errors, external disturbances, etc.) are applied to the system as periodic and random forcing functions

$$\begin{aligned} d_x &= 0.25 \times 10^{-6} \sin(2.22\pi t) + \sigma_x \\ d_y &= 0.06 \times 10^{-6} \sin(.0074\pi t) + \sigma_y \\ d_z &= 0.10 \times 10^{-6} \sin(1.4\pi t) + \sigma_z \end{aligned} \quad (5.10)$$

Here,  $\sigma_x, \sigma_y$  and  $\sigma_z$  are independent, zero-mean, random input pulses of 5Hz, the same as the VISNAV measurement sample rate. These thrust disturbances are measured in Newtons per unit mass, with an average intensity level of  $0.5 \times 10^{-6} N/Kg$ . Inaccuracies are also introduced to the system in the form of parameter uncertainties in  $r_{SE}$  and  $r_{EL}$  because orbital updates are available once every seven days.

Finally, the VISNAV system used in the simulation utilizes four beacons on the front side of the MSC. These beacons are assumed to be in the line of sight of the detectors located on the DSC. The coordinates of these beacons with respect to the MSC body-fixed inertial coordinates (in meters) are given as

$$\begin{aligned} L_1 &= [-5.5, 3.5, -0.5] \\ L_3 &= [-5.5, -3.5, -0.5] \\ L_5 &= [1.5, 3.5, -0.5] \\ L_7 &= [1.5, -3.5, -0.5] \end{aligned}$$

Here, odd-numbered beacons are located on the back of the Leader spacecraft, facing the Follower. The unmentioned even-numbered spacecraft are on the front of the Leader, pointing away from the follower. For this research, Follower spacecraft is assumed to be in view of all of the odd-numbered beacons.

All VISNAV directional measurements are corrupted with measurement noise, chosen by NASA designers to be such that it would amount to noise levels of 0.0005 degrees on each beacon axis. After this corruption, the vector measurements are normalized once again to satisfy the requirement that VISNAV directional measurements be unit directional vectors. All simulations are performed using MATLAB/Simulink.

### 5.3 Control Law

For both the EKF and the SMO, observer estimates will provide relative positions and velocity updates to an adaptive controller to maintain satellite relative position, as developed by Luquette and Sanner [33]. The control law is known to be globally stable in the absence of uncertainties and is able to perfectly track desired smooth trajectories. The required differential thrust per unit mass is determined by the control law

$$\begin{aligned}
 \mathbf{u}_{thrust,F} - \mathbf{u}_{thrust,L} &= \ddot{\mathbf{x}}_r + [I \ R_{ri}^T] + \begin{bmatrix} \hat{\Theta}_1 \\ \hat{\Theta}_2 \end{bmatrix} - K_T \mathbf{s}_T \\
 &= \ddot{\mathbf{x}}_r + \Gamma_t \hat{\Theta}_T - K_T \mathbf{s}_T \\
 \dot{\hat{\Theta}}_t &= -\gamma \Gamma_t^T \mathbf{s}_T
 \end{aligned} \tag{5.11}$$

Here  $\ddot{\mathbf{x}}_r$  is a reference acceleration based on a reference velocity

$$\ddot{\mathbf{x}}_r = \dot{\mathbf{x}}_d - \Lambda_T (\mathbf{x} - \mathbf{x}_d)$$

with  $\mathbf{x}_d$  and  $\dot{\mathbf{x}}_d$  representing the desired relative position and velocity. The matrix  $R_{ri}$  provides the transformation from an inertial reference frame to that of the Earth/Moon-Sun rotating frame.  $\Lambda_T$  and  $K_T$  are constant, symmetric, positive-definite gain matrices.  $\hat{\Theta}_1$  and  $\hat{\Theta}_2$  represent adaptive estimates of unknown constant system vectors (e.g., uncertainties in absolute position and velocity and unknown

perturbing forces). The control law uses the error signal  $s_T$  computed as

$$s_T = \dot{x} - \dot{x}_d + \Lambda_T(x - x_d) = \dot{x} - \dot{x}_r$$

Eqs. (5.11) and (5.11) provide asymptotic stability of the tracking error. A detailed stability analysis is provided in [33].



## CHAPTER 6

# EXTENDED KALMAN FILTER FOR FORMATION FLYING

### 6.1 Extended Kalman Filter Simulations

The Extended Kalman Filter (EKF) is the direct extension of the Kalman filter for nonlinear state estimation problems. The Kalman gain  $K(t)$  is calculated by linearizing the system and measurement model equations at the current state estimate  $\hat{x}$ .

For the continuous Extended Kalman Filter, the following system model is assumed

$$\begin{aligned}\dot{x}(t) &= f(x(t), t) + w(t) && N(\mathbf{0}, Q(t)) \\ z(t) &= h(x(t), t) + v(t) && N(\mathbf{0}, R(t))\end{aligned}\tag{6.1}$$

where  $w(t)$  and  $v(t)$  represent uncorrelated zero-mean gaussian state and measurement noise with intensities  $Q(t)$  and  $R(t)$ , respectively.

The state estimates are propagated by integrating the state estimate equation

$$\dot{\hat{x}}(t) = f(\hat{x}(t), t) + K(t)[z(t) - h(\hat{x}(t), t)]\tag{6.2}$$

where the Kalman gain  $K(t)$  is calculated using the error covariance matrix  $P(t)$

upon integrating the error covariance equation

$$\begin{aligned}\dot{P}(t) &= F(\hat{\mathbf{x}}(t), t)P(t) + P(t)F^T(\hat{\mathbf{x}}(t), t) + Q(t) \\ &\quad - P(t)H^T(\hat{\mathbf{x}}(t), t)R^{-1}(t)H(\hat{\mathbf{x}}(t), t)P(t) \\ K(t) &= P(t)H^T(\hat{\mathbf{x}}(t), t)R^{-1}(t)\end{aligned}$$

The system state is defined as the relative position and velocity between the two spacecraft.

$$\mathbf{x}(t) = \begin{bmatrix} x \\ y \\ z \\ \dot{x} \\ \dot{y} \\ \dot{z} \end{bmatrix} \quad (6.3)$$

Also required for the error covariance and Kalman gain equations are the Jacobi for the system and measurement. The Jacobian matrix for the state

$$\begin{bmatrix} \dot{\hat{\mathbf{x}}} \\ \ddot{\hat{\mathbf{x}}} \end{bmatrix} = \begin{bmatrix} 0 & I \\ \mathbf{A} + \Delta\mathbf{A} & 0 \end{bmatrix} \begin{bmatrix} \hat{\mathbf{x}} \\ \dot{\hat{\mathbf{x}}} \end{bmatrix} + \begin{bmatrix} 0 \\ \hat{\Upsilon}(\hat{\mathbf{x}}, t) \end{bmatrix} \quad (6.4)$$

where  $\hat{\Upsilon}(\hat{\mathbf{x}}, t) = \hat{\mathbf{f}}(\hat{\mathbf{x}}, t) + \mathbf{u}_{thrust}(t) + [\Gamma(t) + \Delta\Gamma(t)] + \mathbf{D}(t)$  from Eq. 5.1, is

$$\begin{aligned}F(\hat{\mathbf{x}}(t), \mathbf{u}(t), t) &= \left. \frac{\partial \mathbf{f}(\mathbf{x}(t), t)}{\partial \mathbf{x}(t)} \right|_{\mathbf{x}(t)=\hat{\mathbf{x}}(t)} \\ &= \begin{bmatrix} 0 & 0 & 0 & 1 & 0 & 0 \\ 0 & 0 & 0 & 0 & 1 & 0 \\ 0 & 0 & 0 & 0 & 0 & 1 \\ 0 & 0 & 0 & a & b & c \\ 0 & 0 & 0 & d & e & f \\ 0 & 0 & 0 & g & h & i \end{bmatrix} \quad (6.5)\end{aligned}$$

where

$$\begin{aligned}
 a &= - \left( \frac{\mu_{EM}}{\|\mathbf{r}_{EF}(t)\|^3} + \frac{\mu_S}{\|\mathbf{r}_{SF}(t)\|^3} \right) + \frac{3G(M_{MSC} + M_{DSC})\hat{x}^2}{(\hat{x}^2 + \hat{y}^2 + \hat{z}^2)^{\frac{5}{2}}} \\
 &\quad - \frac{G(M_{MSC} + M_{DSC})}{(\hat{x}^2 + \hat{y}^2 + \hat{z}^2)^{\frac{3}{2}}} \\
 b, d &= \frac{3G(M_{MSC} + M_{DSC})\hat{x}\hat{y}}{(\hat{x}^2 + \hat{y}^2 + \hat{z}^2)^{\frac{5}{2}}} \\
 c, g &= \frac{3G(M_{MSC} + M_{DSC})\hat{x}\hat{z}}{(\hat{x}^2 + \hat{y}^2 + \hat{z}^2)^{\frac{5}{2}}} \\
 e &= - \left( \frac{\mu_{EM}}{\|\mathbf{r}_{EF}(t)\|^3} + \frac{\mu_S}{\|\mathbf{r}_{SF}(t)\|^3} \right) + \frac{3G(M_{MSC} + M_{DSC})\hat{y}^2}{(\hat{x}^2 + \hat{y}^2 + \hat{z}^2)^{\frac{5}{2}}} \\
 &\quad - \frac{G(M_{MSC} + M_{DSC})}{(\hat{x}^2 + \hat{y}^2 + \hat{z}^2)^{\frac{3}{2}}} \\
 f, h &= \frac{3G(M_{MSC} + M_{DSC})\hat{y}\hat{z}}{(\hat{x}^2 + \hat{y}^2 + \hat{z}^2)^{\frac{5}{2}}} \\
 i &= - \left( \frac{\mu_{EM}}{\|\mathbf{r}_{EF}(t)\|^3} + \frac{\mu_S}{\|\mathbf{r}_{SF}(t)\|^3} \right) + \frac{3G(M_{MSC} + M_{DSC})\hat{z}^2}{(\hat{x}^2 + \hat{y}^2 + \hat{z}^2)^{\frac{5}{2}}} \\
 &\quad - \frac{G(M_{MSC} + M_{DSC})}{(\hat{x}^2 + \hat{y}^2 + \hat{z}^2)^{\frac{3}{2}}}
 \end{aligned}$$

The Jacobian of the measurement,

$$H(\hat{\mathbf{x}}(t), t) = \left. \frac{\partial \mathbf{h}(\mathbf{x}(t), t)}{\partial \mathbf{x}(t)} \right|_{\mathbf{x}(t)=\hat{\mathbf{x}}(t)} \quad (6.6)$$

is the augmented matrix of the Jacobian of each of  $l$  measurements evaluated at the estimate, such that

$$H(\hat{\mathbf{x}}(t), t) = \left[ \begin{array}{cccc} \frac{\partial z_1(t)}{\partial \mathbf{x}(t)} & \frac{\partial z_2(t)}{\partial \mathbf{x}(t)} & \dots & \frac{\partial z_l(t)}{\partial \mathbf{x}(t)} \end{array} \right]^T \Big|_{\mathbf{x}(t)=\hat{\mathbf{x}}(t)} \quad (6.7)$$

In the case of the simulation conditions, four beacon measurements are used, from beacons L1, L3, L5, and L7, resulting in the  $(12 \times 6)$  matrix

$$H(\hat{\mathbf{x}}(t), t) = \left[ \begin{array}{cccc} \frac{\partial z_1(t)}{\partial \mathbf{x}(t)} & \frac{\partial z_3(t)}{\partial \mathbf{x}(t)} & \frac{\partial z_5(t)}{\partial \mathbf{x}(t)} & \frac{\partial z_7(t)}{\partial \mathbf{x}(t)} \end{array} \right]^T \Big|_{\mathbf{x}(t)=\hat{\mathbf{x}}(t)} \quad (6.8)$$

where

$$z_i = \frac{1}{\sqrt{(X_i - x)^2 + (Y_i - y)^2 + (Z_i - z)^2}} \begin{bmatrix} X_i - x \\ Y_i - y \\ Z_i - z \end{bmatrix} \quad (6.9)$$

resulting in

$$\frac{\partial z_i(t)}{\partial \mathbf{x}(t)} = \frac{1}{A} \begin{bmatrix} a' & b' & c' & 0 & 0 & 0 \\ d' & e' & f' & 0 & 0 & 0 \\ g' & h' & i' & 0 & 0 & 0 \end{bmatrix}$$

$$A = [(X_i - x)^2 + (Y_i - y)^2 + (Z_i - z)^2]^{\frac{1}{2}} \quad i = 1, 3, 5, 7$$

$$a' = -(Y_i - \hat{y})^2 - (Z_i - \hat{z})^2$$

$$b', d' = (X_i - \hat{x})(Y_i - \hat{y})$$

$$c', g' = (X_i - \hat{x})(Z_i - \hat{z})$$

$$e' = -(X_i - \hat{x})^2 - (Z_i - \hat{z})^2$$

$$f', h' = (Y_i - \hat{y})(Z_i - \hat{z})$$

$$i' = -(X_i - \hat{x})^2 - (Y_i - \hat{y})^2$$

## 6.2 Extended Kalman Filter Covariance Matrix Selection

The process and measurement noise covariance matrices,  $\mathbf{Q}$  and  $\mathbf{R}$ , respectively are now defined. These matrices are chosen to represent a reasonable level of expected noise. As such, the measurement noise covariance matrix  $\mathbf{R}$  is defined based on the variance of the presumed level of measurement noise.

$$\mathbf{R}_{nominal} = \left[ 0.0005 \left( \frac{\pi}{180} \right) * 1000 \right]^2 \mathbf{I}^{12} \quad \text{meters} \quad (6.10)$$

Here,  $0.0005(\pi/180)$  represents the expected level of measurement noise, then scaled by 1,000 to convert from kilometers to meters (NASA simulations were constructed such that measurement noise measured in kilometers was added to each axis of each beacon such that it would amount to noise levels of 0.0005 degrees on each beacon axis). The term  $\mathbf{I}^{12}$  represents the identity matrix of size 12. The process noise covariance matrix  $\mathbf{Q}$  is significantly more difficult to quantify mathematically due to the time varying uncertainty of orbital parameter data. All uncertainties, disturbances, and unmodelled dynamics are modelled as lumped process noise. To quantify the variance of the process noise, the state was initially propagated with and without any lumped process noise, resulting in two different dynamic responses,  $\dot{\mathbf{x}}_1$  and  $\dot{\mathbf{x}}_2$ . The dynamics without noise were subtracted from those containing noise to yield the process noise vector

$$\begin{aligned} \mathbf{w}(t) &= \dot{\mathbf{x}}_1 - \dot{\mathbf{x}}_2 \\ &= [\mathbf{f}(\mathbf{x}(t), t) + \mathbf{w}(t)] - [\mathbf{f}(\mathbf{x}(t), t)] \end{aligned} \quad (6.11)$$

The variance of the resulting noise vector is then taken, and the largest variance for a given state is used as a conservative measure to provide a starting point for  $\mathbf{Q}$ .

$$\mathbf{Q}_{nominal} = 0.4825 \times 10^{-10} \mathbf{I}^6 \quad (6.12)$$

The term  $\mathbf{I}^6$  represents an identity matrix of size 6.

### 6.3 Extended Kalman Filter Covariance Matrix Tuning

The simulation is run with the initial values of the noise covariance matrices, which are subsequently tuned to minimize steady-state position estimation error. The process noise covariance matrix  $Q$  is tuned first. Holding  $R_{nominal}$  constant,  $Q_{nominal}$  is tuned by incrementally varying a tuning constant  $\alpha$  from 1 to 1,000,000 (by increments appropriate for size of  $\alpha$ ) until the best combination is found

$$Q_{tune} = \alpha Q_{nominal} \quad (6.13)$$

This combination is found to be  $(2000 * Q_{nominal}, R_{nominal})$ , at  $\alpha = 2000$ . Combinations about this “point” are tested to obtain the best combination of  $Q$  and  $R$ .

$$Q_{tune} = \beta * 2000 * Q_{nominal}$$

$$R_{tune} = \gamma * R_{nominal}$$

- The tuning constant  $\beta$  is varied from 0.85 to 1.15 by increments of 0.05.
- The tuning constant  $\gamma$  is varied from 0.7 to 1.3 by increments of 0.1.
- All possible combinations of  $Q_{nominal}$  and  $R_{nominal}$  contained therein are investigated.

The combination of  $(Q_{nominal}, R_{nominal})$  which yields the lowest steady-state position estimation error yields the values of  $Q$  and  $R$  that best represent the process and measurement noise, respectively, and the Extended Kalman Filter is defined.

## 6.4 Extended Kalman Filter Results

The final choice for  $Q$ ,  $R$  are

$$Q = 0.111 * 10^{-6} * I^6$$

$$R = 0.5331 * 10^{-4} * I^{12} \text{ meters} \quad (6.14)$$

This formulation of the Extended Kalman Filter is implemented into the formation flying simulation in MATLAB/Simulink. The estimator processes four beacon measurements to generate an estimate of the state vector

$$\hat{\mathbf{x}}(t) = \begin{bmatrix} \hat{\mathbf{x}} \\ \hat{\dot{\mathbf{x}}} \end{bmatrix} = \begin{bmatrix} \hat{x} \\ \hat{y} \\ \hat{z} \\ \dot{\hat{x}} \\ \dot{\hat{y}} \\ \dot{\hat{z}} \end{bmatrix} \quad (6.15)$$

The observer is run in-the-loop, supplying the state estimate  $\hat{\mathbf{x}}$  to Luquette's adaptive controller. The performance of the observer is evaluated under the following conditions: Cases One through Four evaluate the observer's efficacy given 1) differences in the observer's initial conditions from actual, 2) input disturbances, 3) parameter uncertainty, and 4) measurement noise. Case Five evaluates the observer under the cumulative influences of Cases One through Four. The values of the uncertainties for each of these cases are given in Chapter 5. Results are given for a simulation runtime of 6000 seconds.

The constraints of the simulation conditions require that the relative position of

the satellites be accurate to within a cubic millimeter in space, meaning

$$((x_d - x)^2 + (y_d - y)^2 + (z_d - z)^2)^{\frac{1}{2}} \leq 1.0 \text{ mm} \quad (6.16)$$

where  $x_d$  represents the desired separation distance, in this case  $[0 \ 0 \ -50,000 \text{ mm}]$ . To determine the efficacy of the controller, a simulation was run (assuming the conditions of Case Five) in which the actual states were given to the controller (i.e. no estimator was used). Given perfect state knowledge, the controller was able to achieve a steady-state relative position error of 0.255 micrometers. This suggests that the criteria for acceptable estimator performance be

$$((x_d - \hat{x})^2 + (y_d - \hat{y})^2 + (z_d - \hat{z})^2)^{\frac{1}{2}} \leq 0.9997 \text{ mm} \quad (6.17)$$

Of course it is preferable that the left-hand side of Eq. (6.17), be not simply within acceptable bounds, but as close to 0 as possible. As a conservative rule of thumb, this research was conducted to satisfy Eq. (6.17) to within 0.5 millimeters.

#### 6.4.1 Case One: Inaccurate Initial Conditions

Here the efficacy of the Extended Kalman Filter given inaccurate initial conditions is investigated. As discussed in Chapter 5, the initial estimated relative position,  $\hat{\mathbf{x}}(0)$ , of the spacecraft at the start of simulation, differs from the actual initial relative position  $\mathbf{x}(0)$

$$\begin{aligned} \mathbf{x}(0) &= [10.4815m, -20.7256m, -44.2785m]^T \\ \hat{\mathbf{x}}(0) &= [11.5927m, -22.7981m, -48.7064m]^T \end{aligned} \quad (6.18)$$

All relative velocities are initialized at rest. Starting at time  $t = 0$ , observer estimates of the satellite relative position and velocity are given to the controller, charged with driving the states to the desired value

$$\mathbf{x}_d(0) = [0, 0, -50m]^T \quad (6.19)$$



In cases One through Four, the magnitude of the relative position error  $|\mathbf{x}_e|$ , is considered, where

$$\mathbf{x}_e = \mathbf{x} - \mathbf{x}_d \quad (6.20)$$

This is the difference between the actual satellite relative position, and the desired value of this quantity.

Case One results are shown in Figure 6-1. This figure shows three different views of the actual relative position error magnitude  $|\mathbf{x}_e|$ . In the top view, the initial value

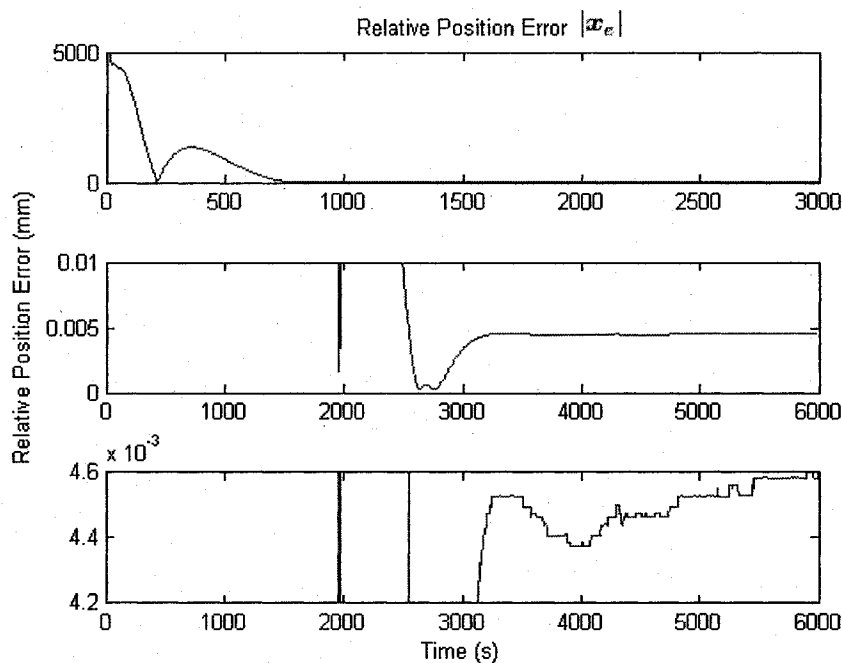


Figure 6-1: Case One - EKF Relative Position Error Magnitude

of the relative position error magnitude, 5,014 mm, corresponds to the difference between the initial estimated and actual states. The middle view demonstrates the steady-state behavior of the satellites. In this case (as with cases Two and Three for the extended Kalman Filter), the term “steady-state” must be used with the

following caveat: there is a drift in the relative positions of the satellites over time, as shown in the third view of Figure 6-1. This drift does not result from differing initial conditions, but rather from the fact that measurement noise and certain causes of process noise (parameter uncertainty and input disturbances) are missing from Case One. Because the Extended Kalman Filter covariance matrices were tuned assuming a certain level of process and measurement noise, these covariance matrices are too large when implemented in simulations that do not include measurement noise and certain process noise (Cases One, Two, and Three). For these cases, the actual process and measurement noise are smaller than expected, so the  $Q$  and  $R$  matrices are oversized. The performance of the Extended Kalman Filter is dependent upon the accuracy of  $Q$  and  $R$  as they are used to calculate the Kalman Gain  $K$ . In these cases the effect of the inaccuracy in the covariance matrices is seen over the course of many hours of simulation run-time, where the drift becomes significant and compromises the efficacy of the observer. For the simulation run-time considered here (6,000 seconds), however, the drift is small ( $\simeq 0.2$  micrometers), so the steady-state behavior is considered to begin at  $t = 3502$  seconds. Figure 6-1 demonstrates that Eq. (6.16) is satisfied at  $t = 748$  seconds, with an RMS error of 4.5 micrometers. Overshoot of magnitude 1361.5 mm occurs at  $t = 362$  seconds.

#### 6.4.2 Case Two: Input Disturbances

The system's reaction to input disturbances is shown in Figure 6-2. Again, the drifting phenomenon is shown in the bottom view of  $|\mathbf{x}_e|$ . This drift will become unmanageable over the course of many hours of simulation run-time. The periodic oscillations seen in the steady-state are a result of input disturbances.

The oscillations, occurring once every 500 seconds, correspond to the motion of the satellite as it oscillates back and forth about  $\mathbf{x}_d$ . The pairings of these oscillations are

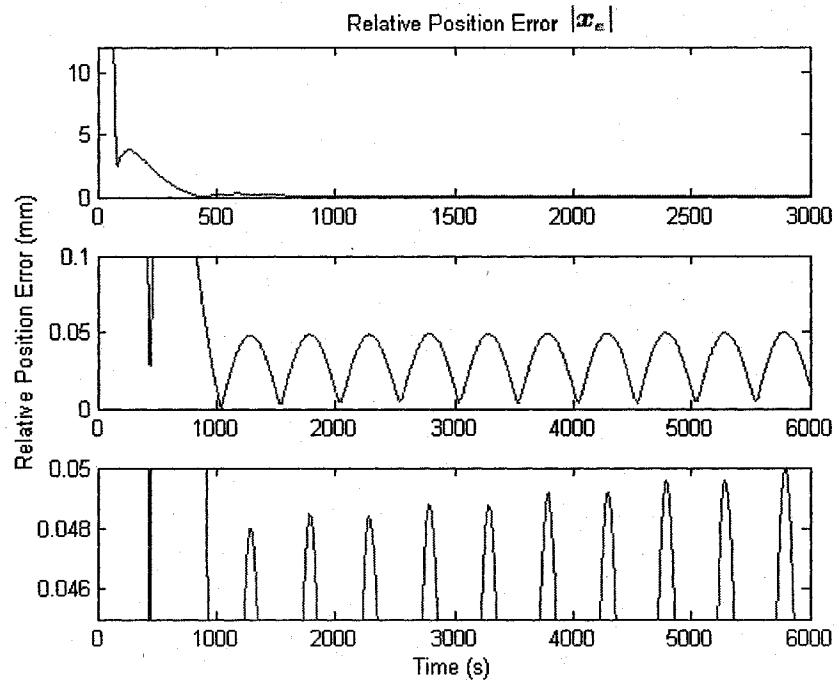


Figure 6-2: Case Two - EKF Relative Position Error Magnitude

best seen in the bottom view, where, beginning at  $t = 1538$  seconds, pairs of peaks of equal magnitude propagate, increasing gradually (the first peak in this picture, does not have a corresponding peak of equal magnitude, as the peak before it (not shown) is still affected by the transient response).

The pairs of peaks begin with a maximum amplitude of approximately 0.0484 mm, and grow by .0004 mm (per pair) to the end of the simulation (i.e. second and third peak have a magnitude of 0.0484 mm, fourth and fifth have a magnitude of 0.488 mm, and so on). Case Two satisfies (6.16) within 319 seconds and begins steady-state behavior at 1040 seconds. Overshoot of 3.8 mm occurs at  $t = 135$  seconds.

#### 6.4.3 Case Three: Parameter Uncertainty

Case Three considers the effect of parameter uncertainties. In this simulation, the orbital parameters representing the distance of the satellites from the Earth and

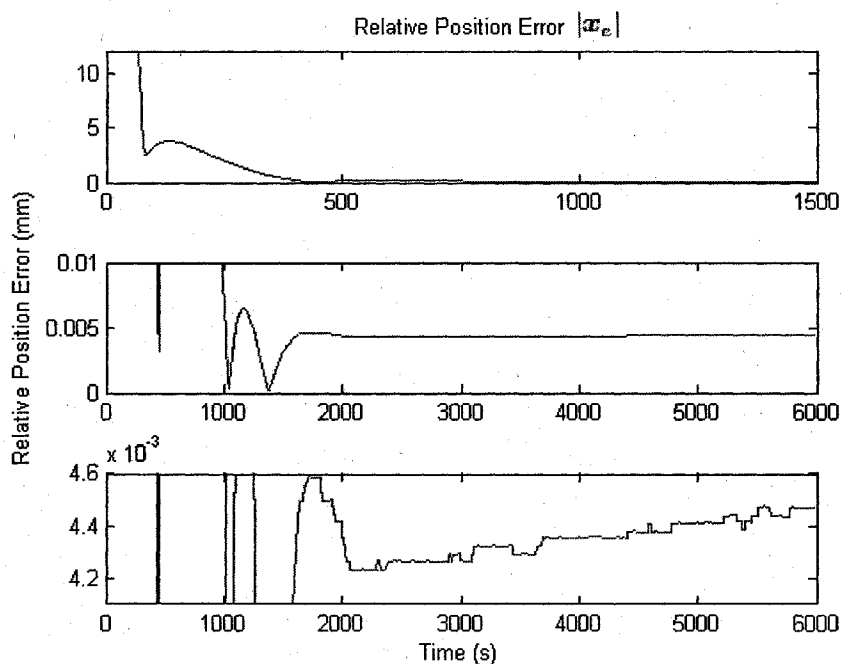


Figure 6-3: Case Three - EKF Relative Position Error Magnitude

the Sun ( $\mathbf{r}_{EF}(t)$ ,  $\mathbf{r}_{EL}(t)$ ,  $\mathbf{r}_{SF}(t)$ , and  $\mathbf{r}_{SL}(t)$ ), are made available once every seven days by implementing a zero-order hold on the update parameters  $\mathbf{r}_{SE}$  and  $\mathbf{r}_{EL}$ . In between updates, the observer estimates the state based on the system model subject to these parametric uncertainties. Furthermore, the values of  $\mathbf{r}_{SE}$  and  $\mathbf{r}_{EL}$  are corrupted with zero-mean noise levels of 5,000,000 m and 4,000 m, respectively. These values were determined by NASA designers as reasonable noise levels for their respective measurements. Figure 6-3 shows the effects of parameter uncertainty on the magnitude of the actual relative position error,  $|\mathbf{x}_e|$ . Eq. (6.16) is satisfied within 319 seconds, after an overshoot of 3.7 mm occurring at 135 seconds. Steady-state behavior begins at  $t = 1815$  seconds, with an RMS error of 0.0044 mm. The drift phenomenon occurs in this figure as well, demonstrated in the third view. The RMS error is small due to the short simulation run-time. With such a short run-time, the percentage difference between the actual values of  $\mathbf{r}_{SE}$  and  $\mathbf{r}_{EL}$ , and the current estimates of  $\mathbf{r}_{SE}$

and  $r_{EL}$  from the previous ground update, is negligible. With simulations lasting longer than seven days, the parameter uncertainties would be greatest just before the update of the orbital parameters, thus the affect on estimation accuracy would be greatest.

#### 6.4.4 Case Four: Measurement Noise

Measurement noise is considered in Case Four. All beacon measurements are subject to zero-mean measurement noise levels of 0.0005 degrees applied to each axis. This value was determined by NASA designers as a reasonable noise level for VISNAV measurements in this application. The results of measurement noise is shown in Figure 6-4. The top view of the figure demonstrates an overshoot of 3.8 mm occurring at  $t = 138$  seconds.

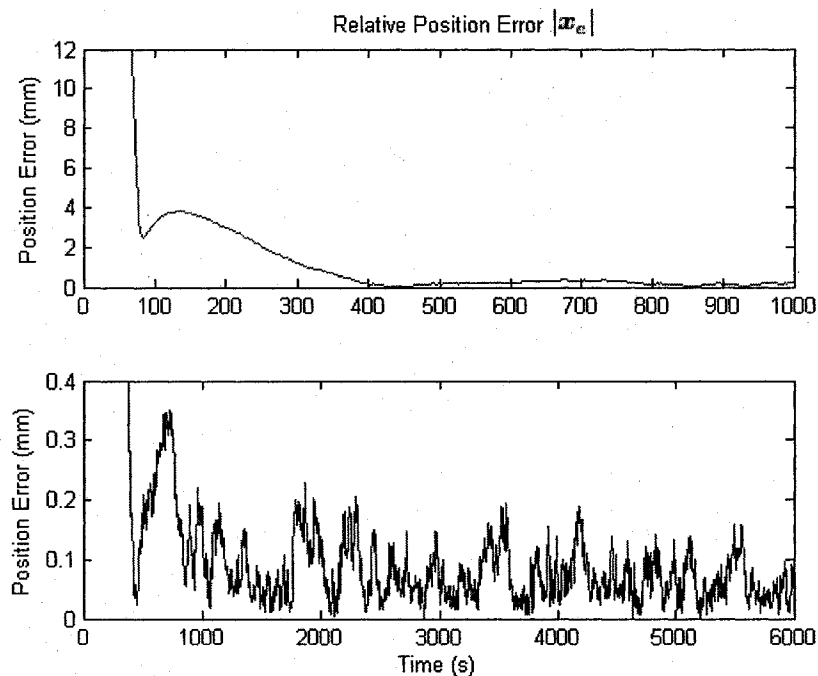


Figure 6-4: Case Four - EKF Relative Position Error Magnitude

The bottom view demonstrates that the drift phenomenon of cases One, Two and Three has been eliminated with the incorporation of measurement noise, with steady-state behavior commencing at  $t = 449$  seconds at an RMS error of 0.0867 mm. Eq. (6.16) is satisfied within 315 seconds.

#### 6.4.5 Case Five: Cumulative Inaccuracies and Disturbances

For Case Five, the effects of Cases One through Four are applied to the system and their cumulative influence on behavior efficacy is considered. Figures 6-5 and 6-6

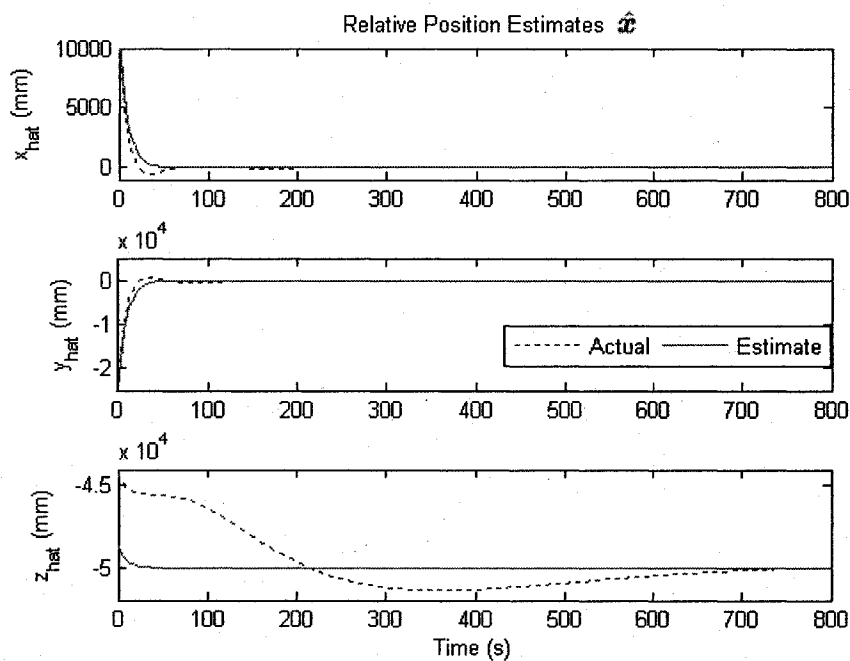


Figure 6-5: Case Five - EKF Relative Position Estimates

show the Actual and Estimated relative position vectors for the Extended Kalman Filter. The observer is quite capable of accurately estimating the relative position of the Follower Satellite with respect to the Leader Satellite for each axis.

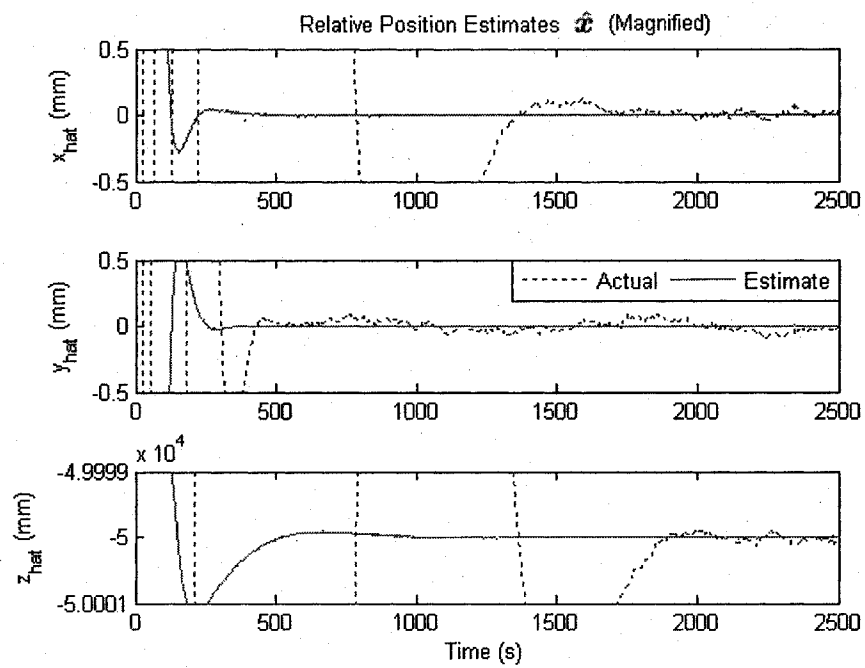


Figure 6-6: Case Five - EKF Relative Position Estimates (Magnified)

Figures 6-7 and 6-8 show  $|\tilde{\mathbf{x}}|$ , where

$$\tilde{\mathbf{x}} = \mathbf{x} - \hat{\mathbf{x}}$$

and demonstrate the ability of the observer to satisfy Eq. (6.17) within  $\approx 924$  seconds.

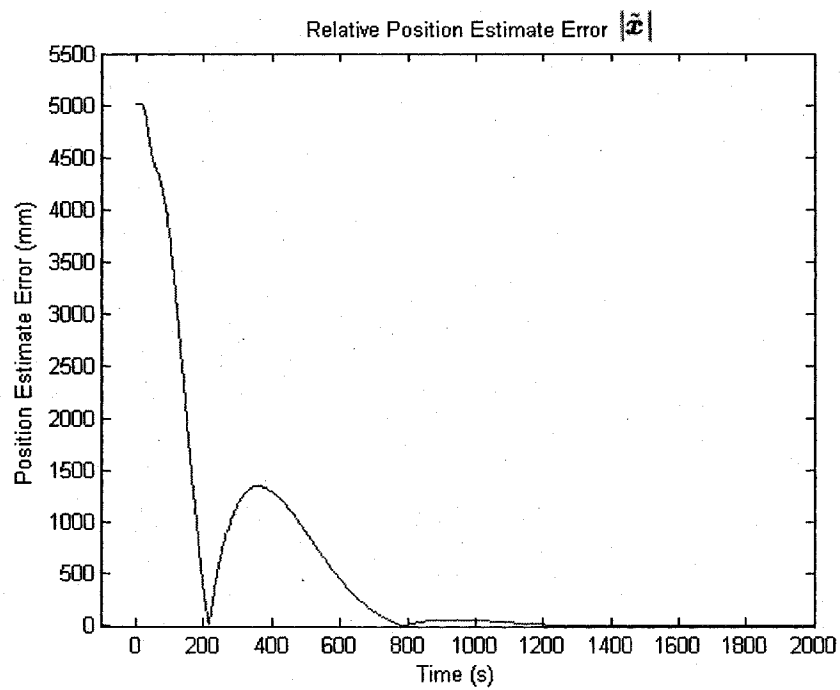


Figure 6-7: Case Five - EKF Relative Position Estimate Error Magnitude

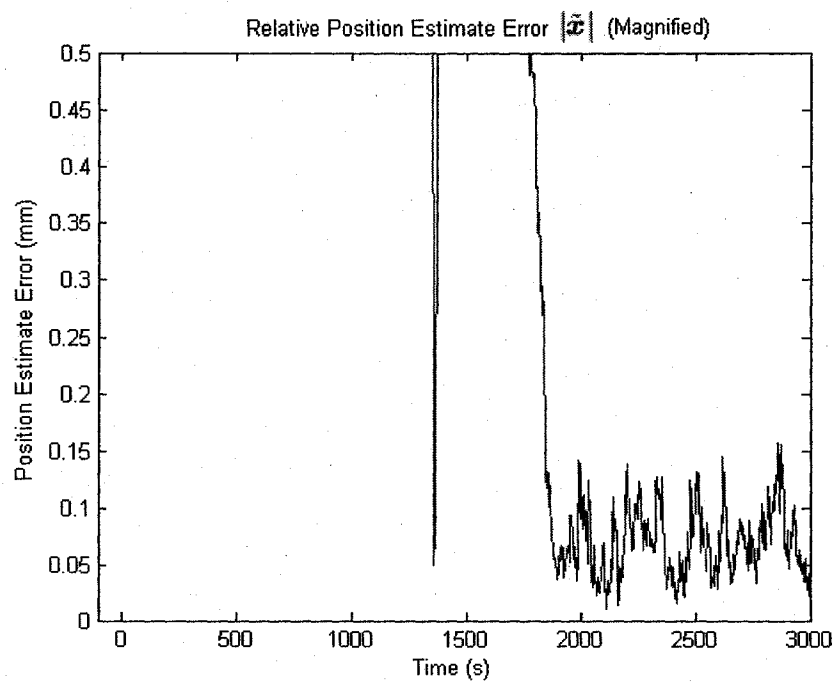


Figure 6-8: Case Five - EKF Relative Position Estimate Error Magnitude(Magnified)



Although this research assumes no formal relative velocity constraints, it is necessary to minimize relative velocity for the sake of minimizing control effort. Figures 6-9 and 6-10 demonstrate the ability of the observer to estimate these quantities.

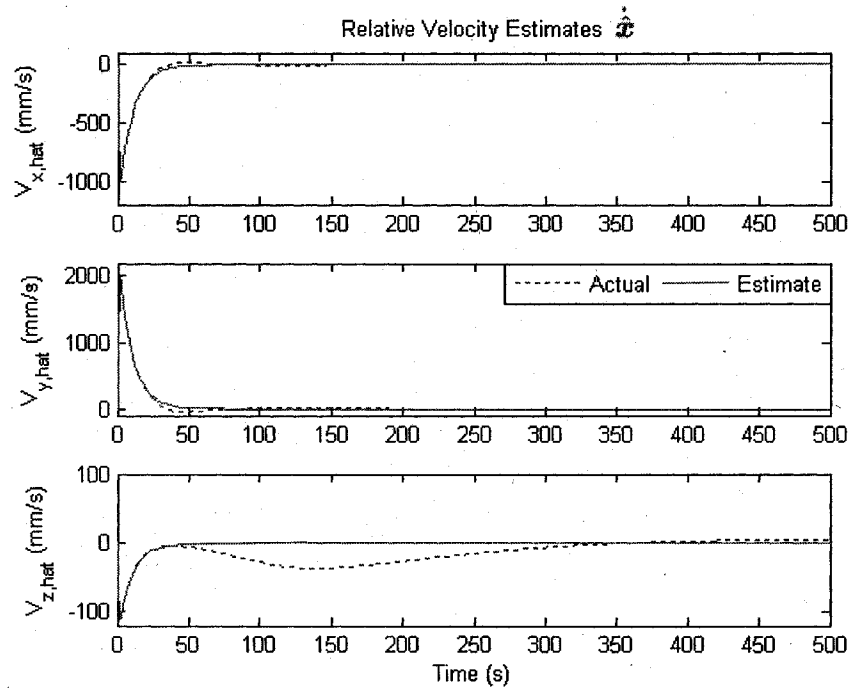


Figure 6-9: Case Five - EKF Relative Velocity Estimates

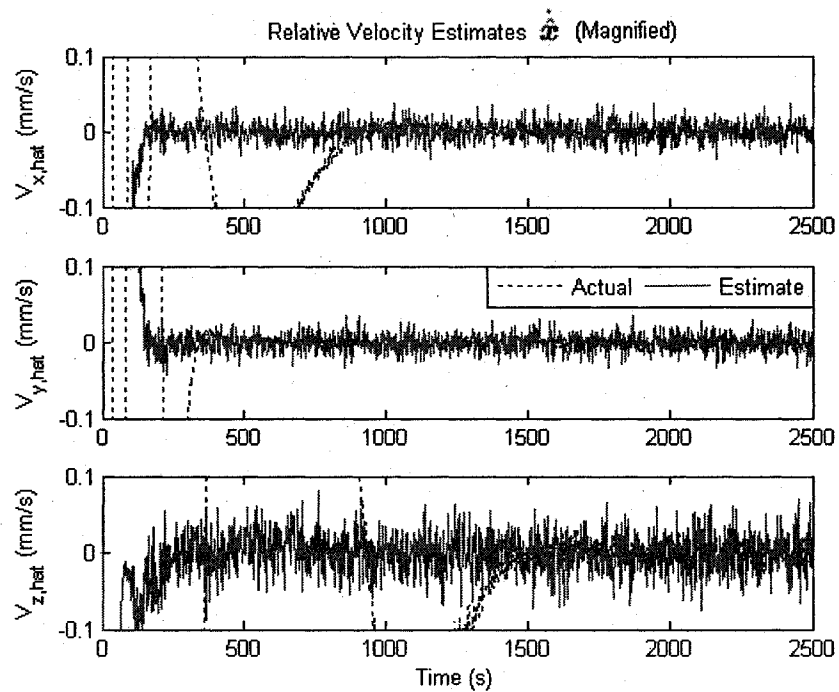


Figure 6-10: Case Five - EKF Relative Velocity Estimates (Magnified)

Figures 6-11 and 6-12 show the magnitude of the relative velocity estimation error, which settles to a steady-state value of 0.0256 millimeters per second. The observer's efficacy in estimating relative position and relative velocity leads to adherence to Eq. (6.17), as shown in the magnitude of the actual relative position error in Figures 6-13 and 6-14. Here it is shown that the actual system satisfies Eq. (6.16) within  $\simeq 1716$  seconds.

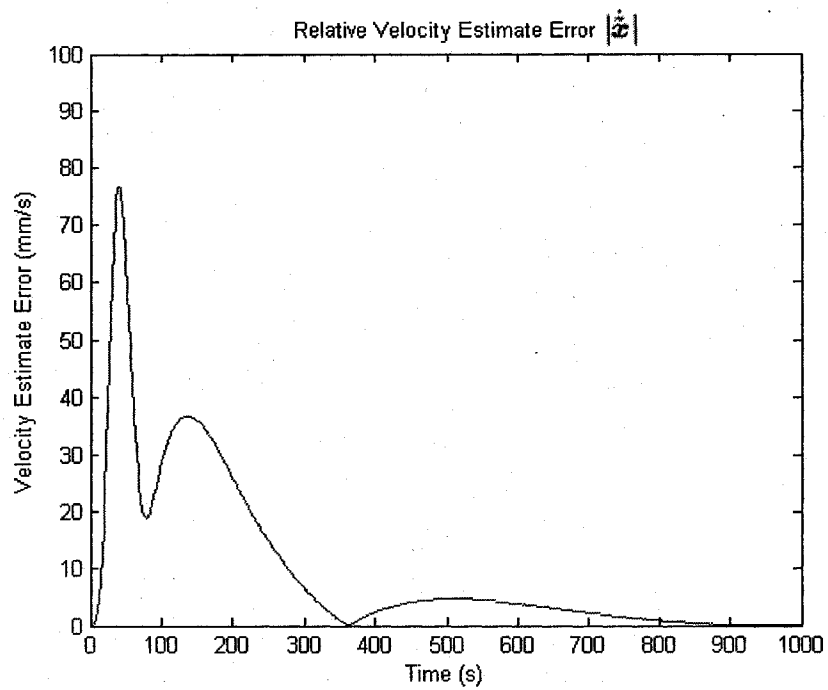


Figure 6-11: Case Five - EKF Relative Velocity Estimate Error Magnitude

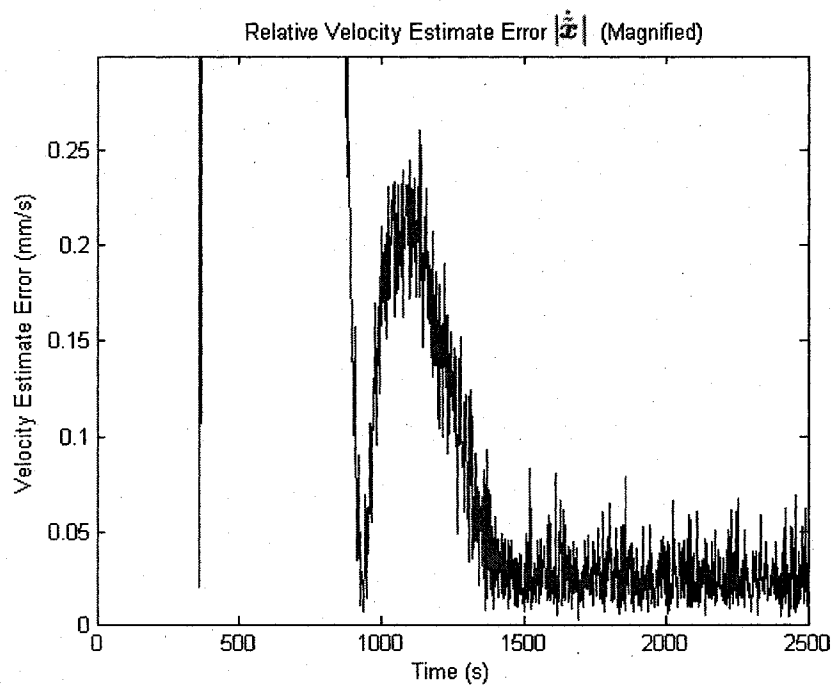


Figure 6-12: Case Five - EKF Velocity Estimate Error Magnitude (Magnified)

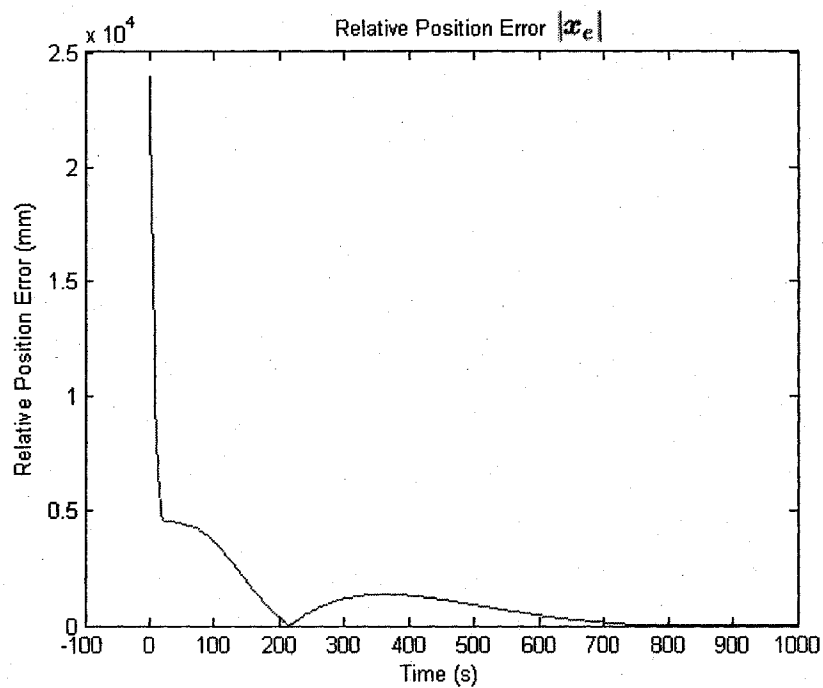


Figure 6-13: Case Five - EKF Relative Position Error Magnitude

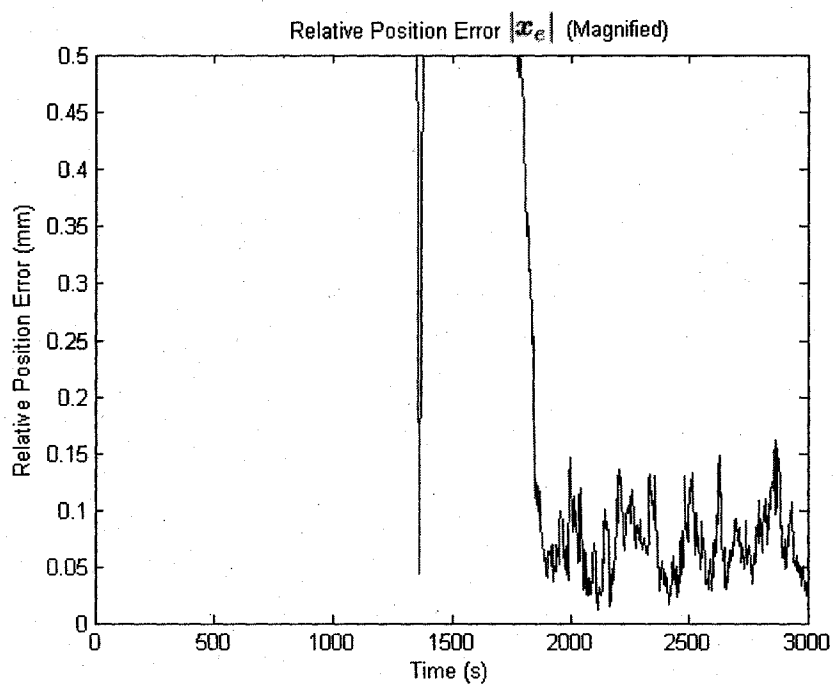


Figure 6-14: Case Five - EKF Relative Position Error Magnitude (Magnified)

# CHAPTER 7

## SLIDING MODE OBSERVER FOR FORMATION FLYING

### 7.1 Sliding Mode Observer Simulations

The Sliding Mode Observer used in simulation is of the form given in Eq. (4.12), with the exception that the function  $sat(\frac{\cdot}{\phi})$  is used in lieu of the  $signum(\cdot)$  function.

$$\begin{bmatrix} \dot{\hat{x}} \\ \ddot{\hat{x}} \end{bmatrix} = \begin{bmatrix} 0 & I \\ A + \Delta A & 0 \end{bmatrix} \begin{bmatrix} \hat{x} \\ \dot{\hat{x}} \end{bmatrix} + \begin{bmatrix} 0 \\ \hat{Y}(\hat{x}, t) \end{bmatrix} - \begin{bmatrix} H_1 \\ H_2 \end{bmatrix} \tilde{z} + K sat\left(\frac{s(\tilde{z})}{\Phi}\right) \quad (7.1)$$

where  $\hat{Y}(\hat{x}, t) = \hat{f}(\hat{x}, t) + u_{thrust}(t) + [\Gamma(t) + \Delta\Gamma(t)] + D(t)$  from Eq. 5.1. Here,  $x$  and  $\dot{x}$  are measured in meters and meters per second, respectively. Each sliding surface is represented by  $s = z - \hat{z}$ . The saturation function is defined as

$$sat\left(\frac{s}{\phi}\right) = \begin{cases} +1 & \text{if } s > \phi \\ s/\phi & \text{if } |s| < \phi \\ -1 & \text{if } s < -\phi \end{cases} \quad (7.2)$$

In this case the saturation function is chosen over the signum function because, as mentioned in Chapter 5, as it eliminates most high amplitude chatter associated with switching in each of the sliding surface functions.

### 7.2 Sliding Mode Observer Gain Selection

For both the Extended Kalman Filter and Sliding Mode Observer simulations, the nonlinear VISNAV measurement model is implemented. The formulation of the

Sliding Mode Observer in Eq. (4.12) assumes a linear measurement model

$$z = Cx$$

With a linear measurement model, the Luenberger Gain  $H \in \mathbb{R}^{6 \times 3m}$  (where  $m$  is the number of measurements, with three axes each) is chosen such that the eigenvalues of  $\Lambda - HC$  are stable, where

$$\Lambda = \begin{bmatrix} 0 & I \\ A & 0 \end{bmatrix}$$

Because these simulations implement a nonlinear measurement model, the desired eigenvalues of  $\Lambda$  cannot be easily chosen. As such,  $H$  is arbitrarily chosen as in [26]. From this basis, gains are further tuned to minimize the steady-state error of the position between the MSC and DSC. Initially, for each beacon (L1, L3, L5, or L7)

$$\begin{aligned} H_i &= \begin{bmatrix} H_1 \\ H_2 \end{bmatrix} \\ H_1 &= - \begin{bmatrix} 5 & 0 & 0 \\ 0 & 10 & 0 \\ 0 & 0 & 25 \end{bmatrix} \\ H_2 &= 0.01H_1 \\ i &= L1, L3, L5, L7. \end{aligned}$$

Because there are four beacons and three axes for each beacon measurement, there may be up to twelve measurements, resulting in  $H \in \mathbb{R}^{6 \times 12}$ . For this same reason there can be up to twelve sliding surface functions. The Switching Gain Matrix is  $K \in \mathbb{R}^{6 \times r}$ . This matrix is chosen according to uncertainty bounds, following the criteria

$$K_i > \xi + D_o$$

For twelve measurements, the resulting  $K$  matrix is initially chosen to be an aug-

mented matrix of four sub-column matrices such that

$$\mathbf{K}_i = \begin{bmatrix} \mathbf{K}_1 \\ \mathbf{K}_2 \end{bmatrix} = \begin{bmatrix} 1 \times 10^{-5} \mathbf{I}^3 \\ 1 \times 10^{-7} \mathbf{I}^3 \end{bmatrix}$$

This research uses a single sliding surface, chosen to be the summation of the measurement errors for each of the 12 beacon axes

$$s(\tilde{\mathbf{z}}) = s(\mathbf{z}_i - \hat{\mathbf{z}}_i) = \sum (\mathbf{z} - \hat{\mathbf{z}}), \quad i = L1_x, L1_y, L1_z, L3_x, \dots, L7_z$$

As a result, the  $\mathbf{K}$  matrix used in the observer takes the following form

$$\mathbf{K} = \begin{bmatrix} 1 \times 10^{-5} \\ 1 \times 10^{-5} \\ 1 \times 10^{-5} \\ 1 \times 10^{-7} \\ 1 \times 10^{-7} \\ 1 \times 10^{-7} \end{bmatrix} \quad (7.3)$$

Initially, the boundary layer for the sliding surface function is arbitrarily chosen to be 5 mm. This value, as well as the values for  $\mathbf{H}$ ,  $\mathbf{K}$ , and  $s(\tilde{\mathbf{z}})$  were chosen from [26].

### 7.3 Sliding Mode Observer Gain Tuning

When the sliding surface and nominal values are defined, the Luenberger Gain Matrix,  $\mathbf{H}$ , Switching Gain Matrix,  $\mathbf{K}$ , and boundary layer  $\phi$  (now a scalar as there is only one sliding surface), are tuned to minimize position estimation error. For each combination of these three values, a simulation is run, and the magnitude of the resulting position estimation error is evaluated. This criteria is chosen to evaluate observer performance because the MSC and DSC satellites must maintain strict relative position in order to ensure proper focus of the X-Ray telescope.

The Luenberger Gain Matrix, which determines whether the error trajectories are driven toward the sliding surface, is tuned first in the following manner

$$\mathbf{H}_{i,tune} = \alpha \begin{bmatrix} \beta \mathbf{H}_1 \\ \gamma \mathbf{H}_2 \end{bmatrix} \quad (7.4)$$

The tuning constants  $\alpha$ ,  $\beta$ , and  $\gamma$  are adjusted to propagate new versions of the Luenberger gain matrix. The ranges for these values were selected assuming the best choice for  $\mathbf{H}$  was somewhere reasonably close to the nominal value (not more than twice as large and not less than one-tenth as large). In the tuning method employed, the tuning constants are distributed to all  $\mathbf{H}_i$  for  $i = L1, L3, L5, L7$ , making all  $\mathbf{H}_i$  identical. Also, the relative proportion of the numerical terms on the diagonal of  $\mathbf{H}_1$  remain unchanged throughout the tuning process. The off-diagonal terms in the  $\mathbf{H}_1$  and  $\mathbf{H}_2$  matrices are kept at zero as well. Although it is not necessary to maintain any of these constraints in the tuning process, these constraints were adopted in the tuning method to avoid the dramatic increase in the number of possible gain sets as the number of tuning constants increases. Simulations are run for various values of the tuning constants, then evaluated for steady state position estimation error. The constants  $\alpha$ ,  $\beta$ , and  $\gamma$  are varied as follows

- $(\alpha, \beta, \gamma) = (\alpha, 1, 1)$ : Here the constant  $\alpha$  is varied from 0.1 to 2 in increments of 0.1, holding  $\beta$  and  $\gamma$  constant.
- $(\alpha, \beta, \gamma) = (1, \beta, 1)$ : Here the constant  $\beta$  is varied from 0.1 to 2 in increments of 0.1, holding  $\alpha$  and  $\gamma$  constant.
- $(\alpha, \beta, \gamma) = (1, 1, \gamma)$ : Here the constant  $\gamma$  is varied from 0.1 to 2 in increments of 0.1, holding  $\alpha$  and  $\beta$  constant.
- $(\alpha, \beta, \gamma) = (1, \beta, \gamma)$ : Here the constants  $\beta$  and  $\gamma$  take on values from 0.1 to 1.9, by increments of 0.1, and are changed in the opposite direction of the other



tuning constant. All combinations of tuning constants fit the form:

$$(\alpha, \beta, \gamma) = (1, 1 - 0.1n, 1 + 0.1n)$$

where  $n$  represents the number of increments. Example values are (1, 0.8, 1.2) and (1, 1.2, 0.8)

Once the best choice of  $\mathbf{H}$  is determined, the Switching Gain Matrix  $\mathbf{K}$  is tuned in similar fashion

$$\mathbf{K}_{tune} = \alpha \begin{bmatrix} \beta \times 10^{-5} \\ \beta \times 10^{-5} \\ \beta \times 10^{-5} \\ \gamma \times 10^{-7} \\ \gamma \times 10^{-7} \\ \gamma \times 10^{-7} \end{bmatrix} \quad (7.5)$$

Finally, once the best choices of  $\mathbf{H}$  and  $\mathbf{K}$  are determined, the boundary layer  $\phi$  is tuned as follows

$$\phi_{tune} = \alpha\phi \quad (7.6)$$

Since there is only one sliding surface, and therefore one boundary layer, the search for the best boundary layer is more straightforward than for the  $\mathbf{H}$  and  $\mathbf{K}$  matrices. Here,  $\alpha$  is varied from 0.1 to 2.0 in increments of 0.1. Upon finding the best choice for  $\phi$ , the Sliding Mode Observer is defined.

The following trends were observed in gain tuning. The choice of the linear gain Matrix  $\mathbf{H}$  has bearing over the transient response. In tuning  $\mathbf{H}$  for the simulation conditions, it is observed that smaller values of  $\mathbf{H}$  result in slower transient responses, and vice versa.

The choice of the switching gain matrix  $\mathbf{K}$  and boundary layer  $\phi$  have little bearing over the transient response, but rather affect the quality of estimation results in the steady state. The Luenberger gain matrix  $\mathbf{H}$  determines whether the error trajectories

will approach the sliding surface, while  $\mathbf{K}$  and  $\phi$  determine whether they will remain on the sliding surface. In selecting  $\mathbf{K}$ , it is necessary to choose values large enough to account for modelling uncertainties and disturbances. Choosing  $\mathbf{K}$  to be larger than necessary will decrease the quality of the estimate, as the saturation function will have to switch at a higher rate. The boundary layer must be chosen large enough such that estimation error remains within the boundary layer, and not so small as to mimic a signum function (induce high chattering). Overly large boundary layer values will result in poor estimates, as large values make the observer more tolerant of the condition  $s(\tilde{\mathbf{z}}) = 0$  not being met.

## 7.4 Sliding Mode Observer Results

The final choice for  $H$ ,  $K$ , and  $\phi$  are

$$H = \begin{bmatrix} H_1 & H_2 & H_3 & H_4 \end{bmatrix}$$

$$H_i = \begin{bmatrix} -5.5 & 0 & 0 \\ 0 & -11.0 & 0 \\ 0 & 0 & -27.5 \\ -0.05 & 0 & 0 \\ 0 & -0.1 & 0 \\ 0 & 0 & -0.25 \end{bmatrix}, \quad i = 1, 2, 3, 4$$

$$K = 1 * 10^{-5} \begin{bmatrix} 0.8 \\ 0.8 \\ 0.8 \\ 0.008 \\ 0.008 \\ 0.008 \end{bmatrix}$$

$$\phi = 6 \text{ mm}$$

This formulation of the Sliding Mode Observer is implemented into the simulation in MATLAB/Simulink, in the same fashion as the Extended Kalman Filter. The performance of the observer is evaluated considering the same five cases as the Extended Kalman Filter in Chapter 6.

### 7.4.1 Case One: Inaccurate Initial Conditions

Case One demonstrates the effect of inaccurate initial conditions on the actual relative position error magnitude,  $|\mathbf{x}_e|$ . Figure 7-1 demonstrates an overshoot of 893.4 mm occurring at  $t = 164$  and the satisfaction of eq (6.16) after 748 seconds. No drift phenomenon occurs with the Sliding Mode Observer for zero measurement noise. Steady-state behavior begins at  $t = 1544$  with an RMS error of 0.0014 mm.

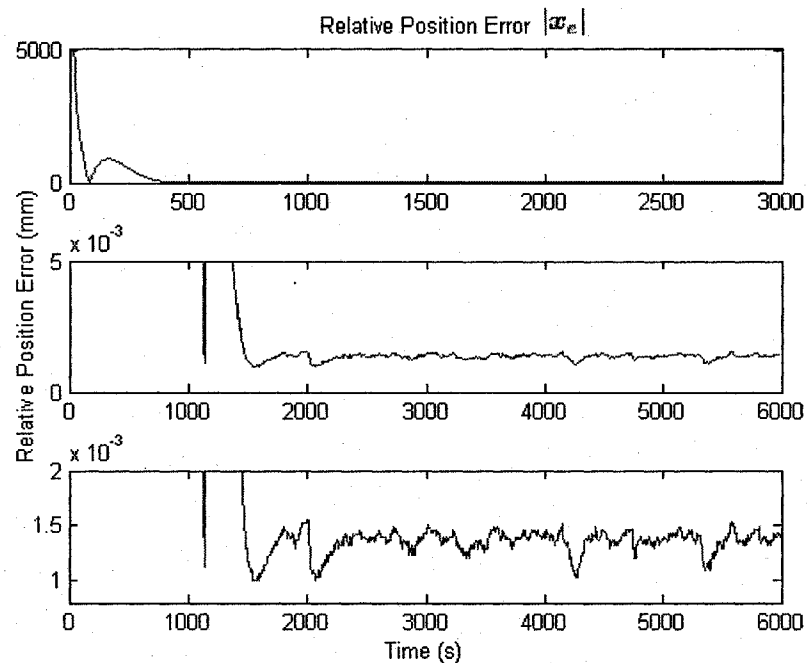


Figure 7-1: Case One - SMO Relative Position Error Magnitude

### 7.4.2 Case Two: Input Disturbances

The effect of input disturbances on  $|\mathbf{x}_e|$  is considered here. Figure 7-2 demonstrates a decreased overshoot of 6.7 mm, given the removal of inaccurate initial conditions, occurring at  $t = 231$ . Eq. (6.16) is satisfied after 418 seconds, with steady

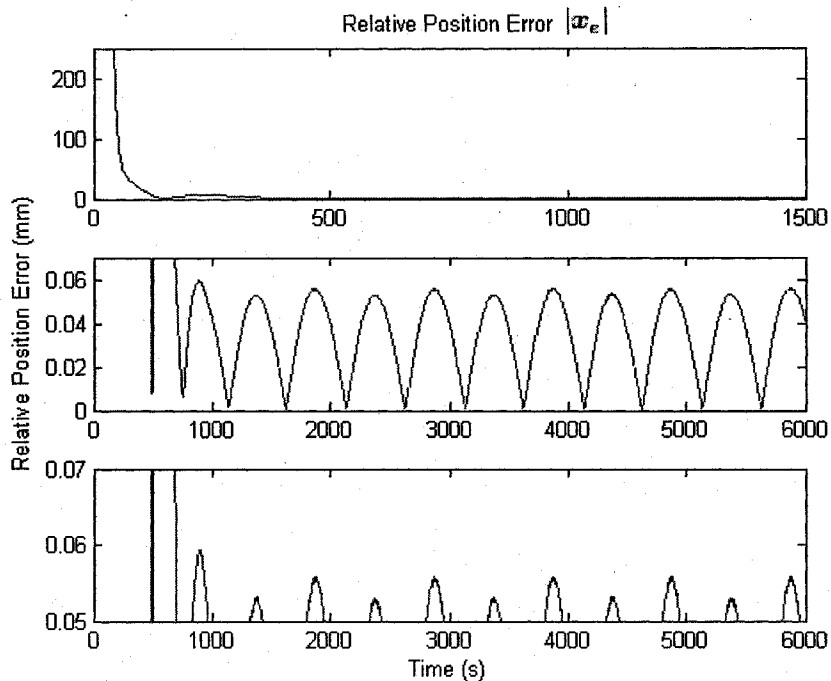


Figure 7-2: Case Two - SMO Relative Position Error Magnitude

state behavior beginning at  $t = 1135$  seconds. As with Case Two for the Extended Kalman Filter, the pairing associated with oscillations about  $\mathbf{x}_d$  occurs here, beginning at  $t = 1135$ . Here, the first peaks of each pair have a value of 0.053 mm, and the second peaks have a value of 0.56 mm, and the magnitude of the pairs of peaks does not grow over time. This indicates that the overshoot past  $\mathbf{x}_d$  is greater on one side of the oscillation than the other.

#### 7.4.3 Case Three: Parameter Uncertainty

Figure 7-3 shows the effect of uncertainties in orbital parameters on  $\mathbf{x}_e$ . Overshoot of magnitude 6.7 mm occurs at  $t = 232$ , and eq (6.16) is eventually satisfied after 420 seconds. Steady-state behavior begins at  $t = 1815$  with an RMS error of 0.0014 mm. The RMS error is small, as with the Extended Kalman Filter, due to the short simulation run-time. With such a short run-time, the percentage differences between

the actual values of  $r_{SE}$  and  $r_{EL}$ , and the current estimates of these parameter from the previous ground update, is negligible.

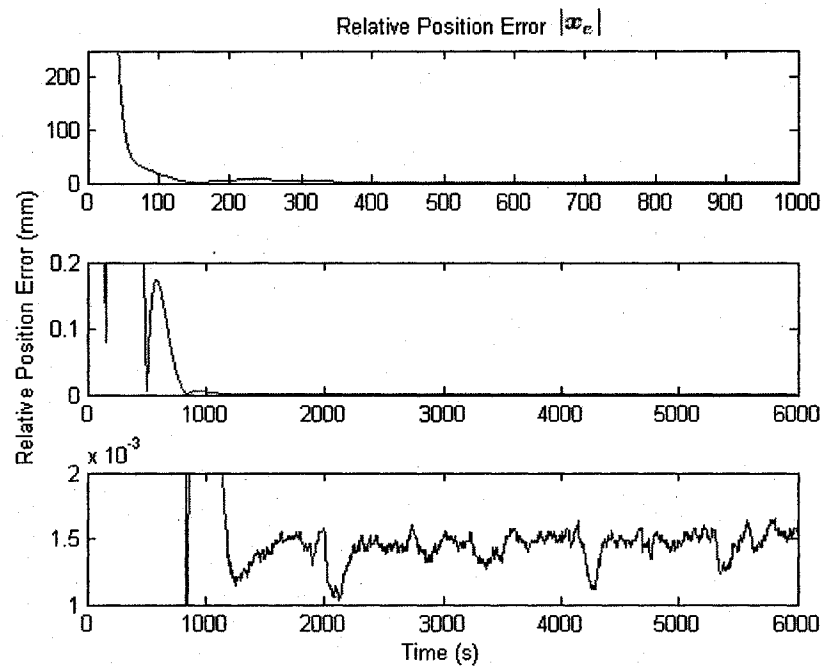


Figure 7-3: Case Three - SMO Relative Position Error Magnitude

#### 7.4.4 Case Four: Measurement Noise

The effect of measurement noise on  $\boldsymbol{x}_e$  is demonstrated in Figure 7-4. Here it is shown that eq (6.16) is satisfied within 418 seconds, following a 6.4 mm overshoot at  $t = 225$ . Steady-state behavior begins at  $t = 514$  at an RMS error value of 0.1374 mm. This error value is a significant increase over Cases One, Two, and Three.

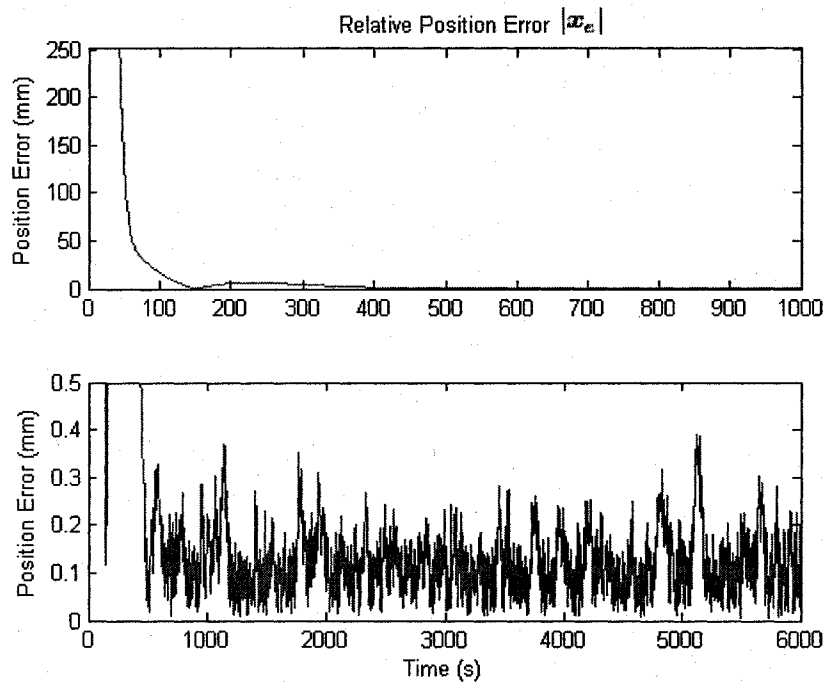


Figure 7-4: Case Four - SMO Relative Position Error Magnitude

### 7.4.5 Case Five: Cumulative Inaccuracies and Disturbances

Case Five investigates the influence of all inaccuracies and disturbances on  $\mathbf{x}_e$ . Figures 7-5 and 7-6 show the actual and estimated relative position vectors for the Sliding Mode Observer.

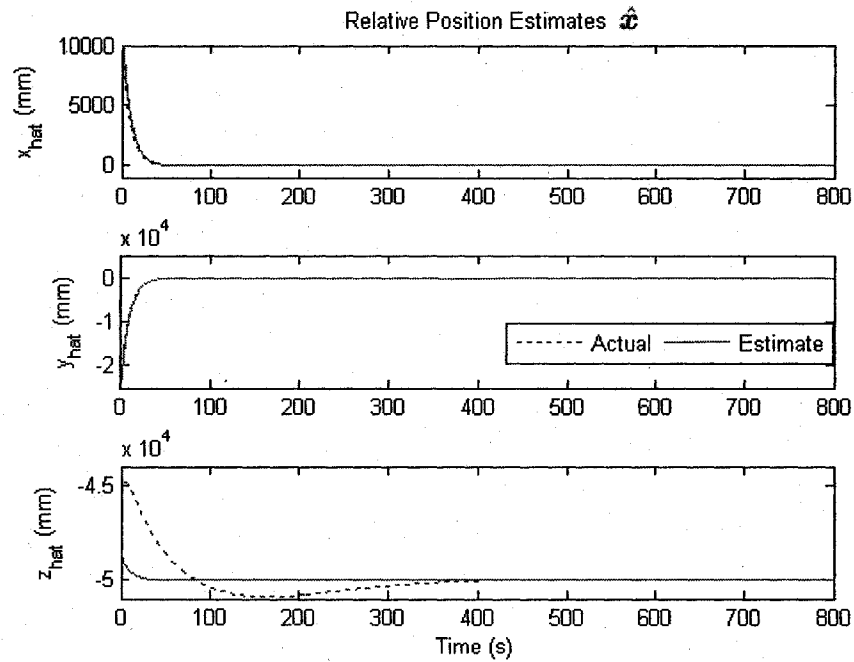


Figure 7-5: Case Five - SMO Relative Position Estimates



Although the state estimates for the Sliding Mode Observer appear somewhat comparable to those of the Extended Kalman Filter, the response is far more oscillatory. This is because of the switching function (saturation function) associated with the Switching Gain Matrix  $K$  and boundary layer  $\phi$ .

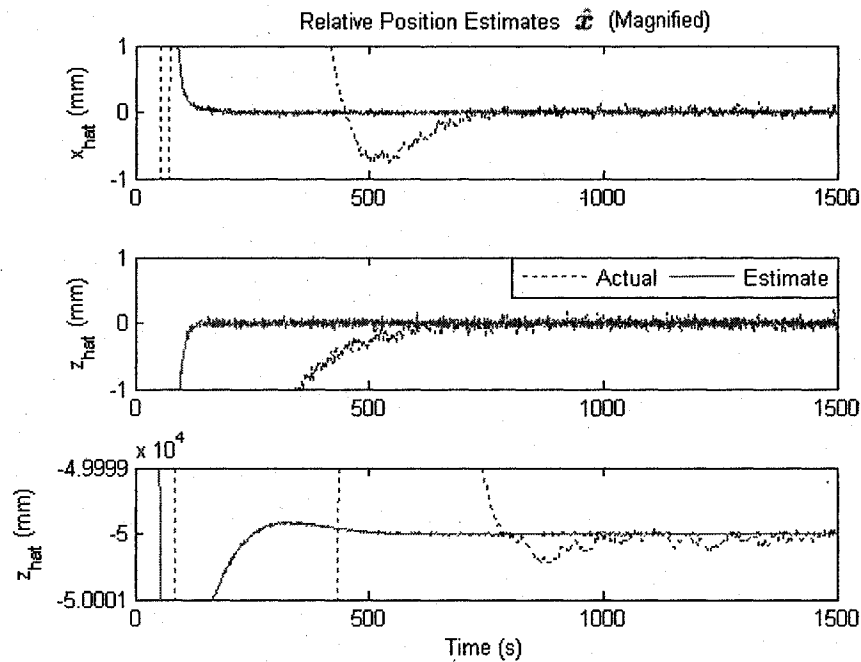


Figure 7-6: Case Five - SMO Relative Position Estimates (Magnified)

Figures 7-7 and 7-8 show the magnitude of the relative position estimate error and demonstrate the observer's competency in satisfying equation Eq. (6.17). The RMS error for relative position estimation is 0.1322 mm, well within acceptable bounds. The Sliding Mode Observer satisfies Eq. (6.17) within  $\approx 811$  seconds.

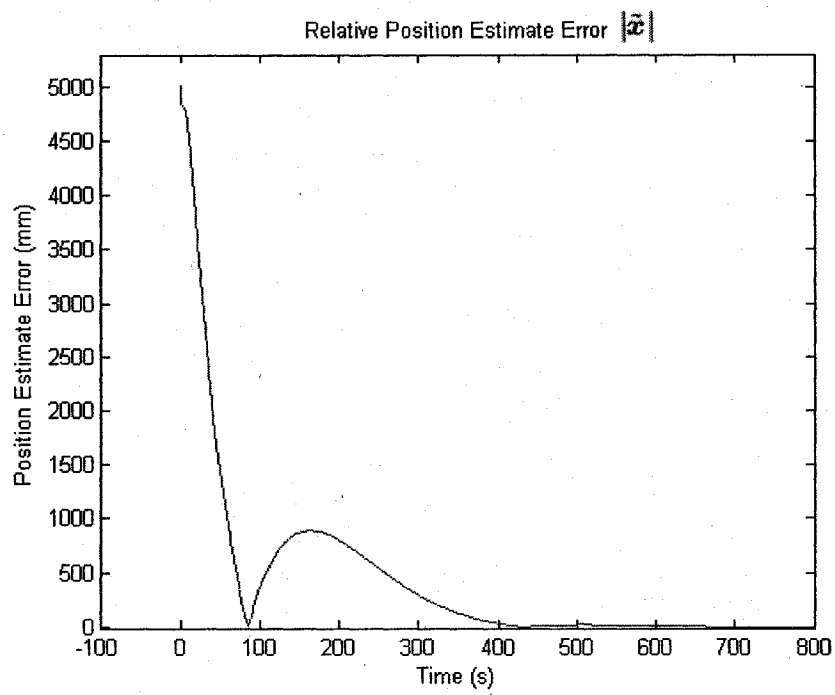


Figure 7-7: Case Five - SMO Relative Position Estimate Error Magnitude

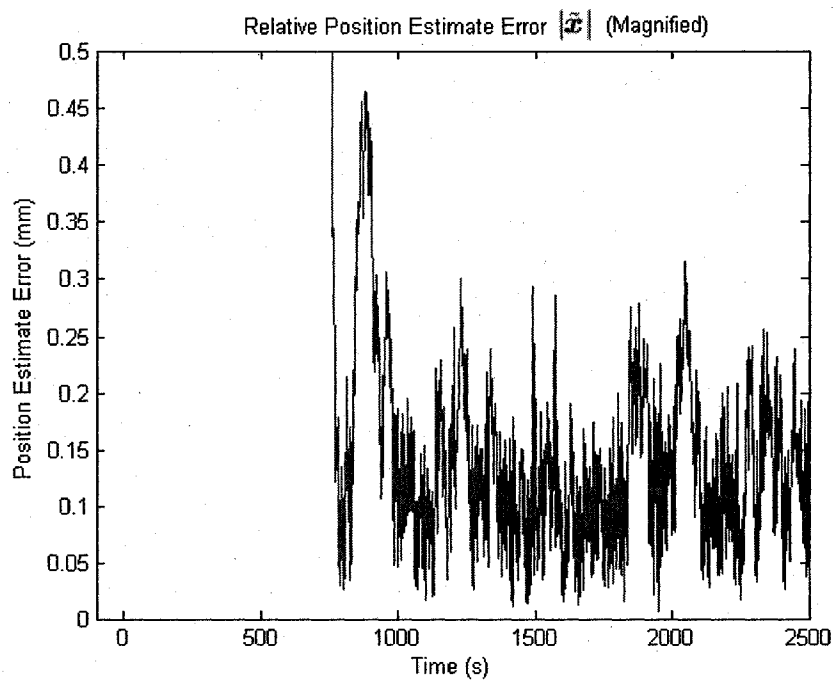


Figure 7-8: Case Five - SMO Relative Position Estimate Error Magnitude (Magnified)

Figures 7-9 and 7-10 show the relative velocity estimates are highly oscillatory, so oscillatory in fact that the standard deviation of the relative velocity estimate at steady state is 59% of the mean, as shown in the magnitude of the relative velocity estimate error, Figures 7-11 and 7-12. This issue can be addressed by using an integral term in the sliding surface to reduce the steady-state error. This does, however, result in slower convergence time[3].

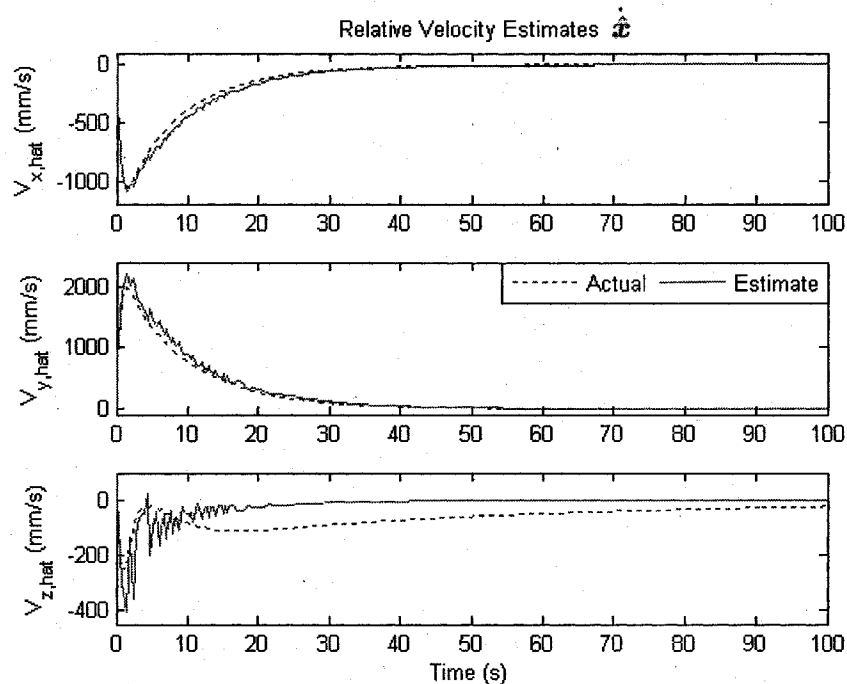


Figure 7-9: Case Five - SMO Relative Velocity Estimates

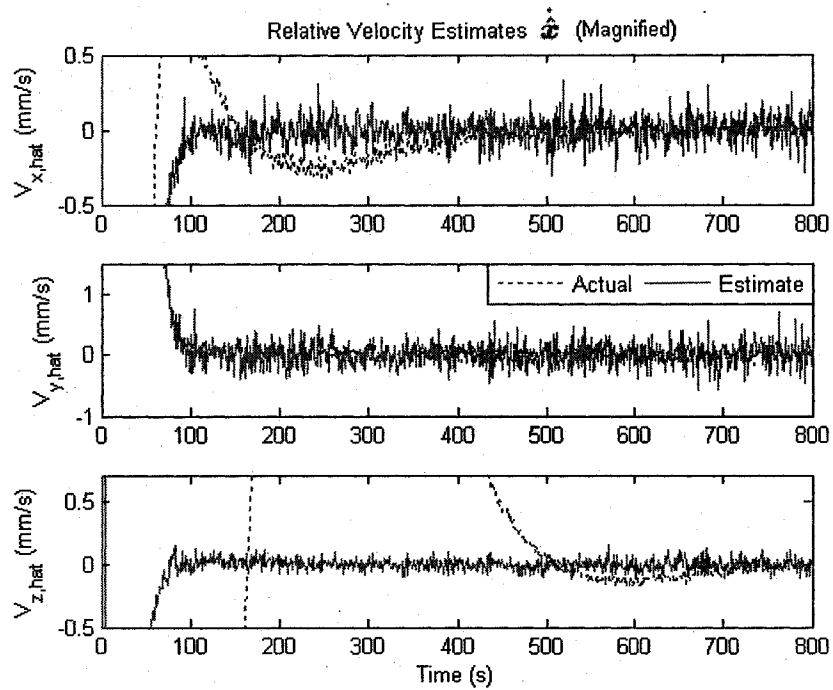


Figure 7-10: Case Five - SMO Relative Velocity Estimates (Magnified)

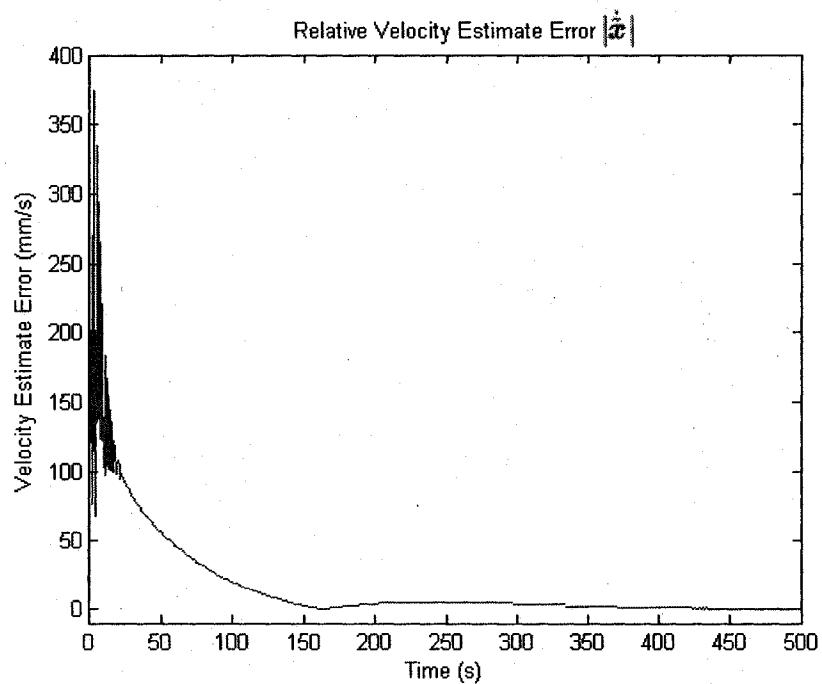


Figure 7-11: Case Five - SMO Relative Velocity Estimate Error Magnitude

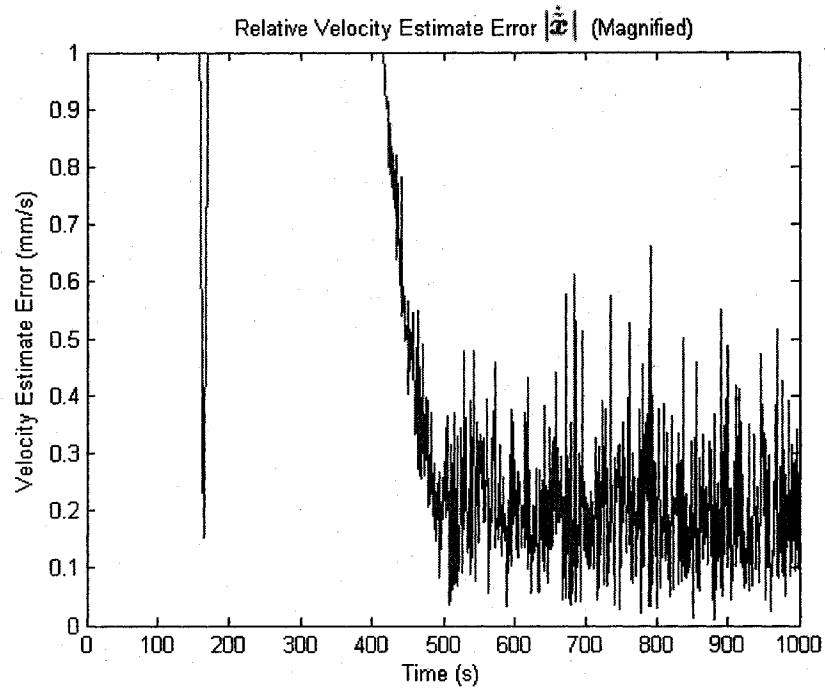


Figure 7-12: Case Five - SMO Relative Velocity Estimate Error Magnitude (Magnified)

For the Sliding Mode Observer, as with the Extended Kalman Filter, the quality of relative position error is comparable to that of the relative position estimate error. Figures 7-13 and 7-14 show the magnitude of the actual relative position error, and demonstrate that Eq. (6.16) is satisfied permanently within 742 seconds.

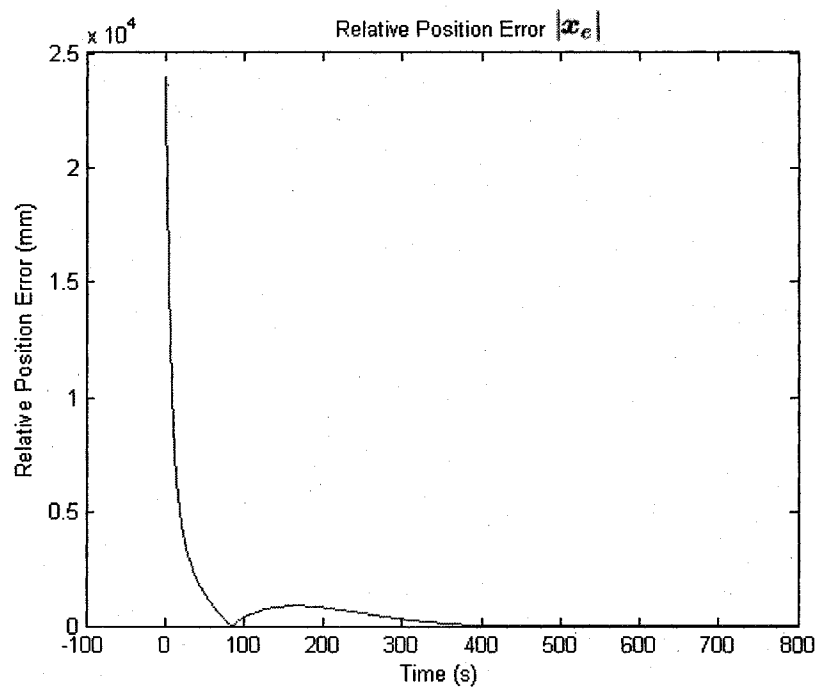


Figure 7-13: Case Five - SMO Relative Position Error Magnitude

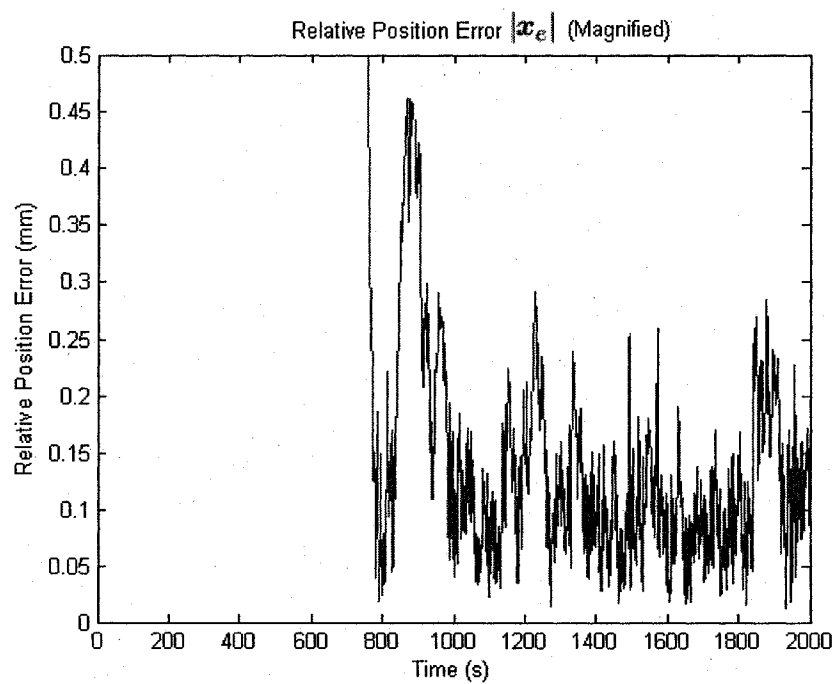


Figure 7-14: Case Five - SMO Relative Position Error Magnitude (Magnified)

## CHAPTER 8

### COMPARISON OF EKF AND SMO

#### 8.1 Case Results

Chapters 6 and 7 demonstrated the Extended Kalman Filter and Sliding Mode Observer ability to provide state estimates in the Constellation X model using a nonlinear measurement model, given inaccurate initial conditions, and nominal measurement noise, parameter uncertainties, and input disturbances.

The observers were implemented in simulations subject to five different conditions, reviewed here

- Case One: Inaccurate initial conditions are considered individually.
- Case Two: Input disturbances are considered individually.
- Case Three: Parameter uncertainties are considered individually.
- Case Four: Measurement noise is considered individually.
- Case Five: Inaccuracies, noise and disturbances are considered collectively.

The system behavior displayed in Cases One through Four are now analyzed to determine their contributions to Case Five. Figures 8-1 through 8-12 summarize the results of the individual cases. All cases are reviewed for relevant characteristics of the actual relative position error vector magnitude  $|x_e|$ . These characteristics include: the time it takes to satisfy eq (6.16),  $t_{satisfy}$ , the magnitude of the overshoot and the

time at which it occurs,  $t_{overshoot}$ , the time at which steady-state behavior occurs, and the associated mean, standard deviation, and RMS value associated with the steady-state behavior. Results for Case Two, shown in Figure 8-3, did not include these last three values due to the cyclical nature of the steady-state behavior.

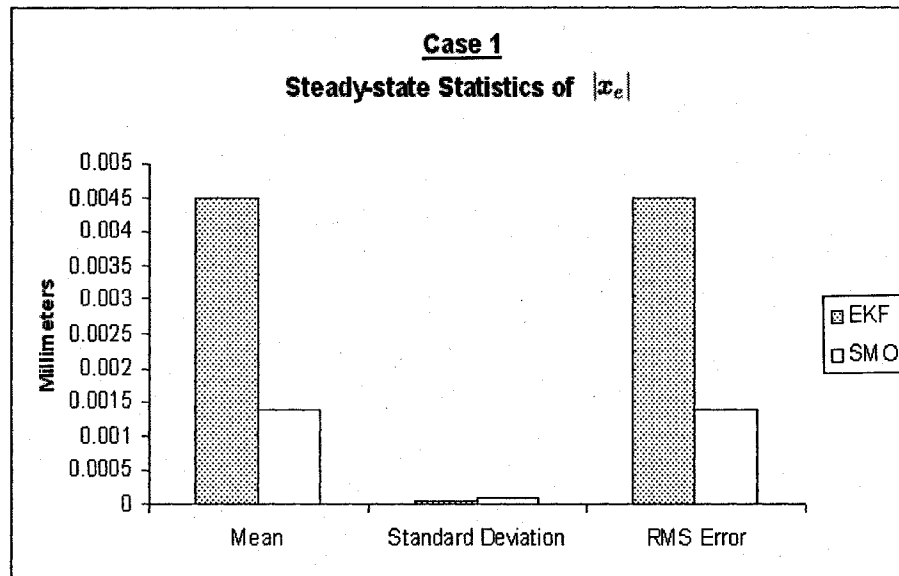
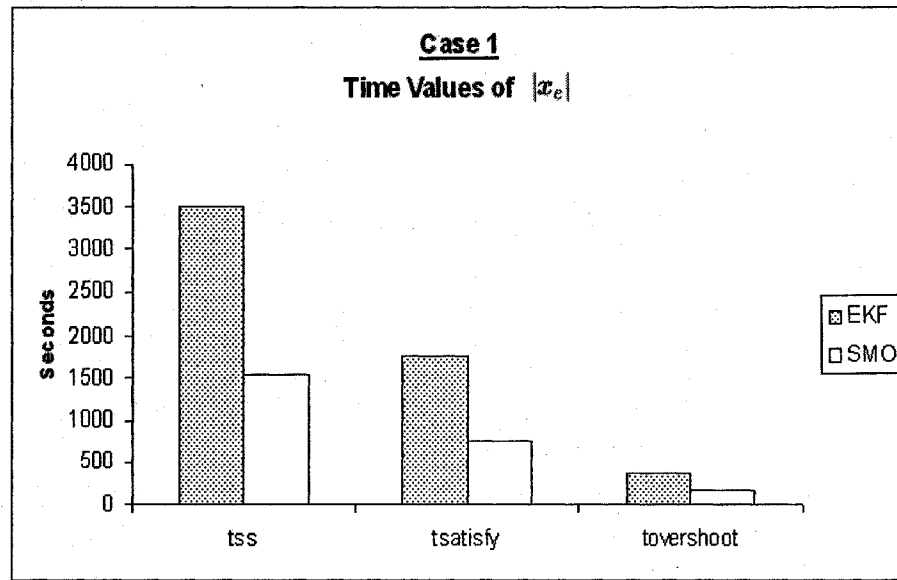
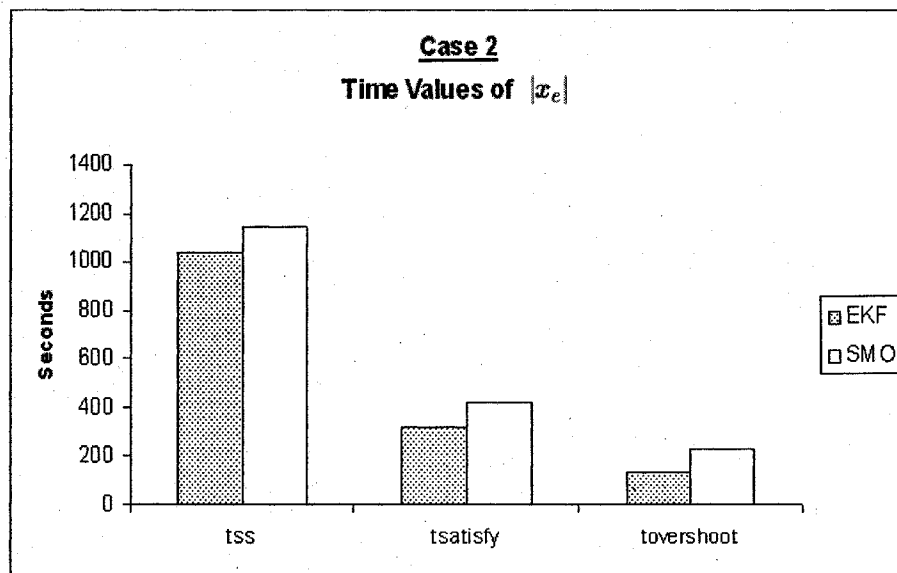
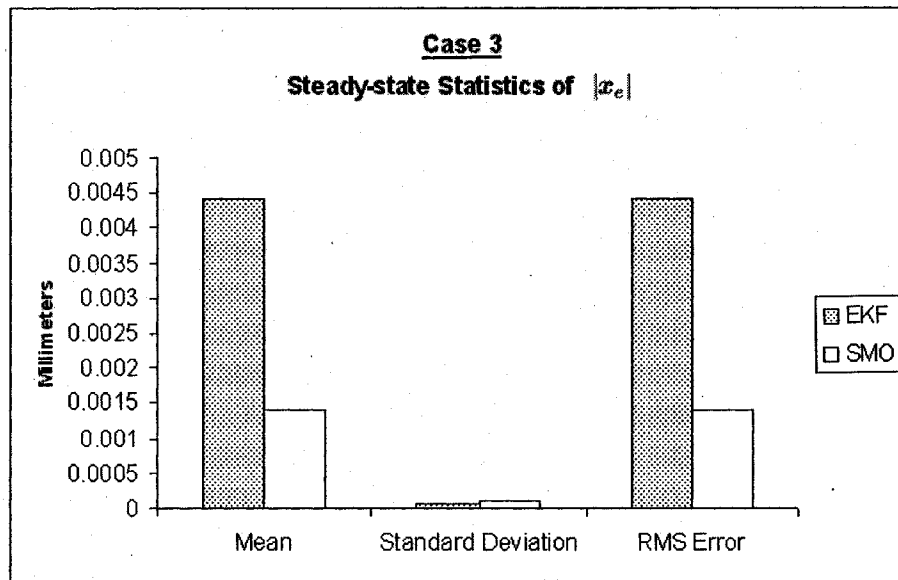
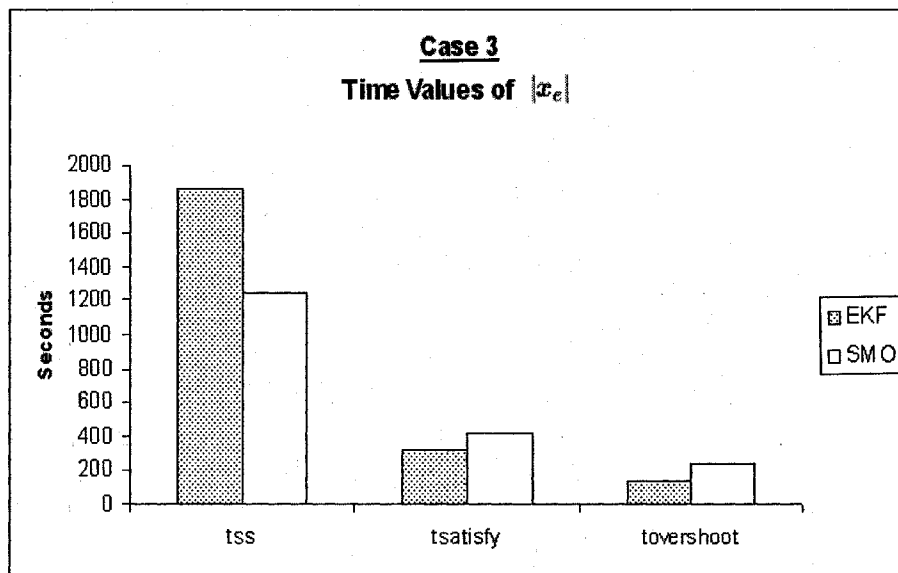


Figure 8-1: Case One - Steady-State Statistics of  $|x_e|$



Figure 8-2: Case One - Time Values of  $|x_e|$ Figure 8-3: Case Two - Time Values of  $|x_e|$

Figure 8-4: Case Three - Steady-State Statistics of  $|x_e|$ Figure 8-5: Case Three - Time Values of  $|x_e|$

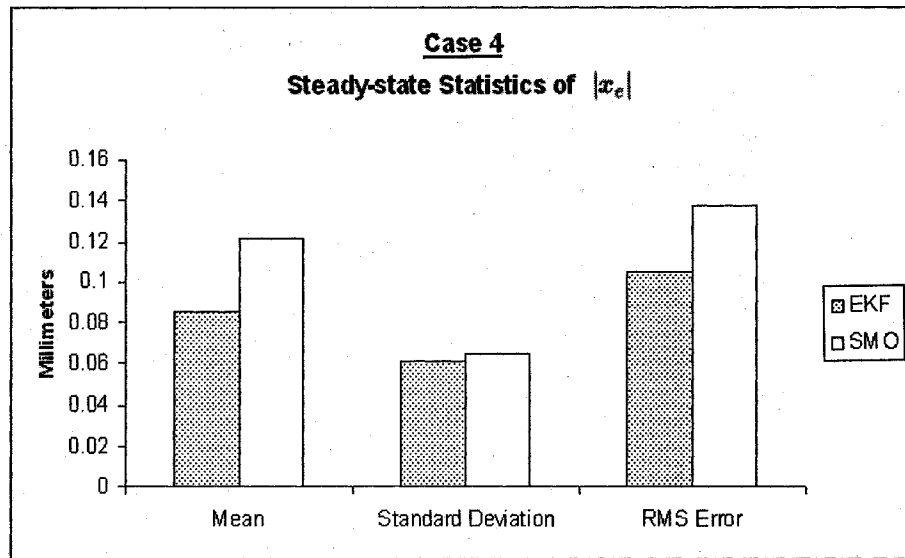


Figure 8-6: Case Four - Steady-State Statistics of  $|x_e|$

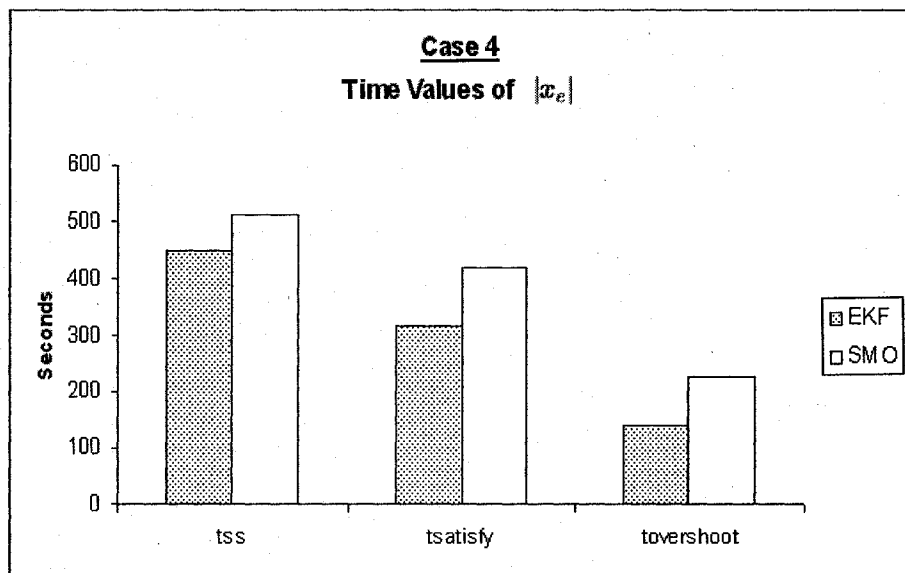
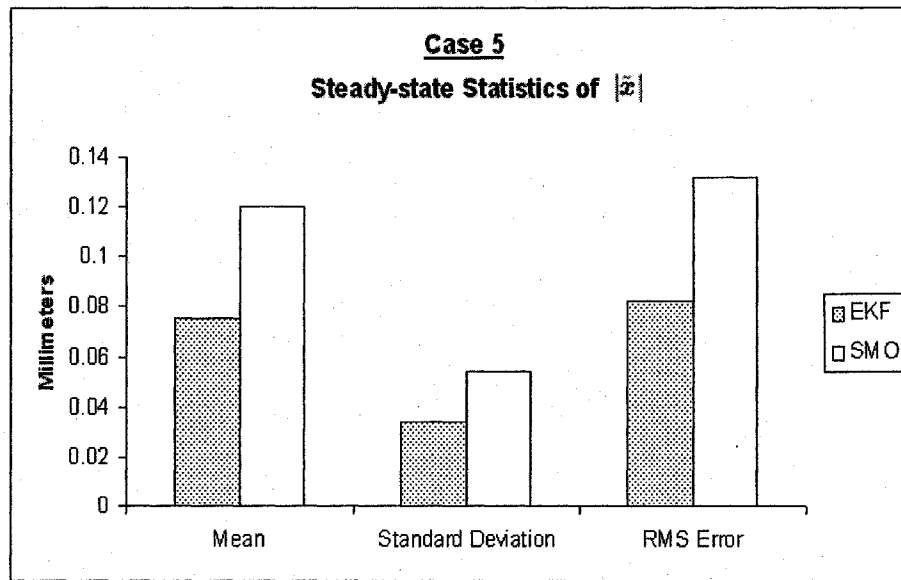
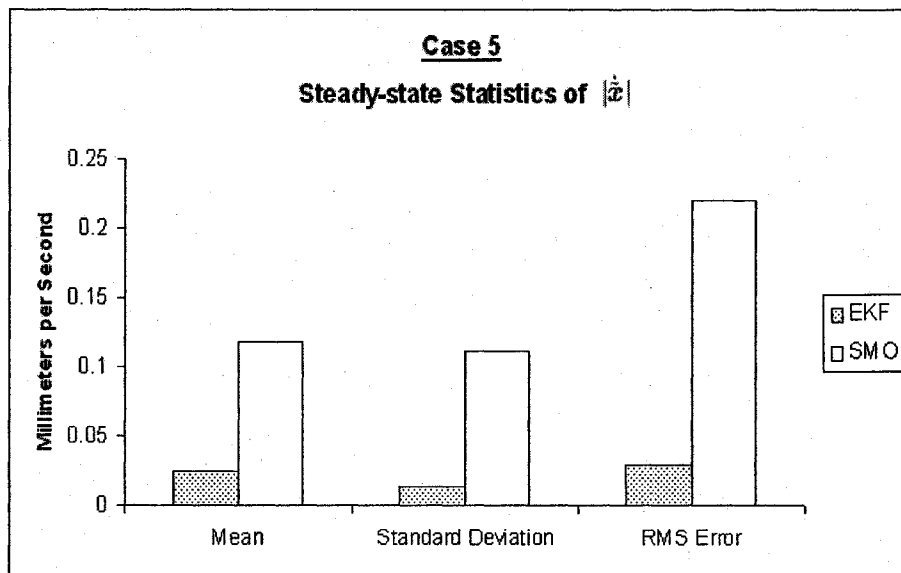


Figure 8-7: Case Four - Time Values of  $|x_e|$

The preceding figures also reveal that of the first four cases, Case Four is the only one in which the RMS error in  $\mathbf{x}_e$  is significant, indicating that most of the steady-state error and oscillation in Case Five is a result of measurement noise and input disturbances, not the initial conditions or parameter uncertainty. Interestingly enough, parameter uncertainty has negligible effect over the steady-state characteristics, as shown in Figure 8-4. This is because the simulations could only be reasonably run for 6,000 seconds, which is not a long enough time in orbit about the  $L_2$  point to induce significant percentage differences in the orbital parameters. The choice for the 6,000 second run-time was a result of the large computational requirements of the simulation, and corresponding real-time required for each simulation.

Case Five also investigates the steady-state characteristics of the relative position and velocity estimate error magnitudes. Figures 8-8, 8-9, and 8-10 show similar values for the steady-state characteristics of  $|\tilde{\mathbf{x}}|$ ,  $|\dot{\tilde{\mathbf{x}}}|$ , and  $|\mathbf{x}_e|$ , respectively. This demonstrates the ability of the controller to produce accurate control given an estimate. Figure 8-9 also demonstrates that the magnitude of the error in velocity estimation is greater for the Sliding Mode Observer than for the Extended Kalman Filter. This inaccuracy in relative velocity estimation results in wasted control effort, which is finite in space missions. Finally, Figure 8-10 shows that although it is slower (as shown in Figure 8-11), the Extended Kalman Filter provides a smaller steady-state error in  $|\mathbf{x}_e|$ , i.e. closer adherence to the desired position  $\mathbf{x}_d$ .

Figure 8-8: Case Five - Steady-State Statistics of  $|\tilde{x}|$ Figure 8-9: Case Five - Steady-State Statistics of  $|\dot{\tilde{x}}|$

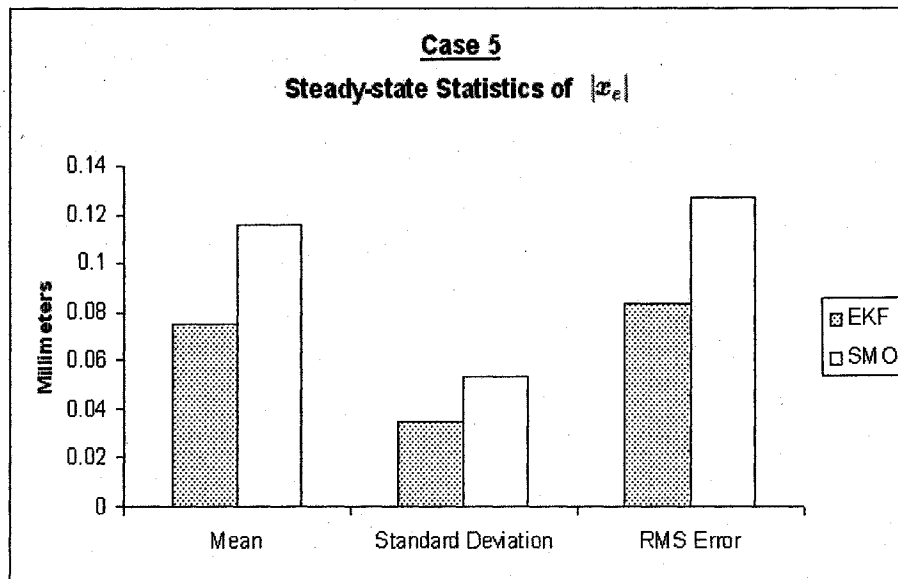


Figure 8-10: Case Five - Steady-State Statistics of  $|x_e|$

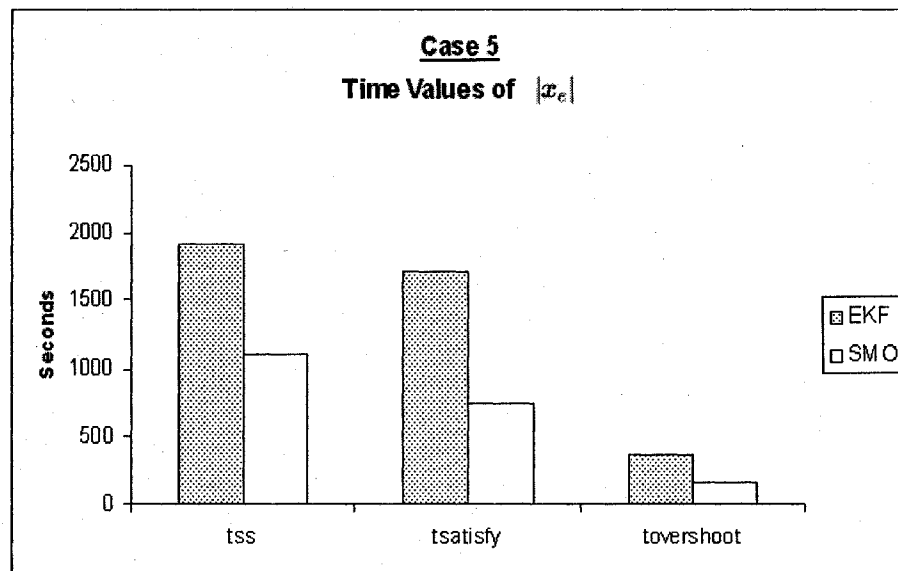


Figure 8-11: Case Five - Time Values of  $|x_e|$

Figure 8-12 shows the overshoot characteristics for each case. Here it is shown that in case Five, the overshoot for the Extended Kalman Filter is greater than for that of the Sliding Mode Observer, even though this is not true for Cases Two through Four. However, the overshoot associated with using the Extended Kalman Filter is greater in Case One, when differing initial conditions are used. This result simply carries through in Case Five. A similar trend is seen in  $t_{satisfy}$  and  $t_{ss}$ , the time it takes  $|x_e|$  to reach steady-state behavior. Although some cases demonstrate these quantities as being smaller for the Extended Kalman Filter than for the Sliding Mode Observer, the Sliding Mode Observer converges faster in Case Five. This is largely caused by the differing initial conditions from Case One.

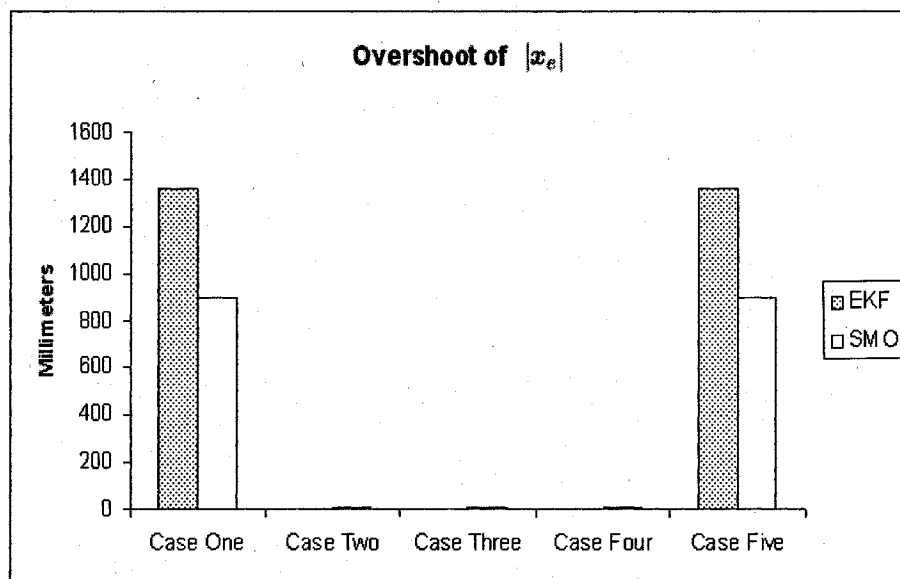


Figure 8-12: Overshoot Values of  $|x_e|$

## 8.2 Sensitivity Comparisons

It is also useful to consider each observer's sensitivity to changes in the nominal values of measurement noise, parameter uncertainties, and input disturbances, to determine each observer's efficacy in estimating the state in spite of such uncertainties.

The estimators' sensitivity to parameter uncertainty was assessed first. The simulation run-times in Cases Three and Five were not long enough to induce significant relative position errors due to parameter uncertainty. Using the same run time, however, significant errors can be induced by simulating inaccurate updates. The two orbital update parameters were varied, the position Earth's distance from the Sun, and the Earth's distance to the Leader,  $r_{SE}$  and  $r_{EL}$ , respectively. The following two figures investigate each observers' ability to accurately estimate the state given inaccurate parameter updates. Figure 8-13 shows the performance of each estimator

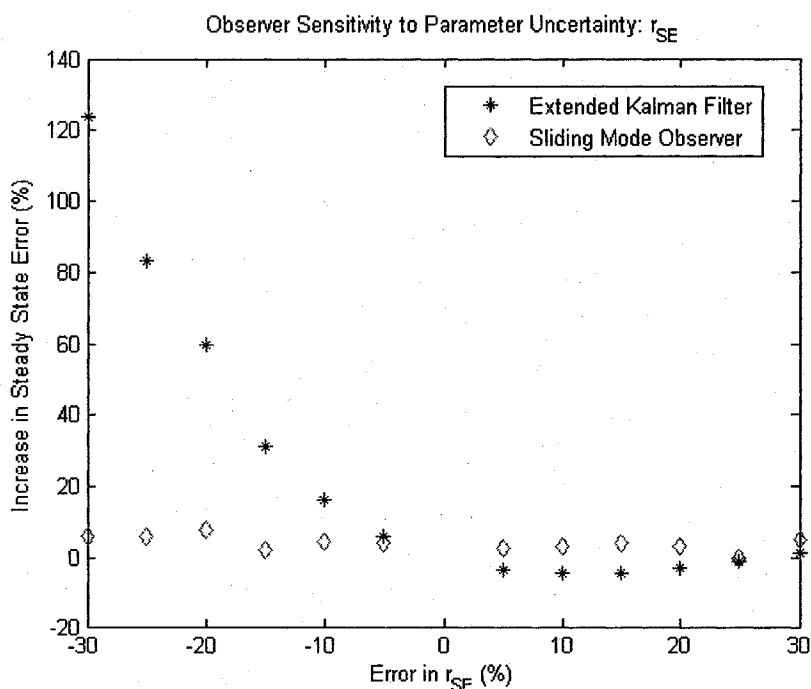


Figure 8-13: Observer Sensitivity to Parameter Uncertainty -  $r_{SE}$



for a given percentage inaccuracy in  $r_{SE}$ . For each percentage inaccuracy in  $r_{SE}$ , the percentage increase or decrease in the steady-state relative position estimation error magnitude over that obtained when using nominal values of all inaccuracies and disturbances (as in Case Five) is shown. Although the percentage inaccuracies in this figure are highly unrealistic (a 30% inaccuracy in the Earth's Distance from the Sun is equal to approximately 28 million miles), the information is useful to assess each observer's sensitivity to parameter uncertainties in general. The Sliding Mode Observer's sensitivity to inaccuracies in  $r_{SE}$  is less than that of the Extended Kalman Filter, as there is great variation in the increase relative position estimation error magnitude for differing percent changes in  $r_{SE}$ .

The second parameter to be evaluated was the Earth's distance to the Leader  $r_{EL}$ , as shown in Figure 8-14. For the Extended Kalman Filter, lower values of  $r_{EL}$  tend

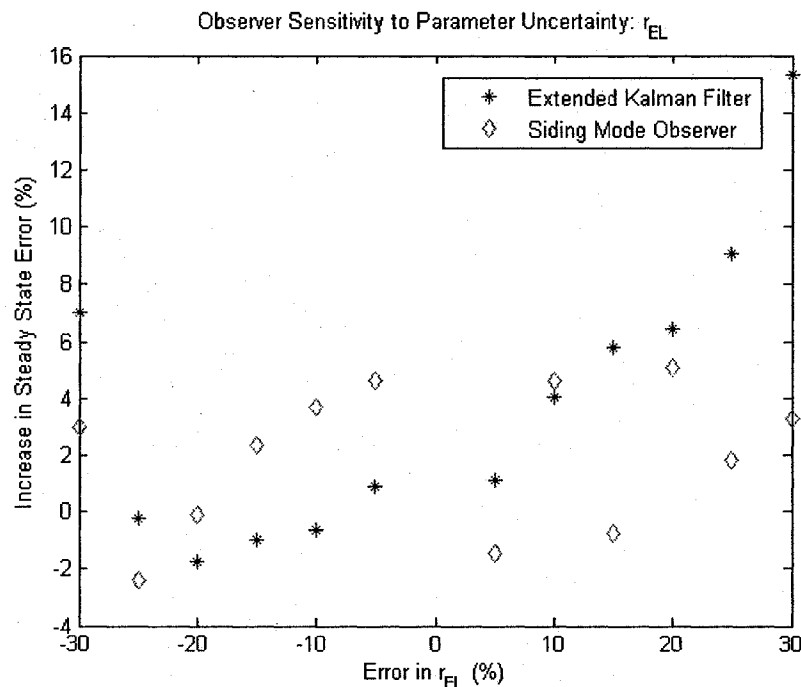


Figure 8-14: Observer Sensitivity to Parameter Uncertainty -  $r_{EL}$

to decrease the steady-state relative position estimation error. No consistent trend regarding the Sliding Mode Observer's sensitivity to inaccuracies in  $r_{EL}$  appears in this figure. As Figures 8-13 and 8-14, reveal no consistent trend for either observer, general assertions regarding these observers' sensitivity to parameter uncertainty are not made for the given simulation conditions.

The observers are next compared in terms of their sensitivity to measurement noise. Figure 8-15 shows why the Extended Kalman Filter is well known for its ability

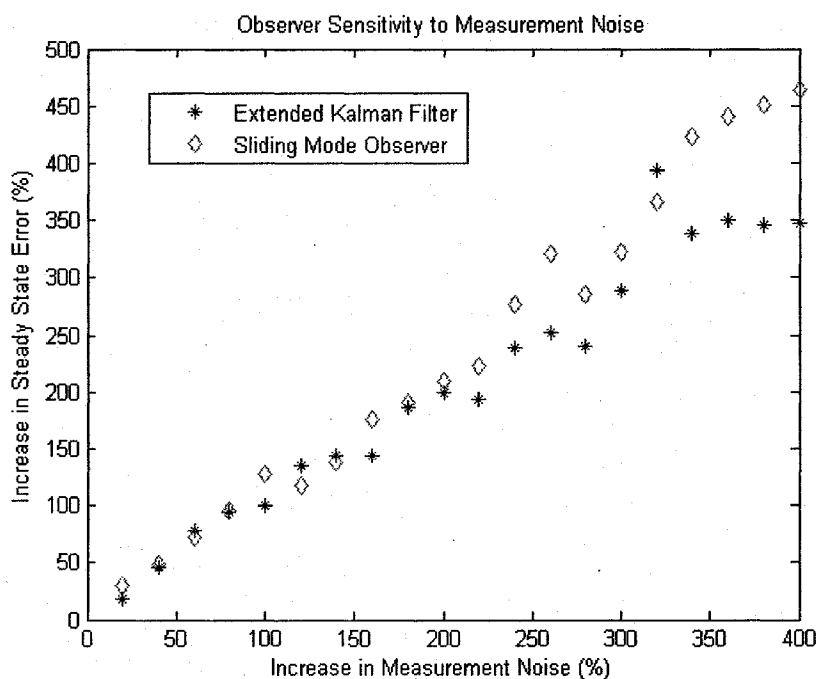


Figure 8-15: Observer Sensitivity to Measurement Noise

to handle measurement noise. In most cases, the Extended Kalman Filter outperforms the Sliding Mode Observer for measurement noise cancellation for most values, and becomes increasingly more favorable as the increase in measurement noise becomes more and more extreme. Such increases in measurement noise levels would not be

reasonably expected, however it is useful to investigate the observers' reactions to such increases. The nominal noise levels were selected by NASA designers as reasonable amount of expected measurement noise. In a real situation, if the measurement noise were to increase beyond the nominal values, the observers would be comparable for an increase of up to 80% over nominal.

Finally, the observers are compared in terms of their sensitivity to sinusoidal input disturbances, as shown in Figure 8-16. Here, it is evident that the Sliding Mode

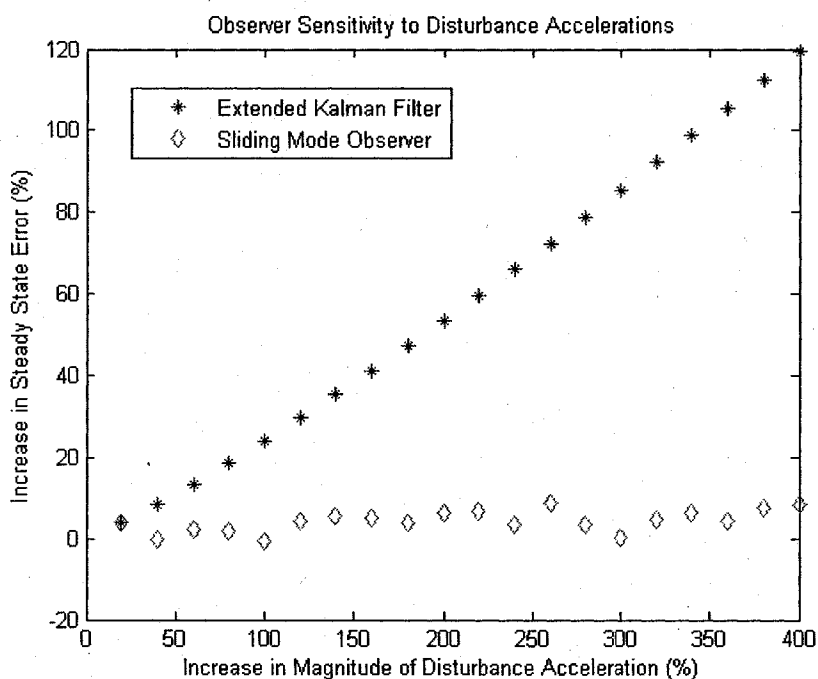


Figure 8-16: Observer Sensitivity to Disturbance Accelerations

Observer is far superior to the Extended Kalman Filter for input disturbance cancellation. The small slope that would be associated with locus of points pertaining to the Sliding Mode Observer would be quite low, indicating the Sliding Mode Observer's low sensitivity to input disturbances. The Extended Kalman Filter, on the

other hand, is quite sensitive to input disturbances, with estimation error increasing quite consistently with input disturbance magnitude. A 400% increase invokes a mere 8.25% change in the steady-state error of the Sliding Mode Observer relative position estimate, as opposed to 119.25% for the Extended Kalman Filter. As with the measurement noise levels, the nominal input disturbance levels were selected by NASA designers expected in a real situation.

### 8.3 Considerations

There are certain aspects of observer design that should be considered in deciding which observer to use for relative position estimates in a formation flying mission. There is no readily-defined optimal combination of gains, boundary layer thickness, and sliding surface for the Sliding Mode Observer, nor is there the same such combination of covariance matrices for the Extended Kalman Filter. As such, it is necessary to define some criterion (or criteria) of best observer performance, and to tune observers in search of meeting this criterion (or criteria). In this work, the criterion of best observer performance was the minimization of steady-state position estimation error. This criterion was selected given the mission performance goals, to maintain the relative position of the satellites at  $\mathbf{x}_d$ . This emphasis in observer tuning did not take into account the effects that velocity estimation errors would have on overall system performance, and therefore likely hindered the definition of the best observer. The observers' performance would have benefitted from considering velocity estimates as well as position, so the observer performance should have been evaluated accordingly.

There are also practices that could have been implemented in tuning the observers to comprise a more exhaustive tuning procedure. The tuning process assumed a hierarchical structure of tuning components (i.e. it was thought that finding the best process noise covariance matrix  $\mathbf{Q}$ , then finding the best measurement noise covari-

ance matrix  $R$ , would lead to the best Extended Kalman Filter. Similarly, the process for tuning the Sliding Mode Observer was to find the best Luenberger gains  $H$ , then Switching gains  $K$ , then boundary layer  $\phi$ ). This process however, leaves out combinations of tuning components that may yield better results. A better tuning process would have involved using a 2-factorial study to investigate the effects of changing the tuning components. Moreover, for the Sliding Mode Observer, the sliding surface should be considered a tuning component. Various sliding surfaces should be constructed, and considered in a 2-factorial study with  $H$ ,  $K$ , and  $\phi$ .

Having considered the recommended tuning procedures, it is clear that the Sliding Mode Observer tuning process leans toward being more time-intensive than that of the Extended Kalman Filter. This is a price one must pay for the versatility of the Sliding Mode Observer design. In deciding on which observer to implement, a decision must be made regarding how to weigh the value of tuning ease versus other constraints of the mission.

In deciding which observer to implement, it is beneficial to consider the versatility of observer design. The Sliding Mode Observer is very versatile in that its performance characteristics can be varied and improved by experimenting with different sliding surfaces, a technique not taken advantage of in this research. Nor is the Sliding Mode Observer sensitive to inaccuracies in the expected level of system and measurement noise, as is the case with the Extended Kalman Filter. The traditional Extended Kalman Filter may provide less accurate state estimates if noise levels are not as expected. One solution to this problem is the use of adaptive Extended Kalman Filters, beyond the scope of this research, which are capable of identifying the process and measurement noise covariances, and modifying noise parameters accordingly.

Another issue to consider is the computational burden of the observer on the on-board processors. When compared with the Sliding Mode Observer, the Extended

Kalman Filter is typically more computationally intensive, due in part to the necessity to calculate the measurement and state Jacobi, and the Kalman gain. Computational power comes at a premium for space missions, and it is generally favorable to favor computationally efficient algorithms, so long as performance is not compromised.

The nature of the formation flying mission must also be considered in selecting an observer. For example, in the Constellation X mission, the Extended Kalman Filter was shown to converge at a slower rate than the Sliding Mode Observer. In all actuality, this is not a problem for most interferometry missions involving large focal lengths. This is because as large focal lengths indicate a distant object of interest, one that will not move from a telescope's field of view quickly. Missions involving spacecraft docking, however, could benefit from an observer with quicker convergence characteristics, as this could shorten the time required for the docking procedure. Similar considerations can be made for overshoot.

## CHAPTER 9

### RESEARCH SUMMARY AND FUTURE WORK

#### 9.1 Conclusions

In this research, the Extended Kalman Filter and Sliding Mode Observer are compared for relative position and velocity estimation in a formation flying mission about the Earth/Moon - Sun  $L2$  point. A nonlinear measurement model employing the VISNAV relative navigation system is used, and the states are propagated in continuous time. State estimates are given to an adaptive controller.

Although both observers are successful in providing estimates to such a degree of accuracy as to meet design requirements, the Extended Kalman Filter formulated in this research is typically more accurate in terms of steady state relative position estimation error, and usually has less standard deviation in such estimates as well, indicating a less oscillatory response. This oscillation indicates that there will be a non-zero relative velocity, and the Follower spacecraft will require control effort of increasing frequency for higher standard deviations in  $|\bar{x}|$ .

The Extended Kalman Filter used in this research is shown, as expected, to be slightly more effective at processing measurement noise than the Sliding Mode Observer used in this research. Alternatively, the Sliding Mode Observer is shown to be far more effective at handling sinusoidal input disturbances than the Extended Kalman Filter.

Between the choice of the particular Extended Kalman Filter and particular Sliding Mode Observer considered in this research, it is the author's opinion that the

Extended Kalman filter would be a more prudent choice for state estimation for the Constellation X mission, assuming its integration is computationally feasible given on-board processing power. It should be noted however, that this recommendation pertains to the *particular* Extended Kalman Filter developed in this research over the *particular* Sliding Mode Observer developed in this research as well, not to either observer in general. The reason for this is that the method employed for observer tuning did not lead to a satisfyingly exhaustive search for either observer, and tuning emphasized only position estimate errors and not velocity. Considering the observers of this research in particular, the underlying reason for recommending this formulation of the Extended Kalman Filter lies in the desire to minimize relative velocity errors, in order to save on control effort. Both observers served well in propagating accurate state estimates for the Constellation X mission, but it is also necessary to consider the amount of control effort the system will require under each observer, as the amount of propellant used in the microthrusters proposed for Constellation X is finite. Fuel is a significant consideration for all space missions. Although this formulation of the Extended Kalman Filter is more sensitive to input disturbances than this formulation of the Sliding Mode Observer, the former is still capable of providing adequate state estimates given a four-fold increase over nominal input disturbance accelerations.

It should be noted, as stated earlier, that the Sliding Mode Observer used in this research should be tested using different sliding surfaces. There is a great deal of flexibility in selecting a sliding surface, so it is likely that the sliding surface used in this research is not optimal. If the observers are tuned further by using the results of a 2-factorial study, and evaluated considering the both velocity and position estimation, as opposed to simply position, a better comparison of the Extended Kalman Filter and Sliding Mode Observer can be obtained.



## 9.2 Future Work

Recommendations for future work include

- investigating the processing requirements of each observer on this particular mission. Given the expense of processing power in space missions, competent estimation algorithms that are computationally efficient should be favored.
- investigating the use of alternative sliding surfaces on the given Sliding Mode Observer. Other sliding surfaces may yield an observer that is favorable to the Extended Kalman Filter in terms of estimation competency and computational burden.
- simulating the linearized measurement model for the Constellation X mission. There is currently no formal stability proof for the Extended Kalman Filter, and as such these observers are often verified through Monte Carlo simulations. There is, however, a formal stability proof for the Sliding Mode Observer given a linearized measurement model for the Constellation X mission.
- eliminating the assumption that satellite attitude remains known and constant at identity throughout the simulation. This presents an opportunity to compare the Extended Kalman Filter with the Sliding Mode Observer for attitude determination in formation flying missions about the Earth/Moon-Sun  $L_2$  libration point.
- the further tuning of both observers, also considering multiple sliding surfaces for the Sliding Mode Observer. Integral and proportional terms can further improve the performance of the Sliding Mode Observer. For each observer, a 2-factorial study would provide a more methodical tuning process. Evaluating the estimate of the entire state instead of simply the estimation of the

satellites' relative position will also lead to more exhaustive results. Implementing these procedures will lead to a more comprehensive comparison of the Extended Kalman Filter and Sliding Mode Observer for formation flying about the Earth/Moon - Sun  $L_2$  libration point.

- comparing other nonlinear observers, such as H-Infinity Observers or Fuzzy Logic Observers for the formation flying mission considered here. Such considerations would lead to a more comprehensive understanding of the relative strengths and weaknesses of different observers for  $L_2$  formation flying missions.

## BIBLIOGRAPHY

- [1] W.E. Wiesel. *Spaceflight Dynamics*. Irwin/McGraw-Hill, Boston, 1997.
- [2] R.J. Luquette and R.M. Sanner. "Linear state-space representation of the dynamics of relative motion, based on restricted three body dynamics". In *Collection of Technical Papers - AIAA Guidance, Navigation, and Control Conference*, pages 353–361, 2004.
- [3] K. Koprubasi. Spacecraft attitude and angular rate estimation using sliding mode observers. Master's thesis, University of New Hampshire, 2004.
- [4] Stellar Imager (SI) Project Website. <http://hires.gsfc.nasa.gov/si>.
- [5] Terrestrial Planet Finder (TPF) Project Website. [http://planetquest.jpl.nasa.gov/TPF/tpf\\_index.cfm](http://planetquest.jpl.nasa.gov/TPF/tpf_index.cfm).
- [6] Micro-Arcsecond X ray Imaging Mission (MAXIM) Project Website. <http://maxim.gsfc.nasa.gov>.
- [7] S.-G Kim, J.L. Crassidis, Y. Cheng, A.M. Fosbury, and J.L. Junkins. "Kalman filtering for relative spacecraft attitude and position estimation". In *Collection of Technical Papers - AIAA Guidance, Navigation, and Control Conference*, pages 2518–2535, 2005.
- [8] P. Singla, K. Subbarao, D. Hughes, and J.L. Junkins. "Structured model reference adaptive control for vision based spacecraft rendezvous and docking". *Advances in the Astronautical Sciences*, 114:55–74, 2003.

- [9] J. Valazek and J.L. Junkins. "Intelligent control systems and vision based navigation to enable autonomous refueling of uavs". In *Proceedings of the 27th annual Rocky Mountain Guidance and Control Conference*, pages 113–131, 2004.
- [10] S. Tanygin. "Closed-form position triangulation for lost-in-space attitude and position determination". In *Collection of Technical Papers - AIAA/ASS Astrodynamics Specialist Conference*, pages 1486–1506, 2004.
- [11] S. Akila, E.K. Kumar, and N.S. Gopinath. "Orbital model studies for onboard orbit estimation". *Journal of Spacecraft Technology*, 16(1):8–30, 2006.
- [12] NASA Office of Technology Transfer Website. <http://techtransfer.gsfc.nasa.gov/ft-tech-GPA-MAGNAV.html>.
- [13] Geoffery Wawrzyniak, Dongsuk Han, George Lewis, Eric Graat, Darren Baird, and Diane Craig. "Genesis orbit determination for earth return and atmospheric entry". *Advances in the Astronautical Sciences*, 120(I):269–282, 2005.
- [14] Oscar Pace. "Gaia: The satellite and payload". In *Proceeding of the Symposium - The Three-Dimensional Universe with Gaia*, pages 23–28, 2005.
- [15] James Webb Space Telescope (JWST) Project Page. <http://jwst.nasa.gov>.
- [16] Philip A. Sablehaus, Doug Campbell, Mark Clampin, John Decker, Matt Greenhouse, Allan Johns, Mike Menzel, Robert Smith, and Pam Sullive. "An overview of the james webb space telescope (jwst) project". In *Proceedings of the SPIE - The International Society for Optical Engineering, UV/Optical/IR Space Telescopes: Innovative Technologies and Concepts II*, pages 1–14, 2005.
- [17] H.D. Stevens, Jack Rodden, Phil Morton, and Matthias Fehrenback. "Validating a formation flying control system design: the grace project experience". *Advances in the Astronautical Sciences*, 104(unnumbered):175–182, 2000.

- [18] C.J. Schrijver, K.G. Carpenter, and M. Karovska. "The stellar imager: A deep-space telescope to image stellar surfaces". In *Proceedings of the 13th Cambridge Workshop on Cool Stars, Stellar Systems and the Sun*, pages 951–954, 2005.
- [19] P.R. Lawson. "The terrestrial planet finder". In *2001 IEEE Aerospace Conference Proceedings*, page unnumbered, 2001.
- [20] W.C. Cash. "Maxim: Micro-arcsecond x-ray imaging mission". In *Proceedings of the SPIE - The International Society for Optical Engineering, Interferometry in Space*, pages 26–28, 2002.
- [21] A. Karlsson, L. D'arcio, R Den Hartog, and M Fridlund. "Darwin a mission overview". In *Proceedings of the SPIE - The International Society for Optical Engineering, Space Telescopes and Instrumentation 1: Optical, Infrared and Millimeter*, page unnumbered, 2006.
- [22] Daniel P. Scharf. "A survey of spacecrat formation flying guidance and control (part ii): Control". In *Proceedings of the 2004 American Control Conference (AAC)*, pages 2976–2985, 2004.
- [23] F.D. Busse, J.P. How, and J. Simpson. "Demonstration of adaptive extended kalman filter for low-earth-orbit formation estimation using edgps". *Journal of the Institute of Navigation*, 50(2):79–93, 2003.
- [24] N.K. Philip. "Relative position estimation using an extended kalman filter during the homing phase of rendezvous and docking". *International Journal of Systems Science*, 22(7):1241–1253, 1991.
- [25] V.I. Utkin. "Variable strucure systems with sliding modes". *IEEE Transactions on Automatic Control*, 22(2):212–222, 1977.

- [26] May-Win L. Thein, Julie K. Theinel, Rich Luquette, and Dean Tsai. Relative position estimation and control for precise formation flying of the constellation x mission. Technical report, NASA Goddard Space Flight Center, 2005.
- [27] J. Park, E.J. Boyle, R. Turton, and P. Famouri. “An experimental comparison of a sliding mode estimator to an extended kalman filter applied to a cold flow circulating fluidized bed”. In *Proceedings of IMECE04 2004 ASME International Mechanical Engineering Congress and Exposition*, pages 2421–428, 2004.
- [28] F. Chen and M.W. Dunnigan. “Comparative study of a sliding-mode observer and kalman filters for full state estimation in an induction machine”. In *IEEE Proceedings: Electric Power Applications*, pages 53–64, 2002.
- [29] E.A. Misawa. *Nonlinear State Estimation Using Sliding Observers*. PhD thesis, Massachusetts Institute of Technology, 1988.
- [30] J.-J. E. Slotine, J. K. Hedrick, and E. A. Misawa. “On sliding observers for nonlinear systems”. *Journal of Dynamic Systems, Measurement and Control*, 109(3):245–252, 1987.
- [31] A.M. Segerman and M.F. Zedd. “Preliminary planar formation-flight dynamics near sun-earth  $l_2$  point”. *Advances in the Astronautical Sciences*, 114:507–524, 2003.
- [32] A. Gelb. *Applied Optimal Estimation*. MIT Press, Cambridge MA, 1994.
- [33] R.J. Luquette and R.M. Sanner. “A nonlinear, six-degree of freedom, precision formation control algorithm based on restricted three body dynamics”. In *Collection of Technical Papers - AIAA Guidance, Navigation, and Control Conference*, pages 2518–2535, 2005.

## **APPENDICES**

## APPENDIX A

### CONSTELLATION X MODELS

Included here are the necessary MATLAB/Simulink models and m-files for the Constellation X model and measurement model, both common to the EKF and SMO simulations. Certain M-files and Simulink models are not included due to NASA proprietary considerations.

#### A.1 Simulation Models

Figure A-1 represents the overall Constellation X simulation model. Figure A-2 pertains the VISNAV measurement model.



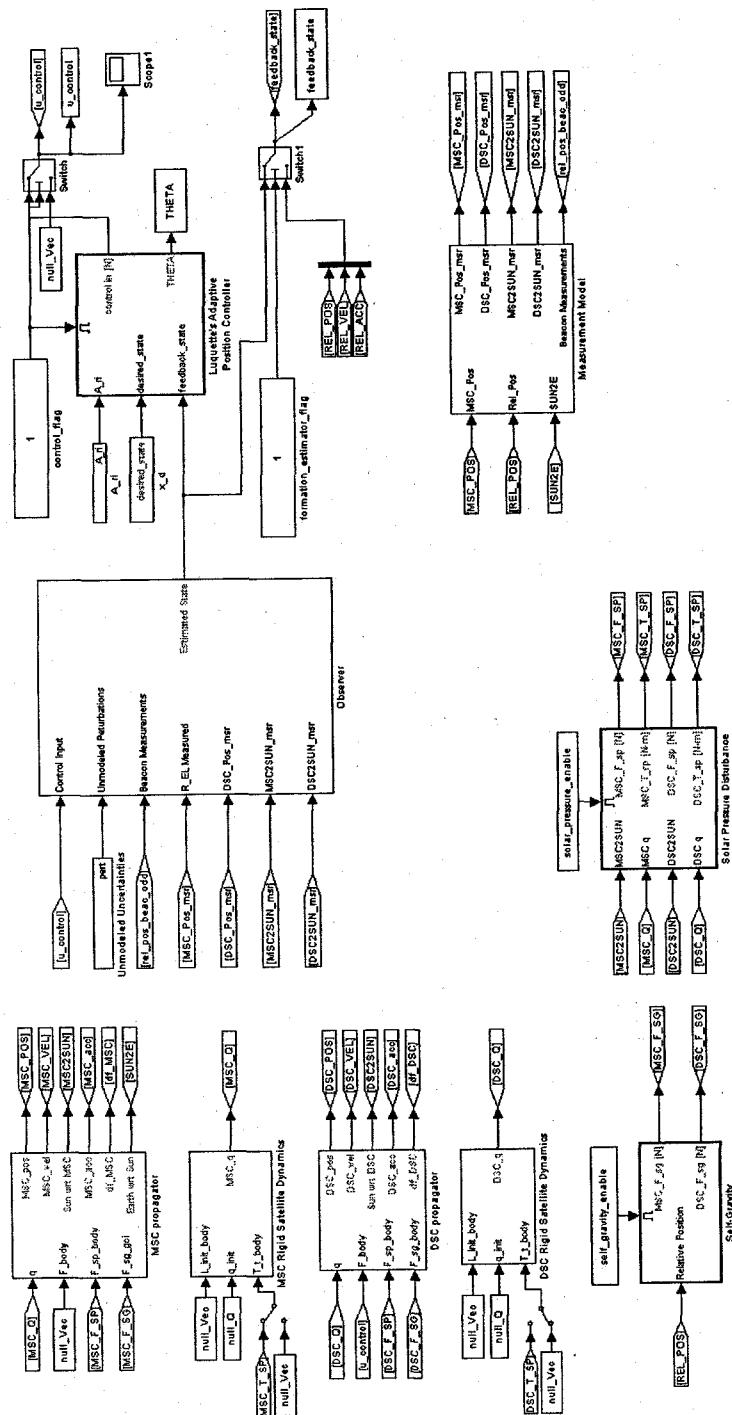


Figure A-1: Main Block Diagram - Constellation X Model

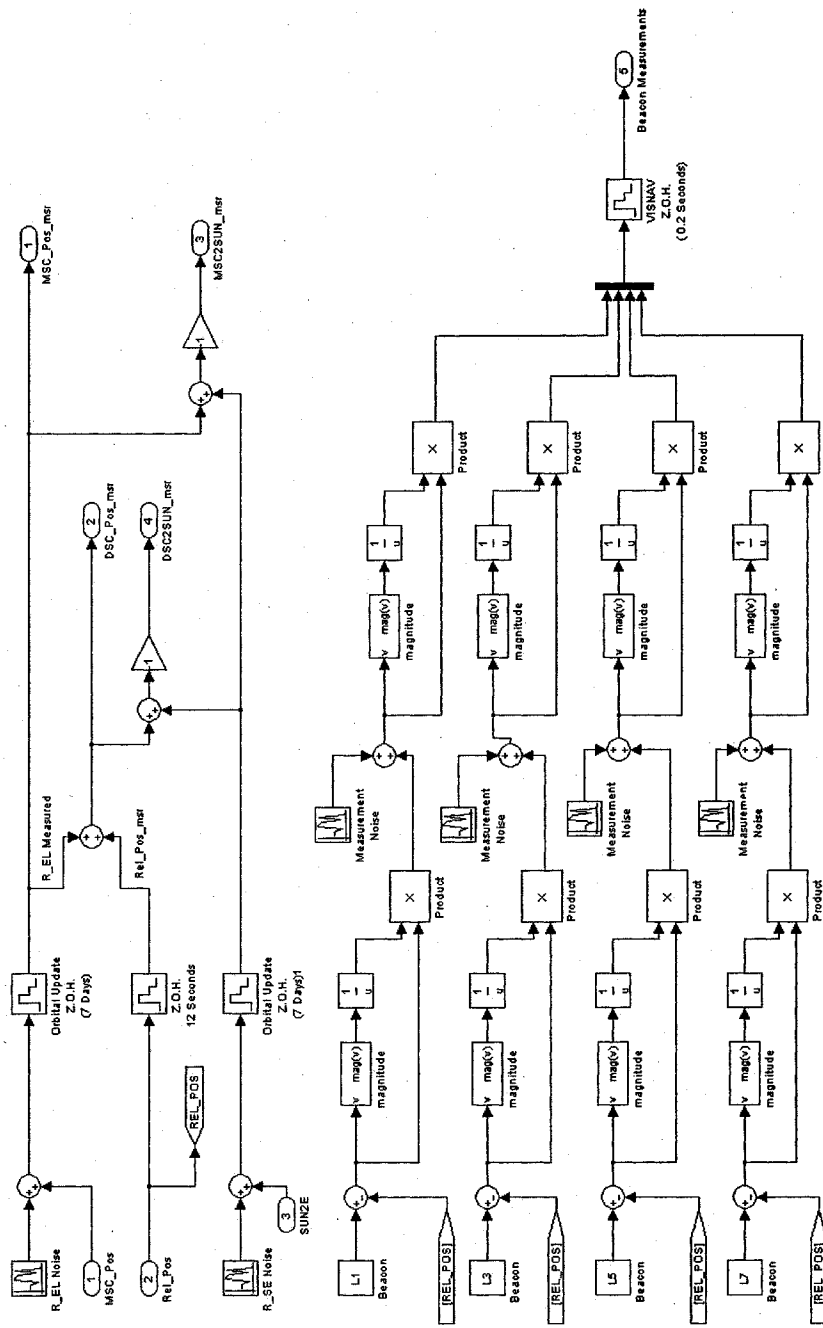


Figure A-2: Measurement Model Sub-block

## APPENDIX B

### EKF - DIAGRAMS & MATLAB FILES

Included here are the necessary MATLAB/Simulink models and m-files for the Extended Kalman Filter. Certain M-files and Simulink models are not included due to NASA proprietary considerations.

#### B.1 Extended Kalman Filter

Figure B-1 represents the Extended Kalman Filter simulation model. Figures B-2 through B-7 refer to the different levels (sub-blocks) of the simulation model. EKF\_observer.m is required to define the covariance matrices Q and R.

EKF\_observer.m:

```
beac_err = 0.0005*pi/180;  
q= 1e-7* [.4825 .4825 .4825 .4825 .4825 .4825];  
Q_EKF = diag(q);  
R_EKF = (beac_err*1000)^2*eye(12);
```

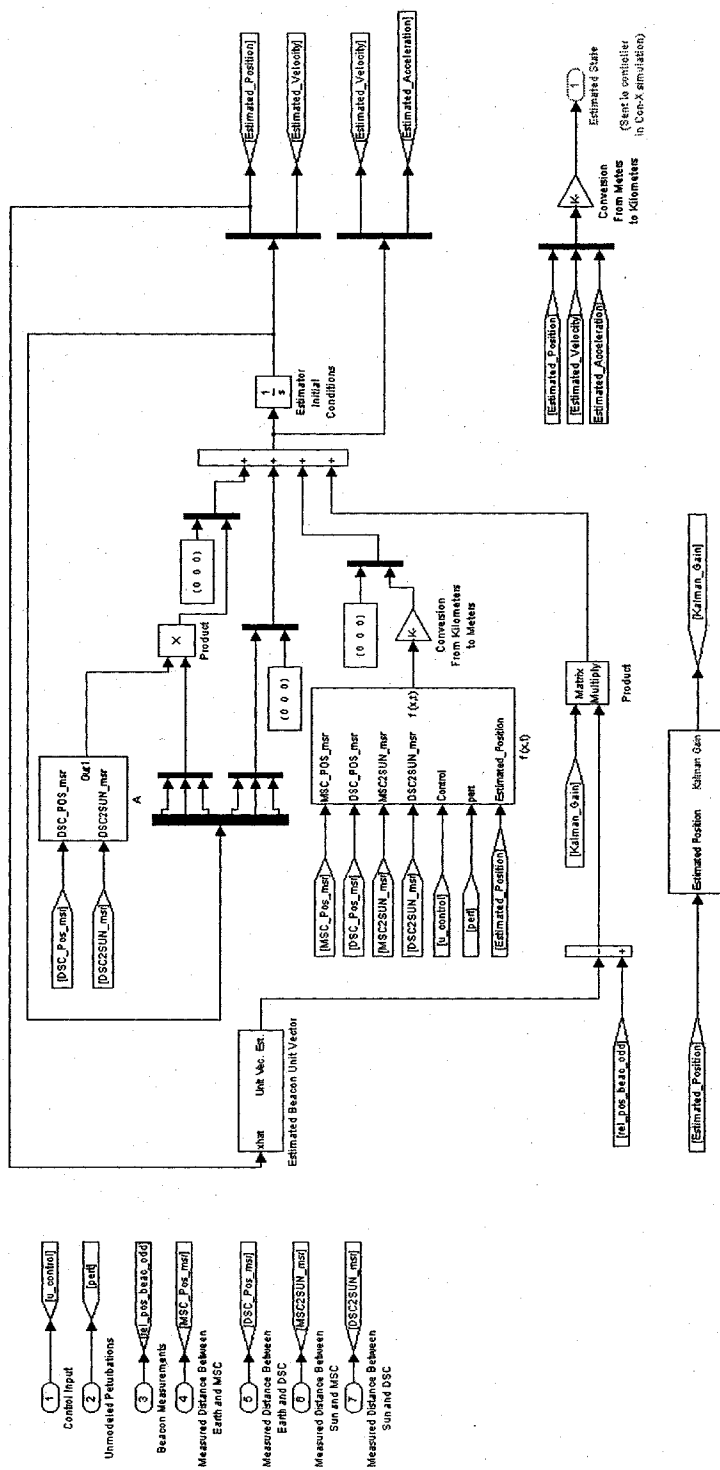


Figure B-1: Main Block Diagram - Extended Kalman Filter

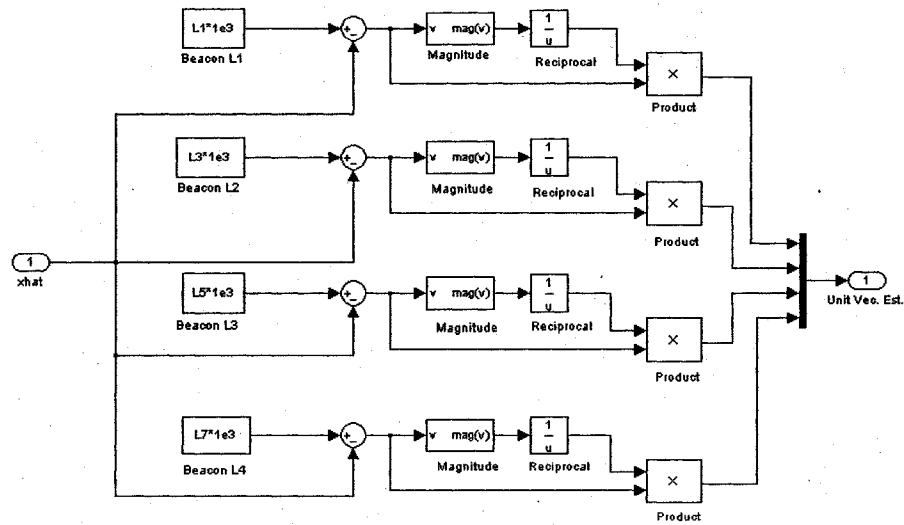


Figure B-2: Estimated Beacon Unit Vector Sub-block

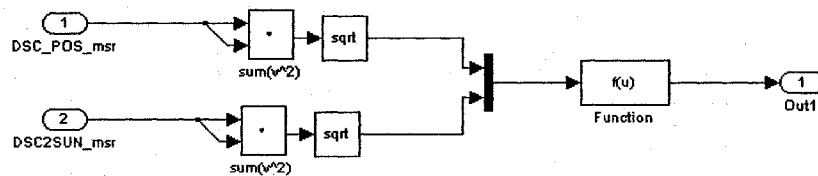


Figure B-3: Sub-block A

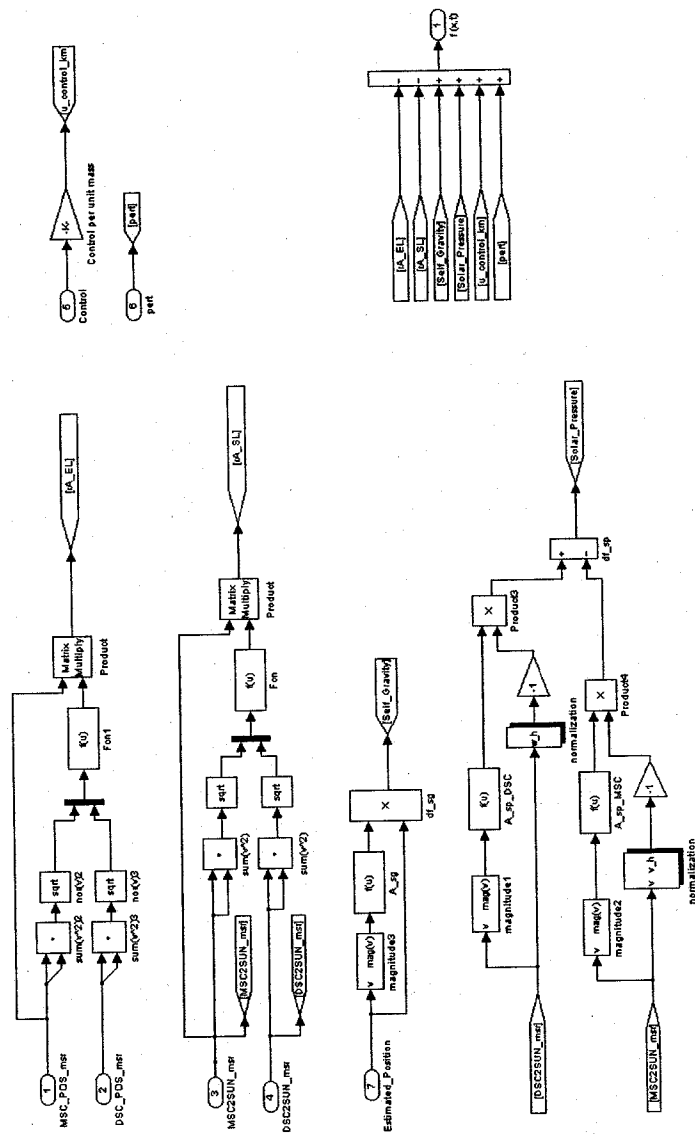


Figure B-4:  $f(x,t)$  Sub-block

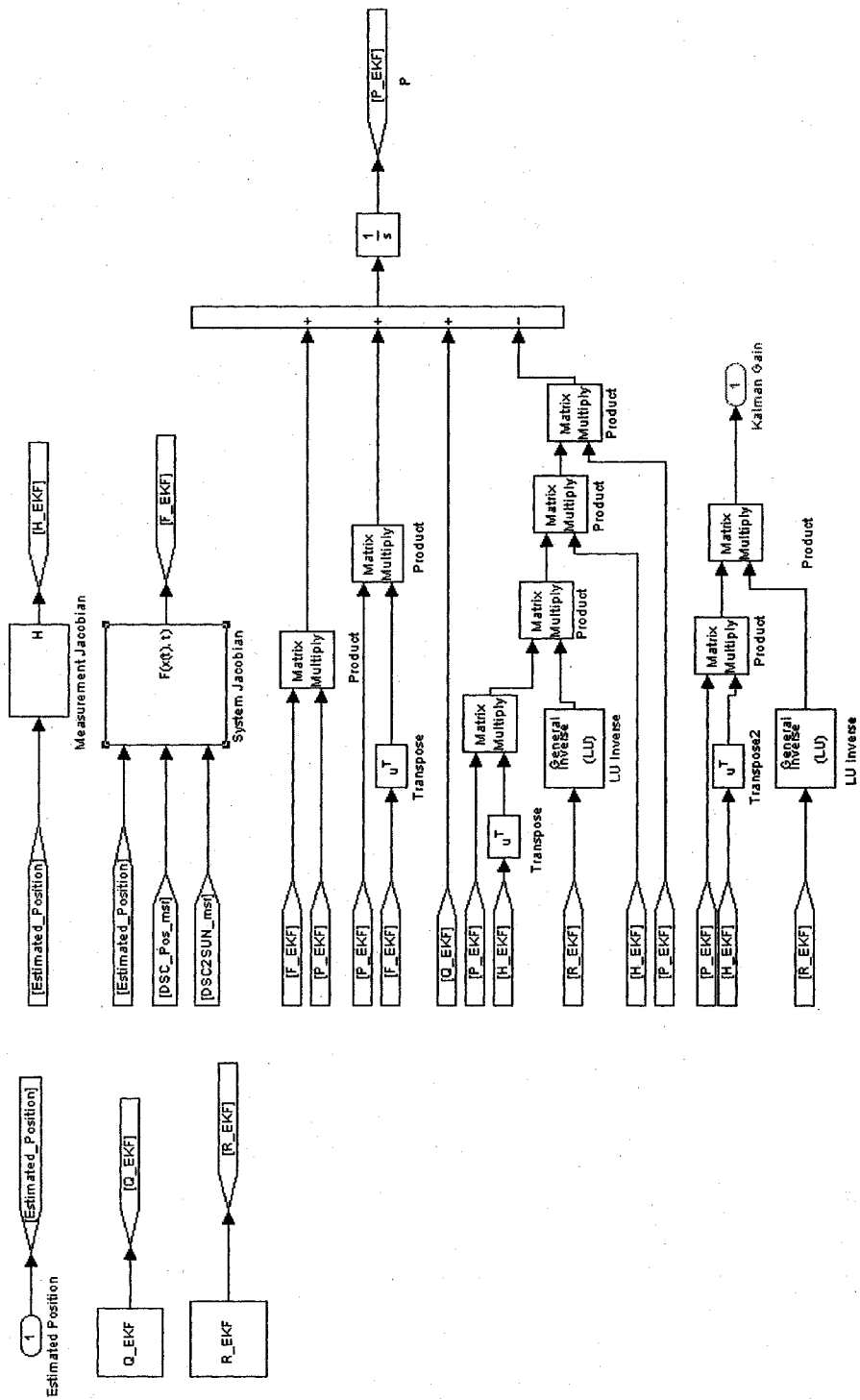
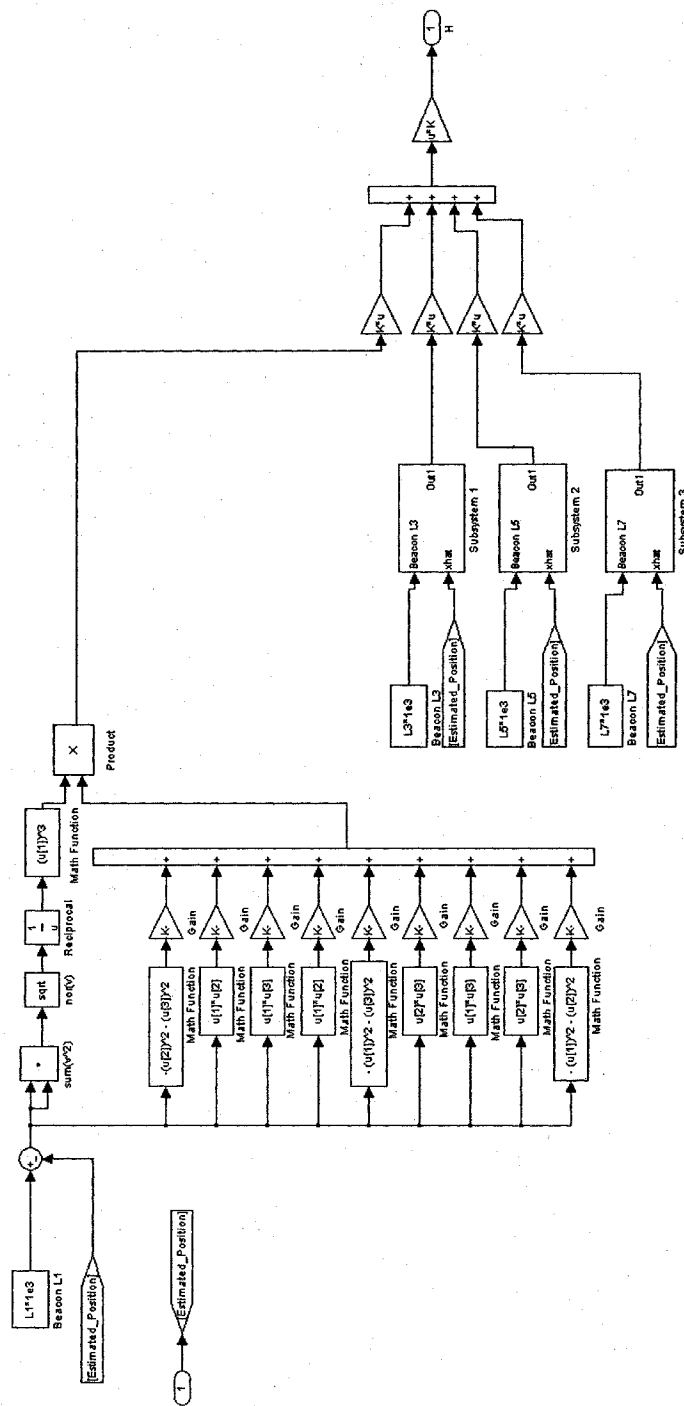


Figure B-5: Kalman Gain Sub-block



Subsystems 1, 2, and 3 are identical to the set of operations using Beacon L1

Figure B-6: Measurement Jacobian Sub-block



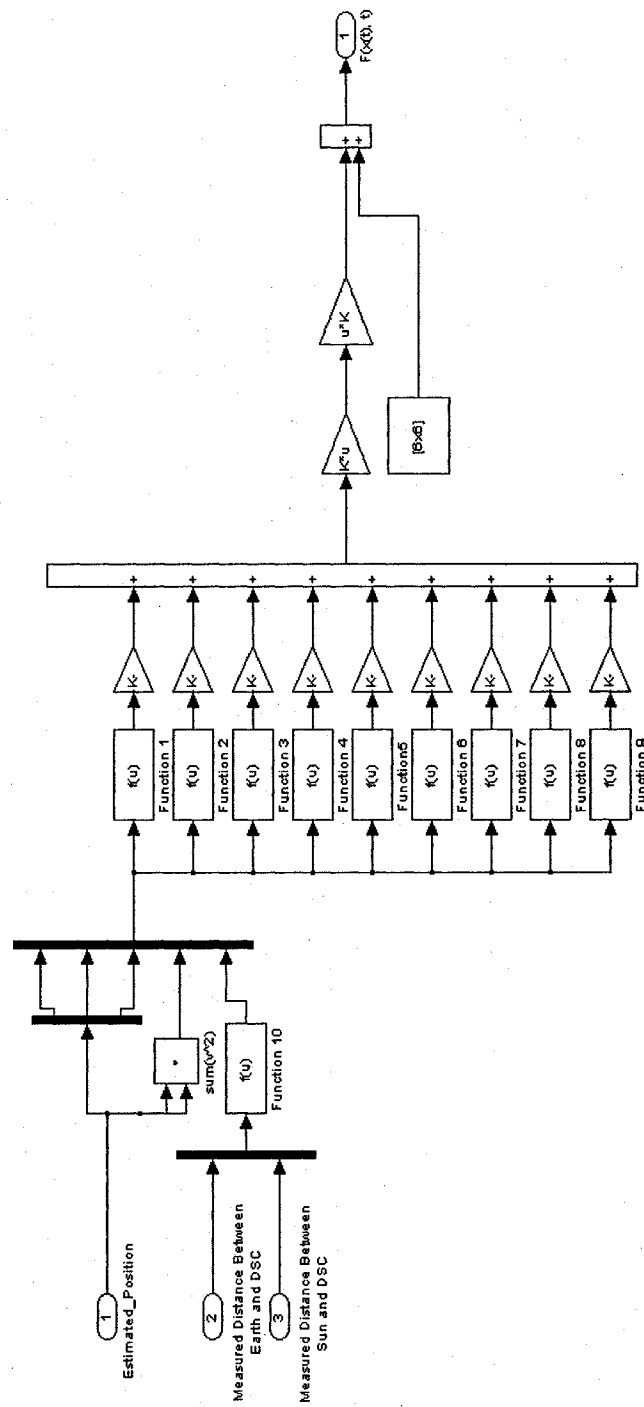


Figure B-7: System Jacobian Sub-block

## APPENDIX C

### SMO - DIAGRAMS & MATLAB FILES

Included here are the necessary MATLAB/Simulink models and m-files for the Sliding Mode Observer. Certain M-files and Simulink models are not included due to NASA proprietary considerations.

#### C.1 Sliding Mode Observer

Figure C-1 represents the Sliding Mode Observer simulation model. The necessary sub-block diagrams, are identical to Figures B-2, B-3, and B-4. SMO\_observer.m is required to initialize simulation conditions and parameters for the simulation.

UnitVectorSubBlock SMO\_observer.m:

```
H1a= -5; H1b= -10; H1c= -25; H1d= -.05; H1e= -.1; H1f= -.25;
H3a= -5; H3b= -10; H3c= -25; H3d= -.05; H3e= -.1; H3f= -.25;
H5a= -5; H5b= -10; H5c= -25; H5d= -.05; H5e= -.1; H5f= -.25;
H7a= -5; H7b= -10; H7c= -25; H7d= -.05; H7e= -.1; H7f= -.25;
```

```
% H_SMO matrix is in this form:
%      | H1a 0 0   H3a 0 0   H5a 0 0   H7a 0 0   |
%      | 0  H1b 0  0  H3b 0  0  H5b 0  0  H7b 0  |
%      | 0  0  H1c  0  0  H3c  0  0  H5c  0  0  H7c  |
%      | H1d 0 0   H3d 0 0   H5d 0 0   H7d 0 0   |
%      | 0  H1e 0  0  H3e 0  0  H5e 0  0  H7e 0  |
%      | 0  0  H1f  0  0  H3f  0  0  H5f  0  0  H7f  |
```

```
H_SMO= [1.1*H1a 0 0 1.1*H3a 0 0 1.1*H5a 0 0 1.1*H7a 0 0;
        0 1.1*H1b 0 0 1.1*H3b 0 0 1.1*H5b 0 0 1.1*H7b 0;
        0 0 1.1*H1c 0 0 1.1*H3c 0 0 1.1*H5c 0 0 1.1*H7c;
        H1d 0 0 H3d 0 0 H5d 0 0 H7d 0 0;
        0 H1e 0 0 H3e 0 0 H5e 0 0 H7e 0;
        0 0 H1f 0 0 H3f 0 0 H5f 0 0 H7f];
```

```
K_SMO= .8*[1e-5; 1e-5; 1e-5; 1e-7; 1e-7; 1e-7];
```

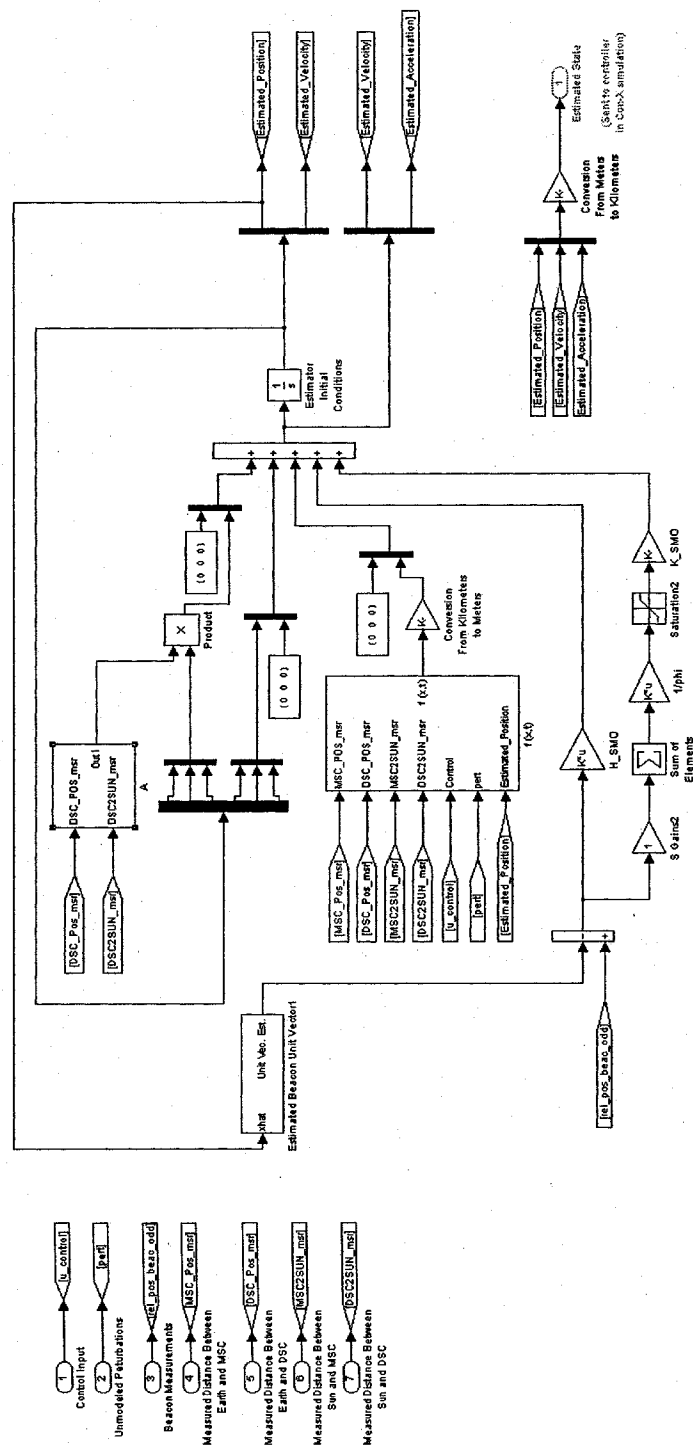


Figure C-1: Main Block Diagram - Sliding Mode Observer